Technical University of Denmark

Photonic crystal fiber long-period gratings for biosensing

Rindorf, Lars Henning; Jensen, Jesper Bo ; Bang, Ole; Lading, Lars; Pedersen, Lars Hag; Lindvold, Lars René

Publication date:
2008

Document Version
Publisher's PDF, also known as Version of record

Link back to DTU Orbit

DTU Library
Technical Information Center of Denmark

Photonic crystal fiber long-period gratings for biosensing

Lars Rindorf
November 1st 2007

COM·DTU

"It may be so; there's no arguing against facts and experiments."
Sir Isaac Newton when confronted with observations supposedly
destroying his theory of gravitation

"Worry about usage and users, not money. Provide something simple to use and easy to love. The money will follow"
Marissa Mayer, Vice President, Search Products & User Experience at Google, from her 9 notions of innovation

iv

Preface

The present thesis describes the scientific research carried out as part of the fulfillment of doctor of philosophy (Ph.D.) in the period November 1st 2004-October 31st 2007. The Ph.D. project is an Innovation Ph.D. project with emphasis on creating the basis for a commercial product. The thesis is to be evaluate as a standard thesis. A business plan may optionally be included in the thesis, but the thesis is to be evaluated on the scientific part *only*. I have chosen to include a tentative business plan as I think entrepreneurship should be a part of every Ph.D. project.

The work has been carried out in the Fibers and Non-linear Optics (FNO) group at COM•DTU, Department of Communications, Optics & Materials (now DTU Fotonik), Technical University of Denmark. The project was financed by the Technical University of Denmark and supervised by

- Ole Bang, Associate Professor, Ph.D., Fibers and Non-linear Optics (FNO), COM•DTU, Technical University of Denmark, Kgs. Lyngby

- Jesper Bo Jensen, Høiberg A/S, Denmark, former Assistent Professor, Ph.D., Fibers and Non-linear Optics (FNO), COM•DTU, Technical University of Denmark, Kgs. Lyngby

- Lars René Lindvold, Ph.D., Risø/DTU, Roskilde, Denmark

- Lars Lading, Ph.D., Director, Sensor Technology Center A/S, Taastrup, Denmark

- Lars Hagsholm Pedersen, Ph.D., Bioneer A/S, Hørsholm, Denmark

Acknowlegdements

I would like to thank a number of people (in no particular order) who have helped or contributed to this thesis. I would like to thank Oliver Geschke,

Abstract

The rapidly growing field of label-free biosensors demands an accurate and portable yet cheap technology. Inspired by the success of surface plasmon resonance biosensors it is investigated whether the unique light guiding properties of photonic crystal fibers (PCFs) can be made useful in this application. The presented work focuses on long-period gratings in PCFs (PCF-LPGs) as these will be shown to posses the required sensitivity. Strong interaction between the sample and probing light is obtained by infiltrating the sample into the holes of the PCF. The PCF-LPG sensor is studied both experimentally and numerically. Experimentally, a setup for CO_2-laser inscribed LPGs has been constructed. The setup produces LPGs with unprecedented quality and throughput. Numerically, the simulation of PCF-LPGs is a demanding task and requires accurate mathematical methods such as the finite element method (FEM). The FEM is very general and can also give estimates to the attenuation constants of the lossy cladding modes as well heat transfer simulations of the rapid, intense heating and cooling during the CO_2-laser inscription.

As sensors PCF-LPGs are shown to detect layers of biomolecules ~ 0.25 nm thick on average while having a refractive index sensitivity of $\sim 10^{-5}$. The PCF-LPG has a vanishing temperature cross sensitivity of ~ 6 pm/$^\circ$C. The sensitivities are shown to be highly dependent on the PCF design, and theoretically it is shown that enhancements of these values of two orders of magnitude is realistically possible. Correct expressions for the sensitivity of PCF-LPGs for refractive index sensing, biosensing, and temperature sensing are derived and presented for the first time. The sensitivity characteristics of LPG-PCFs promise for successful label-free biosensors.

Resumé (Danish abstract)

Det hurtigt voksende felt labelfri biosensorer efterspørger en nøjagtig og bærbar, men alligevel billig teknologi. Inspireret af overfladeplasmon biosensorers succes bliver det undersøgt hvorvidt de særlige lyslederegenskaber i fotoniske krystalfibre (FKF) kan gøres brugbare til samme anvendelse. Det foreliggende studium fokuserer på langperiodiske gitre i FKF (FKF-LPG), idet disse vises at have den fornødne følsomhed. En stærk vekselvirkning mellem prøve og lys opnåes ved at infiltrere prøven ind i hullerne på den FKF.

FKF-LPG studeres både eksperimentelt og numerisk. Eksperimentelt er der blevet bygget en opstilling med en kuldioxidlaser til indprægning af LPG-FKF. Opstillingen kan producere FKF-LPG'er med en hidtil uset kvalitet og antal. Numerisk er modelleringen af et FKF-LPG en krævende opgave and kræver nøjagtige matematiske metoder såsom finite element metoden (FEM). FEM er meget generel og kan også give svar på dæmpningskonstanten af kappetilstande ligesom simulere varmeledningen under den hurtige, intense opvarmning og afkøling af FKF'en under indprægningen med kuldioxidlaseren.

Som sensor vises FKF-LPG at være i stand til at måle et lag af biomolekyler ~ 0.25 nm tykt i gennemsnit med en brydningsindeks følsomhed på $\sim 10^{-5}$. FKF-LPG har en ubetydelig temperatur følsomhed på ~ 6 pm/$^\circ$C. Følsomhederne vises at være generelt meget afhængige af FKF'ens udformning, og teoretisk vises det, at forbedringer af de viste værdier med to størrelsesordener er realistisk muligt. Korrekte udtryk for følsomheden for brydningsindeksmåling, biosensorer og temperaturmålinger bliver udledt og præsenteret for første gang. Følsomhedskarakteristika for FKF-LPG forudsiger, at FKF-LPG kan blive succesfulde som labelfri biosensorer.

Publications

This thesis is partly based on the work presented in the following publications.

Journal papers

[1] L. Rindorf and N. A. Mortensen. Non-perturbative approach to high-index-contrast variations in electromagnetical systems. *Opt. Com.*, 261:181–186, 2006

[2] L. Rindorf and N. A. Mortensen. Calculation of optical-waveguide grating characteristics using greens functions and dysons equation. *Phys. Rev. E*, 74:036616, 2006

[3] L. Rindorf, P. E. Hoiby, J. B. Jensen, L. H. Pedersen, O. Bang, and O. Geschke. Towards biochips using microstructured optical fiber sensors. *Analytical and Bioanalytical Chemistry*, 385(8):1370–1375, 2006

[4] L. Rindorf, J. B. Jensen, M. Dufva, L. H. Pedersen, P. E. Hoiby, and O. Bang. Biochemical sensing using photonic crystal fiber long-period gratings. *Opt. Express*, 14(18):8824–8831, 2006

[5] Danny Noordegraaf, Lara Scolari, Jesper Lgsgaard, Lars Rindorf, and Thomas Tanggaard Alkeskjold. Electrically and mechanically induced long period gratings in liquid crystal photonic bandgap fibers. *Opt. Lett.*, 15:7901–7912, 2007

[6] L. Rindorf and O. Bang. Sensitivity of photonic crystal fiber grating sensors: biosensing, refractive index, strain, and temperature sensing. *J. Opt. Soc. Am. B*, 25(3):310–324, 2008

[7] L. Rindorf and O. Bang. Highly sensitive refractometer with photonic crystal fiber long-period grating. *Opt. Lett.*, 33(6):563–565, 2008

Conferences

A. L. Rindorf, P. E. Hoiby, J. B. Jensen, L. H. Pedersen, T. P. Hansen, O. Bang, and O. Geschke, " Biomolecule detection with integrated photonic crystal fiber sensor", MicroTAS - International Conference on Miniaturized Systems for Chemistry and Life Sciences. 2005, Boston, Massachusetts, USA.

B. J. B. Jensen, G. Emiliyanov, L. Rindorf, P. E. Hoiby, O. Bang, O. Geschke, L. H. Pedersen, and A. Bjarklev, "Microstructured optical fibers, fundamental properties and biosensor applications", Optics East 2006 proceedings (paperid: 6369-1). Full conference paper publ. in proceedings/book.

C. D. Noordegraaf, L. Scolari, J. Lgsgaard, L. Rindorf, and T. T. Alkeskjold, "Electrically tunable long-period gratings in liquid crystal photonic bandgap fibers", In Proceedings (paperid: OThP2), 2007, OFC, Anaheim, LA, USA. Full conference paper publ. in proceedings/book.

D. L. Rindorf and O. Bang, "Rigorous modeling of cladding modes in photonic crystal fibers" (poster 220), OWTNM - Modelling of waveguides and devices, April 2007, Copenhagen, Denmark.

E. L. Rindorf, J. B. Jensen, M. Dufva, L. H. Pedersen, P. E. Høiby, and O. Bang, Bragg Gratings, "Photonic crystal fiber gratings: prospects for label-free biosensors", Bragg Gratings, Photosensitivity, and Poling in Glass Waveguides (BGPP) Topical Meeting September 2-6, 2007, Quebec City, Quebec, Canada. (Invited talk BWC4)

Contents

Chapter 1

Introduction

1.1 Biosensor

A biosensor is used to identify target molecules in a sample. The term "biosensor" is often used somewhat loosely to describe some sort of sensing that is related to biology. Although this is not wrong, the term has a specific meaning to it. A biosensor formally consist of two components: 1) a sensitive biological element, 2) a detector element [8]. The biological element can be created by biological engineering. Its purpose is to give a specific response to specific biomarker, that can be nucleic acids (e.g. DNA), antibodies-antigens, proteins, enzymes, tissue, microorganisms, organelles, cell receptors etc. The detector element can be optical, piezoelectric, electrochemical, thermometric, or magnetic. It detects changes in the biological element. A sensor can only qualify as a biosensor if it is successful in both respects. In an experiment the sensor should be able to distinguish between different types of e.g. biomolecules in a sample. The distinction is made in a selective capture of the target biomarker.

A successful biosensor has a highly sensitive detector element that can detect minute changes in the biological sensitive element, without cross sensitivity to other irrelevant parameters, such as temperature. On the other hand the biosensor can not perform better than its biological element. If the biological element has a high degree unspecific binding, the biosensor will not be accurate. If a technology can not be taken out of the laboratory it is effectively useless. A successful biosensor may be mass produced with a high yield.

In the real world the perfect sensor for a given application may not exist. For an ideal biosensor it is possible to state a list of goals:

1. Surface chemistry: Preferably gold, silica, or silicon. These are well known.

2. Fast response time. < 2 minutes. Use in e.g. airports, hospitals etc.

3. Small & scalable sample size: picomole-attomole ($10^{-12} - 10^{-18}$ mole). Low consumption of sample.

4. Sample volume small & scalable: range 1pL - 1mL.

5. Fingerprinting of target molecules. Identification of molecule by the molecular structure.

6. Portable (Point-of-care). The sensor fits in a doctor's office, ambulance, or hospital ward.

7. Disposable. No contamination of sample by previous tests.

8. Economical: scalable production, and low cost optical components.

A further discussion can be found in the business plan in App. A.

1.2 Current and future technologies

A recent review by R. Bashir [9] categorizes biochemical MEMS[1] into three groups: mechanical detection, electrical detection, and optical detection. Optical biosensors are widespread and they enjoy reliability, flexibility and high sensitivity. The optical methods comprise fluorescent markers [10] and surface plasmon resonance (SPR) [11]. The non-fluorescent sensors are generally known as label-free biosensors, because they do not use fluorescent labels on the molecules. SPR technology is well established for biomolecular interaction analysis (BIA), with equipment available from several companies, most prominently Biacore AB. Promising candidates for next generation [12] portable label-free optical biosensors are ring resonators [13], microsphere resonators [14], and photonic crystals [15].

   Photonic crystals are artificial materials with special optical properties derived from microstructuring the material [16, 17]. A relative of the photonic crystal is the photonic cystal fiber (PCF) which has emerged only a decade ago [18]. PCF consists of a matrix of air holes surrounding a core in which light is guided. It has been shown by Monroe *et al.* [19] that PCFs may be infiltrated with substances which may be strongly probed by the

---
[1]Micro and Eletro-Mechanical Systems

evanescent wavesensing of the propagating light in the fiber. A gas sensor was later studied in detail, experimentally and theoretically, by Hoo *et al.* [20], who also considered the gas infusion times. It is these works that have laid ground to this thesis.

1.3 Photonic crystal fibers as evanescent wave sensors

Although, photonic crystals and PCFs have many similarities there are also fundamental differences. Photonic crystals use an artificial lattice of periodically arranged materials, which often, but not always, are silicon and air manufactured using technology from computer chip processing. The photonic crystals are closely related to natural crystals in solid-state physics where the atomic lattice gives rise to phenomena such as Bragg scattering at the surface and electronic band-gaps. PCFs are fabricated using a stack and draw process and do not necessarily posses Bragg scattering at surfaces or photonic band-gaps at the wavelength of operation. Typically, they exhibit neither. Nevertheless, the lattice of air holes running along the fiber axis can modify the light guiding properties of the fiber to an extent that is remarkable in itself.

Standard optical fibers have been used for evanescent wave biosensing for some time. See e.g. the reviews by Wolfbeis [10], Brogan and Walt [21], or Lee [22]. A standard optical fiber generally has a low fraction of the electromagnetic field energy intensity (field fraction) in its surroundings for evanescent wave sensing. The low field fraction thus gives a low sensitivity when used as an evanescent wave sensor.

Since the paper by Monroe *et al.* in 1999 [19] and Hoo *et al.* in 2003 [20], several directions have branched out. In 2004 Fini carried out a numerical study showing that a hollow core PCF could become a liquid core waveguide with a complete overlap between the liquid and the probing light [23]. Hollow core true bandgap guiding PCFs and hollow core Bragg fiber may provide exciting opportunities within gas and liquid spectroscopy and sensing [24, 25]. The liquid filled hollow core index guiding PCF was demonstrate by Cox in 2006 [26]. Fini also carried out a systematic investigation of the field fraction for different guiding mechanisms and PCF structures. Generally, a small pitch and large air holes give the highest fractions for index guiding. A single core suspended in air or liquid may be the best choice for obtain high field fractions in solid core waveguides [27].

Photonic crystal fibers have also been suggested as fiber optic probes

by Konorov *et al.* [28], where light is delivered in the core and collected by the cladding which has a high numerical aperture. Jensen *et al.* [29] used a PCF for fluorescent biosensing where the sample is infiltrated into the air holes. The cladding structure of a PCF was used. Light propagating in the cladding is very confined and has a high field fraction in the holes, than the core mode of a standard index guiding fiber. This direction has since spawn a number of papers. Rindorf *et al.* [3] have integrated a short piece of the same PCF as used by Jensen *et al.* [29] in a biochip and carried out a biosensing experiment. Smolka *et al.* has investigated the sensitivity of fluorescence in photonic crystal fibers [30, 31]. A similar approach is to coat the holes with a layer, which properties can be altered by the presence of small amount of gases or liguids. Matejec *et al.* has studied the performance of a so called grapefruit microstructured optical fiber. The holes are covered with xerogel layers which are sensitive to gaseous toluene [32].

Long-period gratings have been successfully demonstrated in standard optical fibre as label-free biosensing [33]. Although fiber gratings make a stable and robust platform, the sensitivity of these gratings is generally too low. PCFs have a much larger evanescent wave field fraction, and may thus be successful as label-free gratings. This line is also pursued by Rindorf *et al.* [4] have used gratings to carry out biochemical sensing and Phan-Huy *et al.* [34, 35] who have constructed a sensitive refractometer with a Bragg grating.

Yan *et al.* [36] have infiltrated Raman sensitive beads into a PCF. This research is motivated by the pioneering work of Kneipp *et al.* [37] in single-molecule detection using surface enhanced Raman scattering (SERS). SERS even allows for fingerprinting of molecules through their Raman spectrum. Surface plasmon resonance [11] can also be realized directly on the surface of fiber sensors. It is possible to make such sensors both with the plasmon on the facet and on the cladding of a Bragg fiber [38]. On the facet, the sensitivity to the refractive index has been shown experimentally to be 2×10^{-7} [10] while on the cladding it is experimentally 7×10^{-6} [38].

Recent times have also seen the arrival of microstructured polymer optical fibers. The production of such fibers is still not as developed as for silica fibers. Eventually, microstructured polymer optical fibers may be produced in materials with special properties for specific applications. Polymer allows for special surface chemistries in biosensors [39],[40] or the fabrication of porous, biodegradable fibers [41].

1.4   This thesis

It is the scope of this thesis to lay the foundations for a highly sensitive label-free biosensor based on photonic crystal fiber long-period gratings. The biosensor should eventually form the basis of a competitive commercial product. It is paramount that the technology is well documented and that sources of both enhancements and errors are identified.

In a timespan of three years many subjects are visited and many interesting results can be found. Some of these results deserve publication, some do not. Some work carried out during the project that has not been published, and is described in detail in this thesis. The thesis consists of two main parts: a scientific part and a commercial part with the scientific part forming the main part. The scientific part consists of several chapters which all to some extent could stand alone. Different readers may benefit differently according to their background, and proceed through the different chapters varying familiarity.

Chapter 2 concerns microfluidic aspects of biosensing and work on integrating a PCF in a microfluidic system. Chapter 3 presents the fundamentals of PCFs including theory and numerical methods. The resonance condition for long-period requires accurate effective indices. Efficient calculations are carried out using symmetry and the Finite Element Method. The resonant cladding modes are lossy and require open boundary calculations using perfectly matched layers. Chapter 4 gives a review of theory of fiber gratings, with emphasis on special issues related to PCF gratings. In particular, the lossy nature of the cladding modes can affect the width of the resonance dip and, in turn, the performance of the fiber grating as a sensor. Chapter 5 reviews the general sensor theory which incorporates the dispersion of the PCF. The expression for the sensitivity for refractive index sensing and biosensing are derived. The temperature susceptibility is also addressed with new, rigorously derived expressions. Experimental and numerical results are discussed. The results of the thesis are summarized in Chap. 6. The commercial part of the thesis is covered by a tentative business plan in App. A.

Chapter 2

Opto-fluidics

Optical biosensing is a biochemical experiment using optical detection. In this thesis the focus is on the optics, but the complementary competencies constitute a vastly larger field. Besides biomolecular interactions, which obviously are required, optofluidics [42, 43], microfluidics, and microsystem [44] design must be studied. At small microscopical scales the the fluidics exhibit unusual characteristics described in the field of microfluidics [45].

Besides the biochemical and microfluidic aspects there is the engineering task of taking the sensor out of laboratory. For efficient handling, the optical sensor must be implemented in a system with both an optical coupling as well as a fluidic coupling. Packaging optical and microfluidic systems on a chip is studied in the field of Lab-on-a-chip and biochip technology [46, 47, 48]. In principle, whole miniature laboratories (Lab-on-a-chip) can be fabricated on a chip complete with mixers, separators, PCR reaction chambers for multiplying DNA [49], etc. Needless to say, a successful commercial introduction of such technology will have an enormous impact on drug discovery, microbiology, and health technologies [50].

In order to demonstrate the applicability of PCF technology in this area we have integrated a short piece of PCF in an opto-fluidic biochip [3]. The PCF is identical to the one used by Jensen *et al.* [29] in a biosensing experiment. To the readers of this thesis unfamiliar with microfluidic theory a brief, rudimentary introduction is given. For a more thorough introduction the reader is referred to a recent, excellent book by Bruus for microfluidics in microsystems [51]. The following section is also based on this book. The main task of the considerations in the section is to obtain some estimates of time required to evacuate one solution from a PCF and replace it with another solution.

2.1   Prerequisites: microfluidics

In most biosensors the biomolecules are in an aqueous environment. It is thus fundamental to understand the mechanisms acting in liquids at a small scale. Flow in microsystems are generally characterized by *laminar* flow as opposed to turbulent flow. The Reynold's number describes the onset of turbulent flow and is the relation between inertial and viscous forces in the liquid. For a one micron wide channel the Reynolds number is $Re \sim 1 - 100 \ll 2500$, which is far below the onset of turbulent flow, ≈ 2500. Laminar flow has the advantage that it is possible in some cases to find simple analytical solutions to the Navier-Stokes equation; one such case is the flow in a circular tube. The high viscous forces requires large pressure gradients to obtain an effective flow, and thus flow in microsystems is general slow even compared with small microliter samples which are used.

Fluids driven by a pressure gradient generally obey an Ohm's law type of equation, $\Delta P = RI$, where ΔP is the pressure drop, R is the hydraulic resistance, and I is the fluid current. It can be shown that the hydraulic resistance obeys the same laws for parallel and serial systems as its electrical equivalent. In the case of a photonic crystal fiber the holes appear *in parallel*, and since the holes are usually identical, one merely divides the resistance of a single hole with the number of holes to find the total resistance.

Circular tube

The photonic crystal fibers have holes which are circular, and even in cases where they may elliptical they can be approximated to be circular, at least for our estimations.

For a circular tube of radius r we may solve the Navier-Stokes equation in radial coordinates to obtain the parabolic velocity profile,

$$v_z(r') = \frac{\Delta P}{4\eta L}(r^2 - r'^2), \tag{2.1}$$

where we have imposed the no-slip boundary condition $(v_z(r) = \partial_z v_z(r) = 0)$ at the sides. η is the dynamic viscosity, and L is the length of the PCF. For water the dynamic viscosity is $\eta \simeq 1\mathrm{mPa\,s} = 10^{-8}\,\mathrm{bar\,s}$. For light oils it is typically one or two orders of magnitude larger. The velocity may easily be integrated to obtain expressions for the fluid current and the hydraulic resistance,

$$I = \int_0^{2\pi} \! d\theta \int_0^r \! dr'\, r' v_z(r') = \frac{\pi}{8}\frac{\Delta P}{\eta L}r^4, \qquad R = \frac{\Delta P}{I} = \frac{8}{\pi}\eta L\frac{1}{r^4}. \tag{2.2}$$

We see that the current and the hydraulic resistance scale unfavorably with the radius of the hole. Thus for a given pressure overhead, ΔP, the required time for evacuating a sample increases 16 times for each reduction by half in the radius.

To provide the reader with some typical flow velocities and times for the infiltration of PCFs with water, we consider two PCFs which we will meet in the following chapters: the LMA10 and the Air-15-1550, both from Crystal-Fibre A/S [52]. The LMA10 is an index guiding PCF with a pitch of $\Lambda \simeq 7.1\,\mu\text{m}$ and a hole diameter of $d \simeq 3.2\,\mu\text{m}$. For a $L = 30$ cm long piece of LMA10 and an overhead of $\Delta P = 4\,\text{bar}$ we get

$$V = \frac{I}{\pi r^2} = \frac{\Delta P r^2}{8\eta L} \simeq 0.4\,\text{mm/s}, \quad I = \pi r^2 \times V \simeq 3.4\,\text{pL/s (per hole)}. \quad (2.3)$$

The time required to evacuate the PCF is thus $L/V \simeq 12\,\text{min}$. An LMA10 typically has seven rings of holes giving a total number of 168 holes, and thus the total flow velocity is $0.6\,\text{nL/s} \simeq 2\,\mu\text{L/h}$. The total inner volume of such a piece of LMA10 is $V = 168\,\pi r^2 L \simeq 0.4\,\mu\text{L}$. The Air-15-1550 is a photonic bandgap guiding PCF. Typical parameters for this PCF are $L \simeq 10\,\text{cm}$, $d \simeq 2.3\,\mu\text{m}$, and $\Delta P = 3\,\text{bar}$ giving

$$V = \frac{\Delta P r^2}{8\eta L} \simeq 0.5\,\text{mm/s}, \quad I = \pi r^2 \times V \simeq 3\,\text{pL/s (per small hole)}. \quad (2.4)$$

The PCF has 312 small holes and the total flow is $0.6\,\text{nL/s} = 2\,\mu\text{L/h}$. The inner volume of the 312 holes is $130\,\text{nL}$. The PCF also has a large center hole of $17\,\mu\text{m}$ in diameter. The flow is

$$V = \frac{\Delta P r^2}{8\eta L} \simeq 27\,\text{mm/s}, \quad I = \pi r^2 \times V \simeq 6\,\text{nL/s (large hole)}. \quad (2.5)$$

Thus the flow carried by the single $17\,\mu\text{m}$ hole is ten times that of the 312 small holes. The evacuation time is $200\,\text{s} \simeq 3$ min, and $\simeq 4$ s for small and large holes, respectively.

Molecular diffusion

Since the evacuation of different samples in the PCF is one of the most important aspects in biosensing, it seems worrying that the velocity is zero at hole surface where the molecular interactions take place. If the biomolecules at hole surface do not move, or the speed of movement is a fraction of the average flow speed, this would lead to almost infinite long evacuation

times. At the microscopical level Brownian motion of the molecules is considerable, and at finite temperatures any solution will diffuse to reduce any concentration gradients. The diffusion constant for water molecules is $D = 4 \times 10^{-11}$ m^2/s meaning that the time required for traveling, on an average, a distance equal to the diameter ($d \sim 2\,\mu$m) of a PCF hole is $\sqrt{d^2/D} \simeq 0.3$ s. For larger molecules the diffusion constant is smaller. For DNA we get typical diffusion times as

$$\text{DNA(30 base pair)}: \quad D \simeq 40\,\mu\text{m}^2/\text{s} \Leftrightarrow T(3\mu\text{m}) \simeq 0.2\,\text{s} \quad (2.6)$$
$$\text{DNA(5000 base pair)}: \quad D \simeq 1\,\mu\text{m}^2/\text{s} \Leftrightarrow T(3\mu\text{m}) \simeq 9\,\text{s}. \quad (2.7)$$

Any biomolecule at any position inside the hole of the PCF will thus diffuse into the vicinity of a biomolecular capture complex within a couple of seconds. This is important for the capture efficiency of the PCF-biosensor. The convection induced by the non-constant velocity profile (Eq. (2.1)) in the hole also contributes to dispersing the molecules, thus creating an effective diffusion known as Taylor dispersion [53]. The convection is considerable when the Peclet number, $Pe_r = rV/D \sim 10$, is greater than one. In this regime the effective dispersion, D_{eff}, is actually inversely proportional to the molecular dispersion,

$$D_{\text{eff}} = \frac{R^2V^2}{48D} \sim \frac{(1.5\,\mu\text{m})^2 \times (0.2\,\text{mm/s})^2}{48 \times 4 \times 10^{-11}\text{m}^2/\text{s}} = 4.8 \times \times 10^{-11}\text{m}^2/\text{s}, \quad (2.8)$$

but for our PCFs the effective dispersion maintains the same order of magnitude as the molecular diffusion. The most important point here is that for Taylor dispersion, the concentration of molecules is constant across the hole, meaning that the molecules close to the sides of the holes, where flow velocity is nearly zero, are not 'left behind' during evacuation. If this were the case then infiltrated molecules could by almost impossible to remove.

We have not discussed capillary forces in this chapter. Capillary forces are considerable in microfluidic systems, but since they exist at the boundary between two significantly different substances, such as liquid and air, they do not play any role in our experiments.

2.2   Biochip

The main purpose of integrating the PCF-biosensor in an opto-fluidic system is to facilitate handling as described in the introduction to this chapter. But there are also other benefits by integrating the PCF. It is possible to use a

much shorter piece of PCF (16 mm instead of 10 cm) and thereby reducing the infiltration time and the processing time. The most delicate part of the integration is the sandwich of the PCF between two multimode standard optical fibers (MMF) with large cores of 50 μm in diameter fibers (Fig. 2.1). The Air-15-1550 structure has a single hole of 17 microns surrounded by a microstructured cladding about 65 microns in diameter. The Air-15-1550 does not have any band-gap guiding in the core when it is infiltrated with water but guides only in the cladding. The optical fibers have to be aligned to obtain a high signal output, since light propagating in the bulk cladding has very little fraction and thus very little sensitivity. For standard optical fibers the alignment tolerances has to be within $\sim 10\mu$m. Such precision is achievable with the CO_2 laser method.
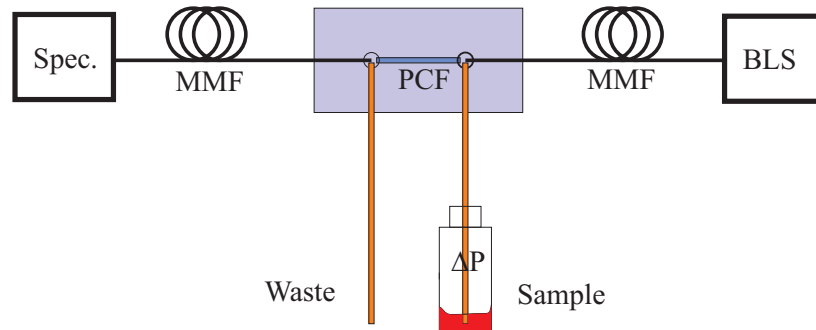
Figure 2.1: The biochip setup used in the biosensing experiments. The chip is connected to a broadband lightsource (BLS) and a spectrometer (Spec.) through multimode fibers (MMFs). The sample is pressed through the chip by applying a pressure overhead (ΔP) to the sample bottle.

Lambert-Beer's Law

As in the biosensing experiment by Jensen *et al.* [29] we carry out a biosensing experiment inside the PCF. The target biomolecules are detected by a fluorescent marker, Cy3, but we do not use the fluorescent signal itself. Instead the characteristic absorbtion spectrum of the fluorescent marker (Cy3), is used. Absorbtion is more stable than the fluorescence which decays in time due to photo-bleaching.

The absorbance results in an intensity drop of the transmitted light on certain frequencies (dependent on the absorbance spectrum). This intensity

drop is described by the Lambert-Beer law:

$$I(\lambda) = I_0(\lambda)\,10^{-A(\lambda)}, \tag{2.9}$$

where the absorbance, $A(\lambda) = \ln(10)\epsilon(\lambda)cL$, is a product of the molar extinction coefficient, $\epsilon(\lambda)$, the concentration, c, and the interaction length, L. Usually the sample is in a cuvette where the overlap of the light with the sample is complete. In the PCF the overlap of the probing light with the sample is only partial, and we can define an effective interaction length, $L_{\text{eff}} = f_u L$, to account for this, which is proportional to the length and the fraction of electromagnetic field intensity inside the air holes, f_u. The field fraction, f_u, depends on wavelength and is typically only a few percent but this is much larger than the field fraction in standard optical fibers, both single mode and multimode. The field fraction increases drastically when the hole is infiltrated with aqueous solutions since the index contrast is reduced. See Fig. 2.2 for f_u for the Air-15-1550. In an immobilization experiment the biomolecules are situated on the surfaces, and the effective interaction length is $L_{\text{eff}} = \eta_u L$, where η is the field energy intensity at the surface of the holes relative to the spatially averaged intensity in the PCF cross section. η_u for the Air-15-1550 is shown in Fig. 2.2. The relative field intensity at the surface, η_u, is a few percent of the average field intensity in the PCF cross section. Also η_u depends on the wavelength and increases when the PCF is infiltrated with aqueous solutions.

2.2.1 CO_2-laser micro-machining

The chip is fabricated in a three step process: First the channels are micro-machined in a piece of PMMA using a CO_2 laser, secondly a lid is sealed on top to close the microsystem using heat bonding, and lastly fibers and fluidic microtubing are glued into place.

The CO_2 laser ablation technique is quite general and fabricate arbitrary microfluidic designs with high throughput. A thin sheet (1.5 mm thick) of poly(methylmethacrylate) (PMMA), also commonly known as plexiglass, is placed under the CO_2 laser. The CO_2 laser has a built in computer controlled mirror which allows for controlling the position of the laser beam on the PMMA sheet. The minimal waist diameter of the beam is ~ 40 μm limiting the possible feature sizes to around 100 μm with a precision of about 5 μm [54]. In the ablation technique, intense, localized heating by the laser beam breaks up the polymer into monomers which evaporate from the surface. Ventilation is used to remove ablated material and gasses.
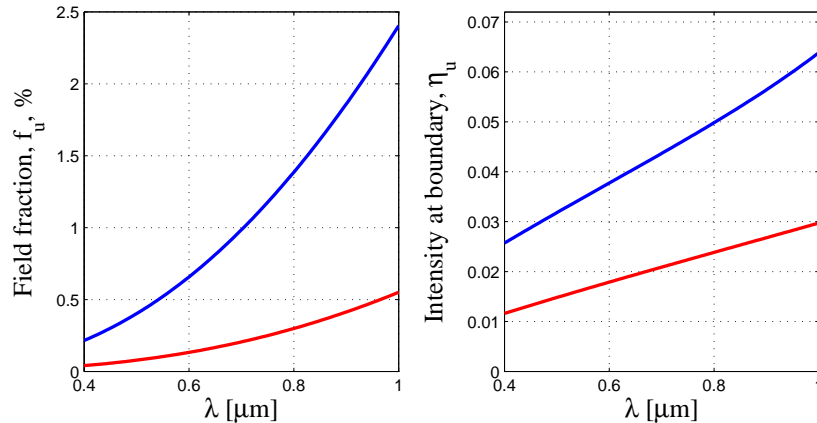
Figure 2.2: Fraction of the electromagnetic field of the PCF Air-15-1550 inside the holes filled with water (blue) and air (red) (left) as function of wavelength. The field intensity integrated at the hole interface increases linearly with wavelength for air (red) and water (blue) filled holes (right).

The speed of laser beam is typically 300-1000 mm/s and the power is 2.6-33 W. The cross section of the channel becomes Gaussian shaped as seen in Fig. 2.3 C. Some monomers are deposited on the sides of the channel creating small ridges at the edge of the channel (Fig. 2.3 A-C). At the channel terminations the depth and width deviate slightly due to a power transient in the CO_2 laser (Fig. 2.3 B). By observing Fig. 2.3 A, we realize that the sequence of the writing of different channels is important, since residues are left in the existing, crossing channels during writing. This generally implies that the largest features are to be written first, followed by the finer and more delicate features. Connections (Fig. 2.3 D-1) at the intersection of the microfluidic channel and the fibers are inscribed first as these are the largest features. The need for such a connection is not obvious. It is related to the sealing of the microsystem, and it will be explained in more detail in the following. Channels for the connecting microfluidic tubes are then written. First the part for inserting the microtubing (Fig. 2.3 D-2) and then the part connecting the tubing to the fibers (Fig. 2.3 D-3).

A

B

C

D
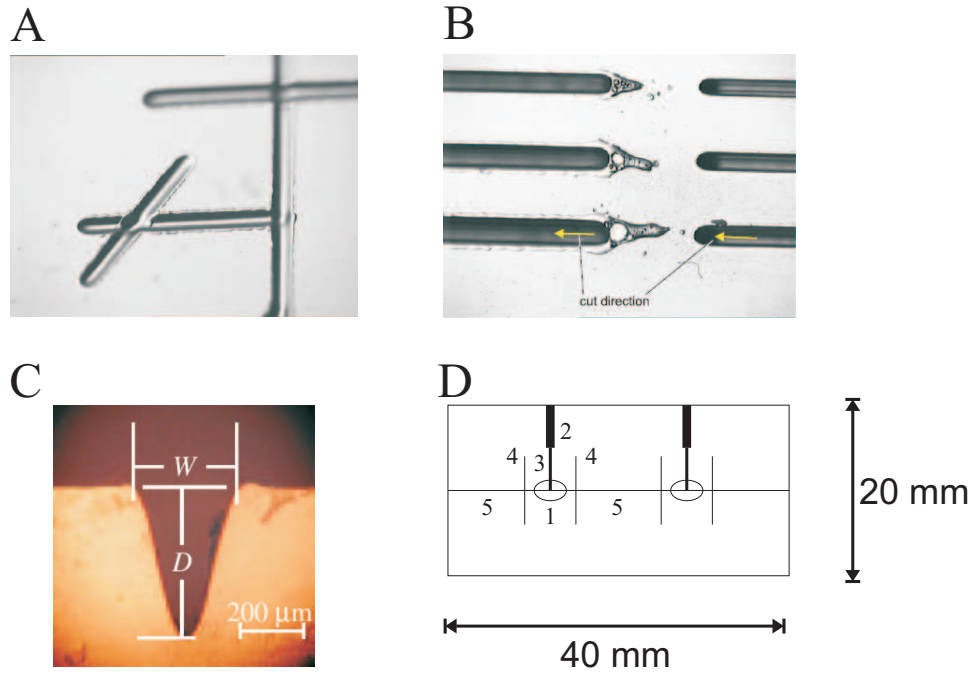
Figure 2.3: CO_2 laser marking on PMMA. The marking of a channel moves material in existing channels (A). The unstable transient of the laser deposits debris when marking is initiated (B). The channels are generally Gaussian shaped. The laser marking sequence for the chip, with the sequence of the pieces indicated by the numbers (D). A-C from Ref. [54]. Reproduced with permission.

2.2.2   Bonding and gluing

The lid on the microsystem was sealed by heat bonding [44]. The lid and the bottom is inserted into a holder with a clamp that applies a slight pressure. The microsystem is then heated to 110°C for about two hours in a convection oven. This temperature is slightly over the glass temperature of PMMA, 105°C, and allows the macro molecules certain movement, regrouping and cultivating new bonds. Achieving the right bonding is something of an art, since the chemical properties of the PMMA vary from batch to batch. The batch used for the presented microsystem was particularly difficult to bond properly, often leaving voids between the lid and bottom. Of course increasing the pressure on the clamp would ameliorate the poor bonding,

but the increased pressure leads to distortion of the delicate features of the microsystem in the hot, softened PMMA, rendering the insertion of the PCF impossible. The problem was eventually resolved by preparing the surfaces lightly with fine sandpaper followed by a wash to remove debris. The grinding also reduces the ridges at the edges of the channels, making the contact surface larger between lid and bottom and thereby improving the bonding.

The PCF, MMF, and the microtubing were secured and sealed by a two component epoxy resin. The epoxy resin is drawn into the microsystem by capillary forces. It is thus quite easy to get the resin into the system, but unfortunately, it tended to diffuse also into the tubing and the PCF. The solution was found by a neat little trick. By creating a small residue volume at the intersection of the fluidic channels, the PCF and the MMF, Fig. 2.3-D-1, the epoxy resin would infuse into the system until the intersection. The channels widen to stop the capillary flow. In this manner, the epoxy resin could be reproducibly be infused into the system by applying a small amount of resin at the entry of the tubing. The microtubes were 50 mm long with an inner diameter of 50 micron.

The same procedure were applied to the PCF and MMFs, but the resin was applied into channels (Fig. 2.3-D-4) through holes in the lid (not shown). The PCF was prepared in a 16 mm long piece. The piece was then carefully inserted into the chip by pushing it with piece of MMF. Once in place the transmittance was checked before securing the PCF and the MMFs with epoxy resin.

The total inner volume was estimated to be 0.5 μL by simple geometrical considerations. By measuring the weight before and after filling with water, it was confirmed by a milligram weight that the volume was less than 1 μL. The bonding procedure had a yield of about 50 % per batch. The subsequent gluing of fibers and microtubing also had a yield of about 50 %. The total yield was 25 %.

2.2.3 Experiments

The MMFs were connected to a halogen light source (Mikropack HL-2000) and a high resolution spectrometer (Ocean Optics Inc. HR2000). The spectrometer is highly sensitive and allowed for continuous monitoring of the absorption spectrum. The setup is outlined in Fig. 2.1. To flow fluids through the PCF in the chip a pressure was applied on the sample bottle. The inner diameter of the microtubing (50 micron) implied that the hydraulic resistance was solely due to the 16 mm of PCF. An overhead of 1 bar across

the PCF was used in the experiments. Changing solution was particularly easy. The air feed for pressurizing the sample bottle was disconnected. The solution bottle could be removed and replaced by another solution bottle.

Bio procedure

To successfully demonstrate a biosensing experiment we perform a selective capture of a target single-stranded DNA molecule. The immobilization complex shown in Fig. 2.4 is constructed inside the PCF while it is inside the biochip. The immobilization procedure involves a fairly standard technique
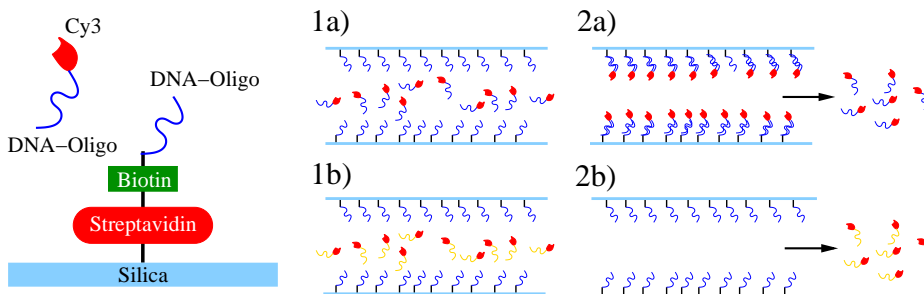
Figure 2.4: The selective DNA capture complex. Right: The complex is constructed in layers. On top of the complex is a single stranded DNA string. If a single-stranded DNA string is introduced the strings can hybridize if the DNA-sequences are complementary. The target DNA can be detected via the fluorescent marker, Cy3, by either the fluorescence or the absorption spectrum. The selective capture is illustrated in 1-2a,b. The sample is introduced. If the strings hybridize they are immobile during a subsequent wash. If the strings are non-complementary, they are washed out (2b).

where an anionic long-chained polymer is coupled to the negatively charged silica surface through a ionic bond. This is followed by a stepwise introduction of chemicals that will make the surface suitable for immobilizing DNA molecules. First, the chip is filled with poly(L-lysine) (PLL) (P8290, 1:1000 in H2O, w/v, Sigma) for 3 min by applying a 1-bar overhead. The pressure is then removed, and the chemical is allowed to work for another 7 min. Excess PLL is then removed with PBS (phosphate buffer solution) wash (10 mM NaH2PO4/Na2HPO4 pH 7.4, 150 mM NaCl) for 5 min that has not been immobilized on the silica surface. Glutardialdehyde (12.5%) which is suitable for connecting two positively charged molecules (in our

case poly(L-lysine) and streptavidin) is then introduced for 3 min at 1-bar external pressure and allowed to work for 17 min with the liquid at rest followed by a 5 min PBS wash. This is then followed by the introduction of the biotin-binding protein streptavidin (1 mg mL.1 in PBS) for 3 min at 1-bar overpressure and another 12 min without external pressure. Ethanolamine (40 mM) is used to block the empty sites on the glutardialdehyde not occupied by streptavidin, so that the following sample of biotin-labeled capture DNA does not immobilize itself outside the biotin binding site on the streptavidin. This is again followed by a 5-min wash with PBS. A 10 μM solution of biotin-labeled single-stranded DNA capture molecules (sequence 5'-biotin-CAGCGAGGTGAAAACGACAAA AGGGG) is then introduced for 3 min at 1 bar and then 12 min without external pressure. The capture complex is then complete and the chip is ready for the DNA hybridization experiment. DNA is introduced in the following with either a complementary DNA sequence (match) or non-complementary DNA sequence. The experiment is illustrated in Fig. 2.4. First a sample (10 μM) of the mismatch DNA is introduced into the capture DNA for 5 min at 1-bar overpressure and allowed to hybridize to the capture DNA for 40 min with the sample at rest. The spectrometer reads a clear absorption signal from the Cy3 fluorescent molecule with the peak at 552 nm seen in Fig. 2.4. The chip is then washed for 20 min with PBS at 1 bar. The Cy3 signal rapidly diminishes at the start of the wash. After the wash, the signal from the mismatch sample is recorded. The procedure is then repeated with the target DNA (10 μM) (Fig. 2.4, 1b2b). Transmission spectra are recorded after each step (1a, 1b, 2a, and 2b) and by comparing with the reference measurement, the absorption caused by the Cy3 molecules is derived. The results are presented in Fig. 2.5. Selectivity (match) is clearly demonstrated, in spite of some unspecific binding (mismatch). The magnitude of the absorbance (4 in Fig. 2.5) observed means that sample size, an estimated 200 pmol, of captured DNA can be reduced, possibly by a factor 100-300, to give a sample size of the order of 1 pmol. By reducing the number of holes may further increase the sensitivity by an order of magnitude, bringing the sensitivity into the fmol regime. This requires that tolerances of chip to be improved, for better alignment, possibly using a different production method. As discussed in Sec. 2.1 the capture efficiency, i.e. the probability of capturing an target molecule, is quite high due to the molecular diffusion in the confined geometry. Secondly, the optical signal collection is effective. This could promise for robust and highly sensitive optical sensor elements.
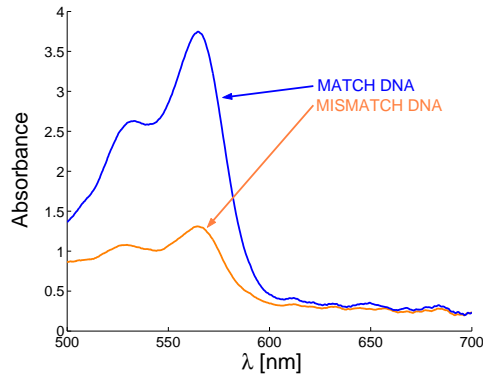
Figure 2.5: The absorbances of the match and mismatch DNA after procedures shown in Fig. 2.4.

2.3 Conclusions

The experiments show that it is possible to fabricate a biochip with a very short piece of integrated PCF for selective detection of DNA-molecules. The integration of the PCF was demonstrated for the first time. The CO_2 ablation technique is sufficiently accurate for PCFs where a large cladding structure is used for the sensing. The short piece of PCF also allows for fast response times. The microfluidics can cause problems and advantages. An improper the diameter of the holes in the PCF can make the response time of a PCF biosensor very long compared with a bulk cuvette. The capture efficiency is likely to be high inside the confined holes.
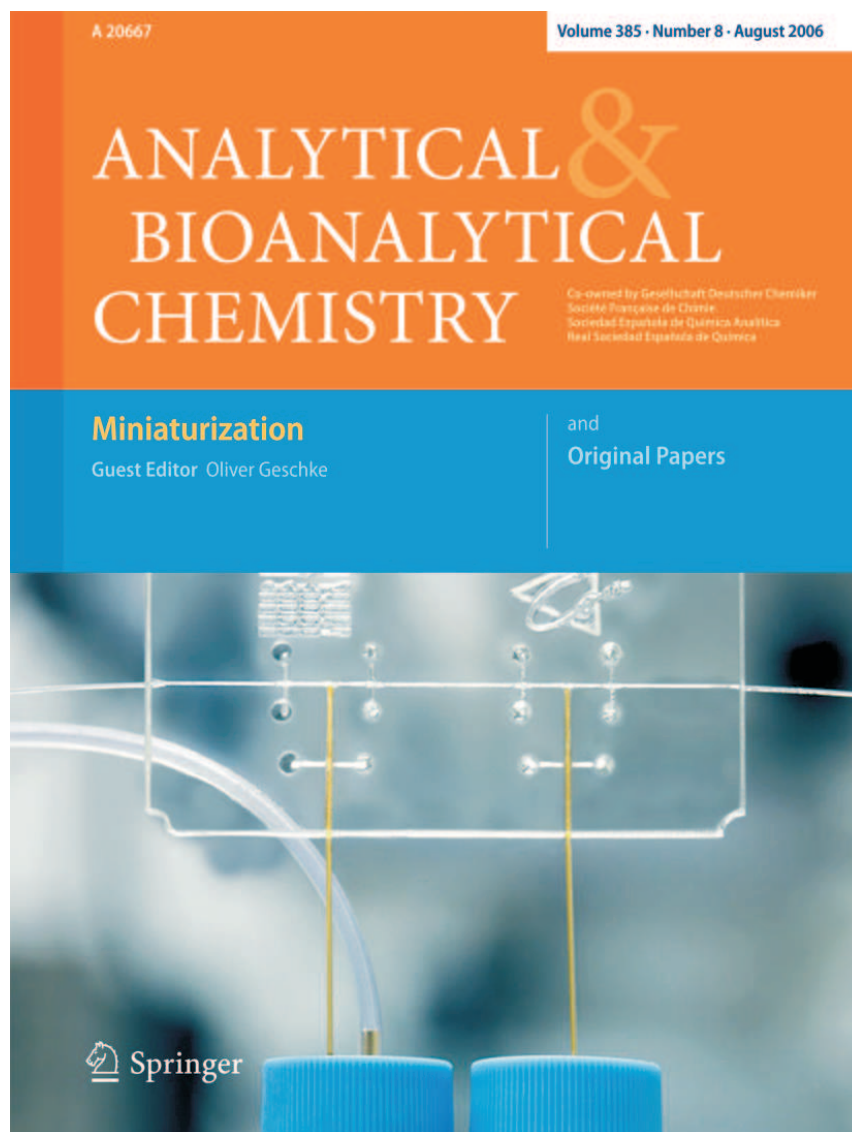
Figure 2.6: The results presented in the chapter was published in the respected journal *Analytical and Bioanalytical Chemistry* [3]. The paper was chosen to appear on the front page. Notice the department logos.

Chapter 3

Photonic crystal fibers

The performance of photonic crystal fiber (PCF) long-period grating sensors of this thesis rely heavily on the fundamental properties of PCFs. For this reason we will give an advanced introduction into the theory and modeling of PCFs. PCFs are sometimes also called microstructured optical fibers or holey fibers. PCFs can be divided into three groups according to their guiding mechanisms: photonic band-gap [55], Bragg [56], or traditional index guiding [18]. The PCFs considered in this thesis are exclusively of the index guiding type. To understand the guiding mechanism, by an analogy the lower refractive index of the cladding reflects completely the light inside the core if the angle of attack is small enough according to Snell's law.

The guiding is, however, a wave phenomenon and must be understood by studying Maxwell's equations. In a standard optical fiber the silica of the core is doped to increase the refractive index. A photonic crystal fiber does not need a doped core to guide. Rather, the optical field in the cladding experiences an artificially reduced refractive index by a periodic lattice of air holes.

Physically, optical waves are electromagnetic fields and are described by Maxwell's equations. The equations involve four vectorial fields: $\mathbf{D}$, $\mathbf{E}$ are the electric displacement and the electric field, respectively, and $\mathbf{B}$, $\mathbf{H}$ are the magnetic field and the magnetic flux density, respectively. The fields are pairwise related by the electric, $\boldsymbol{\epsilon}$, and magnetic, $\boldsymbol{\mu}$, responses of the medium of propagation: $\mathbf{D} = \boldsymbol{\epsilon}\mathbf{E}$, $\mathbf{B} = \boldsymbol{\mu}\mathbf{H}$. The responses are generally anisotropic and must be described by 3×3 tensors. In most materials the electronic response, the permittivity, dominates over the weaker magnetic response, the permeability, which can be taken to be the vacuum permeability. The dielectric media employed in the thesis are silica, air, methanol,

and water. It is desirable that the theory and conclusions also are applicable to microstructured polymer optical fibers [57]. All these materials are all isotropic, lossless dielectrica. ϵ and μ are then real scalars. Admittedly, water is also a weak electric conductor, and thus weakly lossy, but this can be modeled by adding an imaginary term to its dielectric function.

If the fields are considered as monochromatic and temporal harmonic the time dependence of any field is described by a phasor $e^{-i\omega t}$. Maxwell's equations may be written as

$$\nabla \cdot \mathbf{D}(\mathbf{r}, \omega) = 0, \tag{3.1}$$

$$\nabla \cdot \mathbf{B}(\mathbf{r}, \omega) = 0, \tag{3.2}$$

$$\nabla \times \mathbf{H}(\mathbf{r}, \omega) = -i\frac{\omega}{c_0}\mathbf{D}(\mathbf{r}, \omega), \tag{3.3}$$

$$\nabla \times \mathbf{E}(\mathbf{r}, \omega) = i\frac{\omega}{c_0}\mathbf{B}(\mathbf{r}, \omega), \tag{3.4}$$

where the vacuum permitivity, ϵ_0, and the vacuum permability, μ_0, have been replaced by the vacuum speed of light, $c_0 = 1/\sqrt{\epsilon_0\mu_0}$.
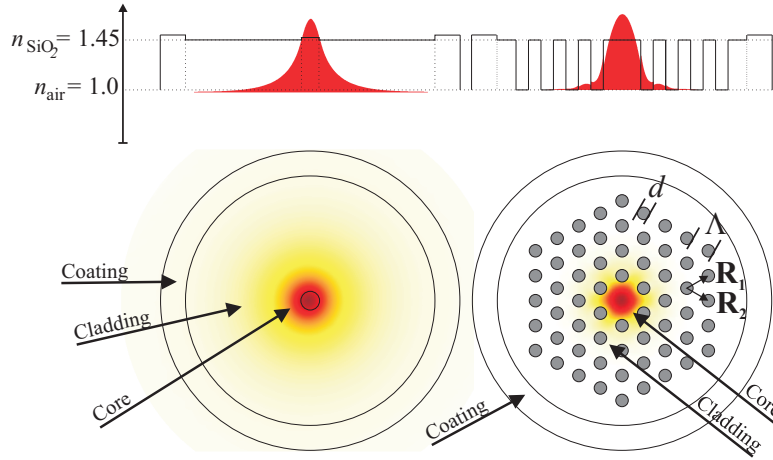
Figure 3.1: Left: a standard optical fiber. The core is doped to increase the refractive index. The fiber is coated with a polymer to obtain mechanical stability. Right: a photonic crystal fiber. The cladding refractive index is effectively decreased by a periodic lattice of air holes with the primitive lattice vectors $\mathbf{R}_1$ and $\mathbf{R}_2$. The PCF is characterized by the pitch, Λ, and the hole diameter d.

If the electronic response, ε, is independent of the field intensity, which is true for low power, Maxwell's equations describe a set of linear equations. If two fields are solutions to the equations, then any linear combination (superposition) of the field is also a solution to the equations. This will prove very useful later on. If ε is also independent of frequency, i.e. there is no *material dispersion*, then Maxwell's equations are time-position scale invariant, i.e. are invariant under the transformation $(x, y, z, t) = \alpha \times (x', y', z', t')$. The invariance is very useful when studying the qualitative properties of optical fibers, but all materials and liquids (including silica and water) have material dispersion and in accurate simulations it must be included.

Eqs. (3.3) and (3.4) can be combined to yield eigenvalue equations formulated in either the electric or the magnetic field

$$\nabla \times \nabla \times \mathbf{E}(\mathbf{r}, \omega) = \frac{\omega^2}{c_0^2} \boldsymbol{\epsilon}(\mathbf{r}, \omega) \mathbf{E}(\mathbf{r}, \omega) \tag{3.5}$$

$$\nabla \times \boldsymbol{\epsilon}^{-1}(\mathbf{r}, \omega) \nabla \times \mathbf{H}(\mathbf{r}, \omega) = \frac{\omega^2}{c_0^2} \mathbf{H}(\mathbf{r}, \omega), \tag{3.6}$$

which must be solved under the constraints of either zero free charge, $\nabla \cdot \mathbf{D} = 0$, or zero divergence, $\nabla \cdot \boldsymbol{\mu} \mathbf{H} = 0$, respectively. In a PCF the dielectric function, $\varepsilon = \epsilon/\epsilon_0$, takes on different constant values in the different materials of the PCF. ϵ_0 is the vacuum permittivity. At the boundary the function is discontinuous. Of course, such jumps are microscopically unphysical since the electronic response can not be discontinuous according to Quantum Mechanics. Nevertheless, at a macroscopical scale, the interface is well described by a discontinuous function. At boundaries this results to a boundary condition for the fields. The magnetic field is continuous at the boundaries, but its derivatives are not necessarily continuous. The electric field is generally discontinuous: the components transverse to the boundary are continuous and the component normal to the boundary is discontinuous. Discontinuous functions require special considerations in numerical implementations.

3.1 Characterization of optical fibers

An incident electromagnetic field on the end of an optical fiber excites a number of waves which are either guided or radiative. The transient radiative solutions decay leaving the guided waves, *modes*. An illustrative analogy is the Quantum Mechanical example of a particle in box where only standing wave solutions are allowed. In terms of the electric field, the electromagnetic

field can be described as a superposition of different modes

$$\mathbf{E}(\mathbf{r}, t) = \sum_{m=1}^{\infty} \int_0^{\infty} \mathrm{d}\omega \, \mathbf{E}_m(\mathbf{r}_\perp, \omega) \, e^{i(\beta_m z - \omega t)}, \qquad (3.7)$$

where the fiber axis is assumed to be parallel to the z-axis, $\mathbf{r}_\perp = (x, y)$, and β_m is the propagation constant of the mode m. Usually one is interested in that the optical fiber is *single-mode* to avoid intermodal dispersion and mode mixing.

From the propagation constant, β, the *effective index* is defined as

$$n_{\mathrm{eff}} = \frac{c_0}{v_\mathrm{p}} \equiv c_0 \frac{\beta}{\omega}, \qquad (3.8)$$

describing the phase velocity, v_p, of the mode relative to vacuum speed of light. A wave envelope propagates with the group velocity, v_g, related to the group index, n_g, by

$$n_\mathrm{g} = \frac{c_0}{v_\mathrm{g}} = \frac{\partial \beta}{\partial k} = n_{\mathrm{eff}} - \lambda \frac{\partial n_{\mathrm{eff}}}{\partial \lambda}. \qquad (3.9)$$
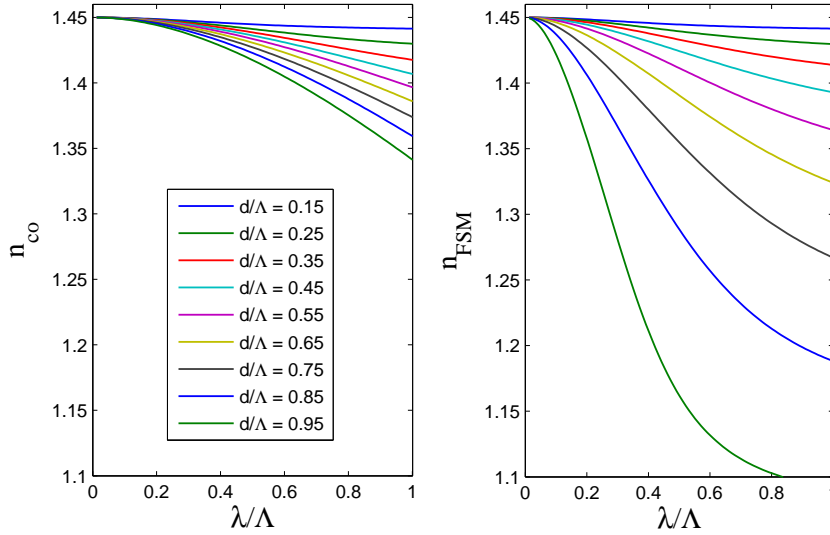
Figure 3.2: The effective index of the core (left) and fundamental space filling mode (right), for various values of the wavelength, λ, and hole diameter, d, relative to the pitch, Λ.

The chromatic group velocity dispersion can be expressed as

$$D_{\mathrm{g}} = \frac{\partial(1/v_{\mathrm{g}})}{\partial\lambda} = \frac{1}{c_0}\frac{\partial}{\partial\lambda}\frac{\partial\beta}{\partial k} = -\frac{\lambda}{c_0}\frac{\partial^2 n_{\mathrm{eff}}}{\partial\lambda^2}. \tag{3.10}$$

$D_{\mathrm{g}} > 0$ is called normal dispersion (negative curvature of n_{eff}), and $D_{\mathrm{g}} < 0$ is called anomalous dispersion (positive curvature of n_{eff}).

3.1.1 Triangular photonic crystal fibers

The most common index guiding PCF is the triangular seen in Fig. 3.1. The structure is described by the irreducible lattice vectors $R_1 = \frac{1}{2}(\sqrt{3}, 1)$, $R_2 = \frac{1}{2}(\sqrt{3}, -1)$. The core is formed by leaving out a single hole in the center of the PCF. In Fig. (3.2) the effective index of the fundamental core mode and the fundamental space filling mode of a PCF is shown. The fundamental space filling mode is the highest effective index mode propagating in an infinite cladding structure. The effective index is seen to decrease with the wavelength and with increasing diameters of the holes. In the short wavelength limit the field is confined to the high index material (base index n_b) [?], $n_{\mathrm{eff}} = n_b$, $\lambda \ll \Lambda$ ($\omega \gg c_0 2\pi/\Lambda$), which is confirmed by Fig. 3.2. In the long wavelength limit, the effective index of the electromagnetic fields tends to a uniform distribution in the structure, and thus by the paraxial approximation, where vectorial effects are neglected we, have $n_{\mathrm{eff}} \simeq (1 - f)n_b + n_h$, $\lambda \gg \Lambda$ ($\omega \ll c_0 2\pi/\Lambda$), where n_h refractive index of the hole material, f ($\neq f_u$) is the air filling factor, indicating the fraction of air in the fiber cross section. Triangular PCFs have the special property that they can designed to guide only a single (degenerate) fundamental core mode for all wavelengths if the hole diameter is smaller than a critical value, $d_{\mathrm{c}}/\Lambda \simeq 0.42$. This has been shown by Mortensen *et al.* [59?] using numerical and semianalytic approaches and Kuhlmey *et al.* [60, 61] using the highly accurate multipole method [62, 63]. It has also been shown that if the wavelength is larger than a critical value,

$$\lambda_{\mathrm{c}}/\Lambda > 2.8 \times (d/\Lambda - 0.42)^{0.89}, \tag{3.11}$$

then the PCF will be single mode even when the hole diameter is larger than the critical value, 0.42. In practice, PCFs are effectively single mode even when the theoretical criterion is not fulfilled due to the weak guiding of the higher order modes. For large mode area PCFs one prefers a higher relative hole diameter of $0.45 - 0.50$, since the PCF is less susceptible to bend losses. At the short wavelengths there exist a wavelength cut-off, λ_{c}, below which

the PCF becomes highly lossy. The cut-off is related to the bend radius, R_c, by [64]

$$\frac{R_c}{\Lambda} \propto \frac{\Lambda^2}{\lambda_c^2}. \tag{3.12}$$

The prefactor is of the order of unity for a relative hole diameter of ~ 0.5. The susceptibility of an optical fiber to microdeformation losses [65] can be indicated by the beat length, $L_B = 2\pi/(\beta_{co} - \beta_{FSM}) = \lambda/(n_{co} - n_{FSM})$, between the core and fundamental space filling mode. A short beat length, i.e. large spacing between the modes, gives a low susceptibility. The large spacing can be created by large air holes or small pitch (Fig. 3.2). Increasing the difference between the core and fundamental space filling modes changes the number of guided modes.

Optical fibers also experience attenuation even in absence of bend losses, due to absorbtion and confinement losses. For weak losses ($\alpha\lambda \ll 1$) this can be described an exponential decay $I(z) \propto |E|^2 \propto \exp(-\alpha z)$, where the attenuation constant, α, is usually given in decibels per length $\alpha_{dB/cm} \simeq -8.7\,\mathrm{Im}[\beta] = -8.7\,\mathrm{Im}[n_{eff}]\frac{2\pi}{\lambda}$, and is proportional to the imaginary part of the propagation constant and effective index.

3.1.2   Symmetry of PCF optical modes

Triangular PCFs obey a six-fold rotational symmetry and inversion symmetry, C_{6v}. Through group theory the symmetry may be used to reduce the size of the computational domain, but it can also be used to categorize the modes [66, 67]. Most importantly, it provides knowledge of which modes are degenerate, i.e. different field solutions, e.g. polarizations, with the exact same propagation constant. The core mode of a triangular PCF is degenerate in theory which has also been verified numerically [68]. Symmetry enables the computational domain to be reduced by at least a factor of four (Fig. 3.3).

The modes can be identified by the outer boundary conditions: perfect electric conductor, ($\mathbf{n} \times \mathbf{E} = 0$), or perfect magnetic conductor, ($\mathbf{n} \times \mathbf{H} = 0$), as indicated in Fig. 3.3. While symmetry helps categorizing the modes, it does not provide any knowledge of the ordering of the modes. For a PCF with hole diameter $d/\Lambda = 0.6$ six modes are guided in the core. Their mode fields are seen in Fig. 3.4. The four higher order modes appear four fold degenerate both in experiment and numerically [69]. According to Group Theory they are only two-fold degenerate, but their effective indices are closely spaced. For a single mode PCF it may be anticipated that the

lowest cladding order modes share the same symmetry as the higher order core modes in Fig. 3.4.

Normally modes propagating in the bulk silica cladding and in the microstructured part of cladding are called cladding modes. In this work the modes propagating in the bulk material are called *bulk modes*, reserving the term *cladding modes* for modes propagating, at least partially, in the cladding structure.

3.2   Numerical methods

For the computational physicist the eigenvalue problems posed by Eqs. (3.5-3.6) may seem trivial at first sight: the problems are linear and Hermitian under the condition that the material is lossless, ($\text{Im}[\varepsilon]{=}0$). In fact, their solution is complicated by three facts: the eigenvalues (effective indices) are very closely spaced, the solutions must be divergence free and, more importantly, the fields and their derivatives are not continuous at boundaries,
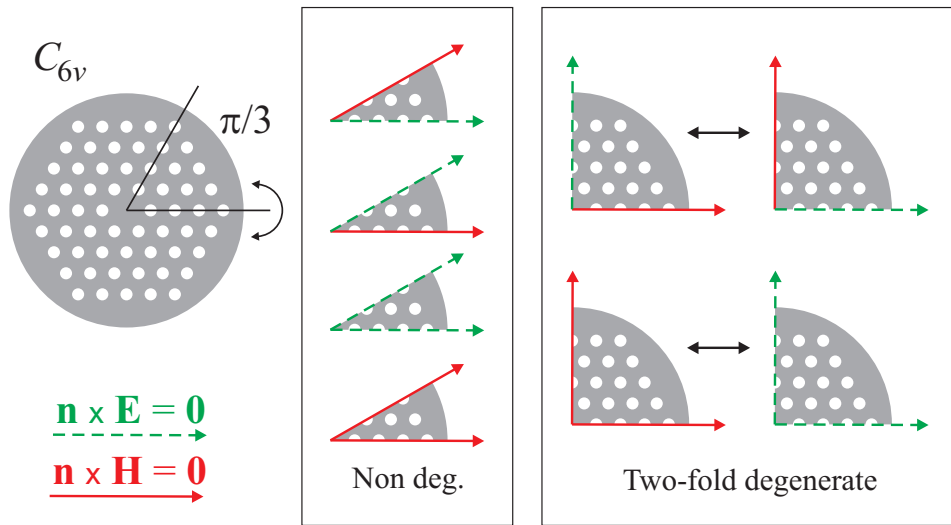
Figure 3.3: A triangular PCF obeys a six-fold rotation and inversion symmetry. The modes are group into non-degenerate modes (center box), or pairwise degenerate modes (right box) satisfying the boundary conditions perfect electric conductor ($\mathbf{n} \times \mathbf{E} = \mathbf{0}$) or perfect magnetic conductor ($\mathbf{n} \times \mathbf{H} = \mathbf{0}$). The fundamental core mode belongs to the top pair in the right box.
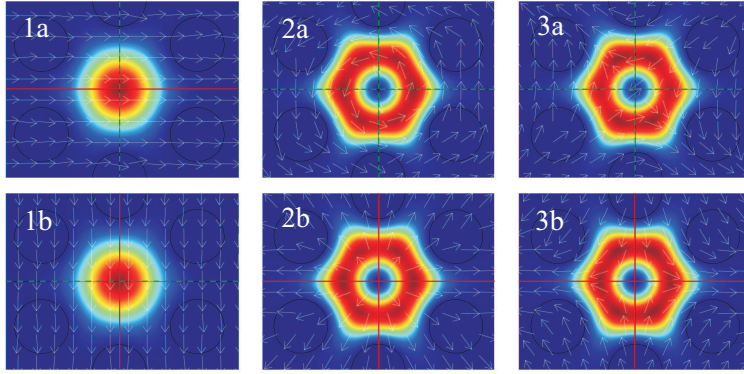
Figure 3.4:   Guided core modes for a PCF with $d/\Lambda = 0.6$. z-comp. of Poynting vector, P_z, and the transverse electric field (vectors). The fundamental core mode x (1a) and y (1b) polarized. LP01 (HE11) like. The second lowest guided core modes (2a-2b). LP11: TE01 (1a) and HE21 (1b) like. The third lowest guided core modes (3a-3b). LP11: HE21 (3a) and TM01 (3b) like. The modes constitute degenerate pairs (top and bottom). In practice, the center and right modes all appear degenerate.

requiring special mathematical measures.

For modeling PCF there exist various simple methods, such as the effective index method and the scalar approximation. For long-period gratings a high accuracy is needed for predicting the resonance wavelength. To estimate the accuracy consider a resonant wavelength of $\lambda_r = 1\,\mu$m and a grating
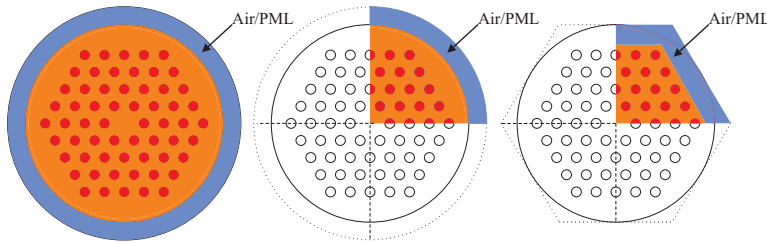
Figure 3.5: The computational domain. An optional perfectly matched layer (PML) can be added at the outer boundary of the PCF. Symmetry may be used to reduce the domain (center). In practice, excess bulk outside the air holes may be removed (right) without spurious effects.

period of $\Lambda_{\mathrm{G}} = 500$ μm, we get from the resonance condition Eq. (4.12) an index difference $n_{\mathrm{co}} - n_{\mathrm{cl}} \sim 0.002$. If the uncertainty on the resonant wavelength is 5 nm, then the precision of the effective index should be at least, (5 nm/1μm) $\times$ $(n_{\mathrm{co}} - n_{\mathrm{cl}}) \sim 10^{-5}$. Such a precision can only be achieved using rigorous fully vectorial modeling. Fortunately, several implemented methods are available. The most common are the plane-wave method (PWM) and the finite element method (FEM).

In the beginning of the Ph.D. project the PWM was used with the freely available MIT Photonics Bands (MPB) [70]. Later, a shift was made to the FEM, using a commercial implementation by Comsol [71], since FEM was found to be superior to PWM.

The computational domain of the cross section of the PCF is finite and this requires boundary conditions at the outer boundaries of the domain. One solution is to impose perfect electric conductor ($\mathbf{n} \times \mathbf{E} = \mathbf{0}$) or perfect magnetic conductor ($\mathbf{n} \times \mathbf{H} = \mathbf{0}$) at the outer boundaries of the PCF. This can result in spurious reflections from the boundary, since the perfect electric or magnetic conductor boundary condition is essentially unphysical for the problem at hand. The problem may be alleviated by including a layer air with a lower refractive index than the bulk silica, Fig. 3.5. This reduces the reflections. In reality the light leaves the PCF and is absorbed in the surroundings leading to so-called confinement losses. One way of treating this problem is using perfectly matching layers (PMLs). In the PML a complex coordinate transformation is performed, which can be made such that no spurious reflections arise from any wave incident at PML (Fig. 3.5). For modes which are guided by the core of the PCF the bulk silica around the microstructure may be removed, greatly reducing the numerical task.

3.2.1 The finite element method

FEMs are becoming increasingly widespread in the recent years. The method divides the domain of the cross section of an optical fiber into a number of finite elements, hence the name. Inside these elements the solution is typically approximated by a polynomial, although other, more exotic, elements also exist. The finite element method is mathematical very well founded in functional analysis [72]. The reader is referred to Brenner and Scott for the mathematical foundations of FEM [73] and Jin for the implementation of electromagnetics in FEM [74].

FEM simulation of waveguide problems dates back to 1968 [75], and since then it has been pursued by a number of research groups. Some prominent contributors are Koshiba [76], Rahman [77], Selleri [78], and Geuzaine [79,

80].

The FEM handles the discontinuous fields mathematically consistently and there exist very efficient eigenvalue solvers for FEMs. The eigenvalue problem is discretized into a matrix problem. For real space FEM the elements of the matrix are almost all zero, and the problem can be made sparse. Solvers for sparse problems fare well both in terms of convergence and time-consumption. The time consumption as function of the number of dependent variables, N, scales very favorably as $\mathcal{O}(N)$. This also makes the solution of large systems accurate, and the solution can be made arbitrarily accurate by increasing the number of finite elements.

The FEM is very flexible and complex refractive indices and a range of boundary conditions and PMLs can be used. Furthermore, in the COMSOL implementation the user can modify the governing equations at will.
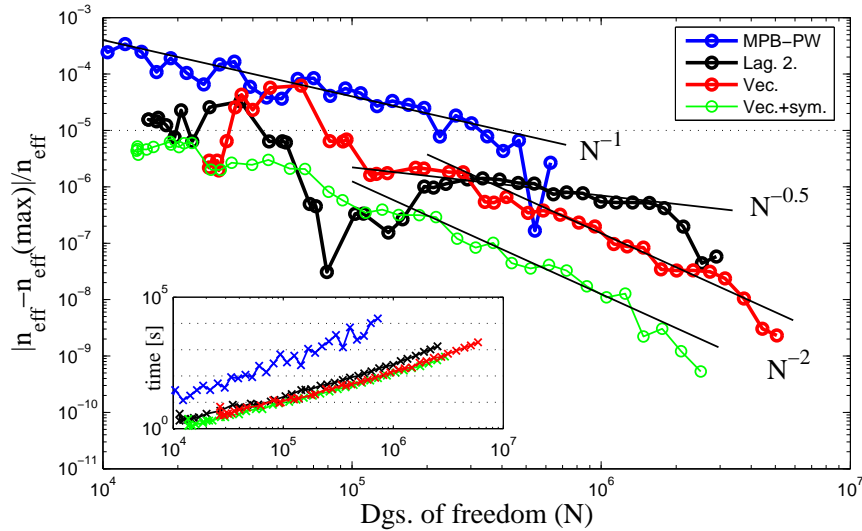
Figure 3.6: Convergence of the effective index of a core mode using different FEM and PWM. 'Lag. 2': second order Lagrange elements. 'Vec.': vector elements. 'Vec.+sym': using the C_{6v} symmetry of the PCF and vector elements. Inset: time consumption of the methods. The computers have similar processor performance.

Method	n_{eff}	conv(n_{eff})	DOF
PW (MPB)	1.4485613057	8×10^{-6}	723243
FEM (COMSOL), Lag.	1.4485774433	6×10^{-7}	3371224
FEM (COMSOL), Vec.	1.4485767719	6×10^{-9}	5899642
FEM (COMSOL), Vec.+sym.	1.4485767651	2×10^{-9}	2955456
Multipole (CUDOSMOF)	1.4485769528	1×10^{-13}	N.A.

Table 3.1: The n_{eff}(max) values used in Fig. 3.2. conv(n_{eff}) is the estimated convergence error at the highest DOF. DOF is the number of degrees of freedom.

Finite elements

One innovation that has significantly improved the performance of the FEM is the so-called vector element. Typically Lagrange elements are used for any problem. Lagrange elements are the most common and intuitive, and are polynomial fit to the field inside each elements of each component of the vector field. In an implementation with Lagrange elements the z-component of the field is usually eliminated by the divergence condition, $H_z = -\nabla_\perp \cdot \mathbf{H}_\perp/(i\beta)$, which is then inherently fulfilled. The implementation gives a boundary condition that involves also the derivatives of the fields. The derivatives of fields are more prone to error than fields. The precision of the eigenvalue increases with the inverse of the number of elements squared for quadratical Lagrange elements.

The vector element, or edge element as it is sometimes referred to, describes the two in-plane components of the field by describing the vector field along its edges. The transverse components are continuous across the elements, whereas the normal components are free variables. The element is well suited for the electromagnetic field which transverse component is continuous and which normal components may be discontinuous. The evaluation of the curl of a field with the vector element is related to the highly successful Yee grid used in finite difference time domain methods [81]. When using vector elements a mixed formulation is used with vector elements for the transverse field components and the Lagrange elements for the z-component of the field.

3.2.2 Planewave methods

Spectral methods using Fast Fourier Transforms (FFTs) and plane-waves have commonly been used to simulate photonic crystal fibers [82]. The

method has a number of advantages: it is simple to implement and to understand, it is fast for small systems, and it is available freely in the MIT Photonics Bands package MPB [70] written by Johnson *et al.* [83]. The method makes use of Bloch's theorem (also known as Floquet's theorem to mathematicians), and solves Eq. (3.6) by using Fast-Fourier Transforms. The implementation has manifestly periodic boundary conditions, but the images may be decoupled by using a sufficient large computational domain to simulate e.g. localized mode in PCFs. In $\mathbf{k}$-space the curl operations on the left hand side of Eq. (3.6) are exactly evaluated, as they are equal to the cross product of $i\mathbf{k}$ and the magnetic field. Unfortunately, the discretized eigenvalue matrix can not be made sparse as in FEMs. The time consumption scales as $\mathcal{O}\big(N \log(N)\big)$, where N is the number of plane-waves used. This is nearly as good as the linear scale of the FEM. The spectral method achieves very fast convergence in the number of plane-waves grid if the solution belongs to the class of infinitely differentiable functions. The magnetic field is only C^1, i.e. its derivatives may be discontinuous. This implies that the accuracy of the eigenvalue increases only linearly in the number of plane-waves [72]. To avoid poor convergence and accuracy the discontinuous dielectric function is smoothed at material interfaces. Although the magnetic field should be C^2 when the dielectric function is smoothed at the material interfaces, I have been unable to reproduce this numerically. This lack of convergence has also been observed by Johnson *et al.*[83].

The numerical problems are attributed to two facts: the plane waves are *non-local* functions, and the optical modes of a fiber are *localized* states. Secondly, the plane waves, being continuous functions handle the discontinuities at the boundaries poorly. The convergence of the PWM solvers is not good and this has been known for a long time [84], and for a large system it can fail to converge the problem.

3.2.3 Numerical benchmarking

As a test it is chosen to model a PCF with seven rings of air holes surrounding the core, a pitch of $\Lambda = 7$ μm, a relative hole diameter of $d/\Lambda = 0.45$, and a wavelength of $\lambda = 1$ μm. The PCF is implemented in both COMSOL and MPB. In COMSOL there are three implementations: Lagrange elements, solving only for the in-plane components, vector elements with and without using the symmetry of the PCF structure (Fig. 3.3). The FEM mesh consists in all simulations of elements of roughly equal size. There is no refinement of the mesh at the material interfaces. The FEM solves directly for the propagation constant. In MPB the numerical settings as following.

The problem is implemented in a unit cell with 14 Λ distance between the cores. The smoothing of the epsilon is set to 'mesh-size = 13'. Space-time inversion symmetry is exploited with the command 'mpbi'. The program solves for the frequency, but is set to indirectly calculate the propagation constant (command: find-k), by finding the appropriate frequency to a given propagation constant.

The COMSOL simulations were run on the HPC application server (Sun High Performance Computing Systems) DTU on a 1.3 GHz processor, and the MPB simulations were run on a 1.3 GHz PC with 775 MB of RAM.

As a reference the effective index is also calculated with the highly accurate multipole method, CUDOSMOF [85]. It is clearly seen in Fig. 3.6 that COMSOL converges as N^{-2} for the vector elements, and $N^{-0.5}$ for the Lagrange elements, whereas the MPB converges as N^{-1}. The MPB simulations failed to converge in 10,000 iterations beyond 723243 degrees of freedom. The required time for a calculation with 10^{-5} accuracy of the effective index is 10^4 s $\sim$ 3 hours with the PWM and 15 s with the FEM using vector elements and symmetry. The fall off seen in all curves for high degrees of freedom is due to the fact the highest number of degrees of freedom is used as the fully converged value. The highest converged values are presented in Table 3.1. The estimated convergence error, $\text{conv}(n_{\text{eff}})$, is obtained by fitting a power law function to the convergence data in Fig. 3.6, and then plugging in the highest number of degrees of freedom in this function. In the plot the dashed line indicates the required precision for the problems at hand. It is seen that MPB just barely reaches this limit. The inferior performance of the PWM has also been observed by Szpulak *et al.* [86]. The implementation of COMSOL runs approximately 5.5 times slower on the HPC serves than on my PC, due to a suboptimal installation of the program. I have taken the liberty to correct this and divide the actual times with this factor, since it is an artefact of the installation and not the program itself.

3.3   Summary

The fundamentals of PCFs within theory and numerics have been presented. The six-fold rotation and inversion symmetry of triangular PCF allows for a reduction of the computational domain by a factor of four and thus for faster computations. The finite element method has been benchmarked against the plane-wave method. The finite element method provides the accuracy for the required simulations while the plane-wave method fails. The time

require for calculating the effective index with 10^{-5} accuracy was 3 hours with the PWM and 15 s with the FEM.

Chapter 4

Long-period fiber gratings

When two modes propagate in a fiber the amplitude of the superposed modes beats with a characteristic length, known as the beat length: $L_{\mathrm{B}} = 2\pi/(\beta_{\mathrm{co}} - \beta_{\mathrm{cl}})$. Here the two modes are taken to be the core (co) and a cladding (cl) mode, but beating can in principle occur between any two modes or between the two polarizations of the same mode. By perturbing the fiber with a period matching the beat length it is possible to couple the two modes resonantly. The cladding modes are lossy, and the beating between the core and cladding mode can be identified in the spectrum as attenuation dips. By choosing the period and the size of the perturbation the position and depth of the dip may be controlled. This phenomenon can be described theoretically using Coupled-Mode Theory (CMT). CMT is a simple and remarkably efficient tool for simulating uniform fiber gratings. Fiber gratings can be grouped in two: long period gratings (LPGs) and Bragg gratings (BGs). In LPGs a core mode is coupled to a co-propagating cladding mode. In BGs a core mode is coupled to the counter propagating core mode. We will not treat the BG in further detail in this work.

Often CMT is based on somewhat heuristic arguments. For this reason we make a rigorous derivation based on the derivation by Yariv [87, 88].

4.1   Coupled mode theory

As a starting point the electric field is written as a superposition of the core mode and a resonant cladding mode, m,

$$\mathbf{E}(\mathbf{r}) = a_{\mathrm{co}}(z)\mathbf{E}_{\mathrm{co}}(\mathbf{r}_{\perp})e^{i\beta_{\mathrm{co}}z} + a_{\mathrm{cl}}(z)\mathbf{E}_{\mathrm{cl}}^{(m)}(\mathbf{r}_{\perp})e^{i\beta_{\mathrm{cl}}z}, \qquad (4.1)$$

where $\mathbf{E}_{\text{co}}$ and $\mathbf{E}_{\text{cl}}^{(m)}$ are the unperturbed modes of the fiber and $a_{\text{co}}, a_{\text{cl}}$ are the complex amplitude coefficients. In the following the superscript index on the cladding mode field is omitted for simplicity. In absence of a grating, or any other perturbation, such as bending or structural imperfections, any power launched into the core or cladding mode will remain in the mode by virtue of the eigenvalue equation. The cladding mode, however, attenuates over some centimeters. Ignoring the leaky nature of the cladding modes for now, the coefficients a_i will be constant with respect to z in absence of a grating. If we introduce some weak isotropic perturbation, $\Delta\varepsilon(\mathbf{r})$, to the dielectric function, we may couple the two modes. Assuming the perturbation to be periodic with the grating period, Λ_{G}, we may without loss of generality write $\Delta\varepsilon$ as a Fourier expansion

$$\Delta\varepsilon(\mathbf{r}_\perp, z) \;\; = \;\; \sum_{p=-\infty}^{\infty} \Delta\varepsilon_p(\mathbf{r}_\perp) e^{ip\frac{2\pi}{\Lambda_{\text{G}}}z}, \tag{4.2}$$

where $\Delta\varepsilon_p(\mathbf{r}_\perp)$ is p'th Fourier component of $\Delta\varepsilon(\mathbf{r}_\perp, z)$.

Since the unperturbed eigensolutions to Eq. (3.5) are assumed known we may simplify the governing equation before proceeding. Using $\nabla \times \nabla \times \mathbf{E} = -\nabla^2\mathbf{E} + \nabla(\nabla\cdot\mathbf{E})$ and that the unperturbed modes are divergence free inside the domains, $\nabla \cdot (\varepsilon\mathbf{E}) = \varepsilon\nabla \cdot \mathbf{E} = 0$, we obtain a set of three uncoupled, scalar equations,

$$(\nabla_\perp^2 + \frac{\mathrm{d}^2}{\mathrm{d}z^2})\mathbf{E}(\mathbf{r}) + k^2\Big[\varepsilon(\mathbf{r}_\perp) + \sum_{p=-\infty}^{\infty} \Delta\varepsilon_p(\mathbf{r}_\perp)e^{ip\frac{2\pi}{\Lambda_{\text{G}}}z}\Big]\mathbf{E}(\mathbf{r}) = 0. \tag{4.3}$$

The unperturbed eigensolutions are orthonormal with the inner product

$$\int \mathrm{d}\mathbf{r}_\perp \mathbf{E}_m^\dagger(\mathbf{r}_\perp) \cdot \mathbf{E}_n(\mathbf{r}_\perp) = \delta_{mn}, \quad m, n \in \{\text{co,cl}\}. \tag{4.4}$$

Inserting the superposition given by Eq. (4.1) into Eq. (4.3) gives a differential equation. The equation may be simplified by each eigenmode satisfying the eigenvalue equation $a_m(z)e^{i\beta_m z}\big[(\nabla_\perp^2 - \beta_m^2)\mathbf{E}_m(\mathbf{r}) + k^2\varepsilon(\mathbf{r}_\perp)\big]\mathbf{E}_m(\mathbf{r}_\perp) = 0$. The slowly varying amplitude approximation is employed

$$\Big|\frac{\mathrm{d}^2 a_m(z)}{\mathrm{d}z^2}\Big| \ll \beta_m\Big|\frac{\mathrm{d}a_m(z)}{\mathrm{d}z}\Big| \tag{4.5}$$

which physical interpretation is that the mode conversion by the grating is slower than the harmonic oscillation by the propagation constants, β_i. The

phase matching approximation keeps the oscillating terms closest to resonance, which are assumed to be the zeroth and the p'th Fourier component. These approximations results in a differential equation,

$$i2\beta_{\text{co}}\frac{\mathrm{d}a_{\text{co}}(z)}{\mathrm{d}z}e^{i\beta_{\text{co}}z}\mathbf{E}_{\text{co}}(\mathbf{r}_\perp) + i2\beta_{\text{cl}}\frac{\mathrm{d}a_{\text{cl}}(z)}{\mathrm{d}z}e^{i\beta_{\text{cl}}z}\mathbf{E}_{\text{cl}}(\mathbf{r}_\perp)$$

$$+k^2\Delta\varepsilon^{\text{AC}}(\mathbf{r}_\perp)e^{\pm ip\frac{2\pi}{\Lambda_\text{G}}z}\Big[a_{\text{co}}(z)e^{i\beta_{\text{co}}z}\mathbf{E}_{\text{co}}(\mathbf{r}_\perp) - a_{\text{cl}}(z)e^{i\beta_{\text{cl}}z}\mathbf{E}_{\text{cl}}(\mathbf{r}_\perp)\Big]$$

$$+k^2\Delta\varepsilon^{\text{DC}}(\mathbf{r}_\perp)\Big[a_{\text{co}}(z)e^{i\beta_{\text{co}}z}\mathbf{E}_{\text{co}}(\mathbf{r}_\perp) - a_{\text{cl}}(z)e^{i\beta_{\text{cl}}z}\mathbf{E}_{\text{cl}}(\mathbf{r}_\perp)\Big] = 0. \quad (4.6)$$

The superscripts 'AC' and 'DC' originate in electric engineering, and indicates that the Fourier components are either oscillating or constant, respectively. The differential equation can be turned into two linear coupled equations by using the orthonormality of the electric fields, Eq. (4.4), to, in turn, multiply the differential equation with the eigensolutions and integrate over the cross section of the fiber. By multiplying the amplitude coefficients with a phase factor, $\hat{a}_i(z) = e^{i\sigma_i z}a_i(z)/\sqrt{\beta_i}$, a particular simple form is obtained. The physical meaning assigned to σ_i will soon become apparent. The coupled differential equations may be expressed in matrix form as

$$\left[\begin{array}{c}\frac{\mathrm{d}\hat{a}_{\text{co}}(z)}{\mathrm{d}z}\\\frac{\mathrm{d}\hat{a}_{\text{cl}}(z)}{\mathrm{d}z}\end{array}\right] = -i\left[\begin{array}{cc}0 & \kappa e^{i\delta z}\\\kappa^* e^{-i\delta z} & 0\end{array}\right]\left[\begin{array}{c}\hat{a}_{\text{co}}(z)\\\hat{a}_{\text{cl}}(z)\end{array}\right], \quad (4.7)$$

where we have introduced the detuning, δ, the coupling constant, κ, and the self-coupling constant, σ_i,

$$\delta \equiv \beta_{\text{co}} - \beta_{\text{cl}} + \sigma_{\text{co}} - \sigma_{\text{cl}} - m\frac{2\pi}{\Lambda_G} \quad (4.8)$$

$$\kappa \equiv \frac{k^2}{2\sqrt{\beta_{\text{co}}\beta_{\text{cl}}}}\int\mathrm{d}\mathbf{r}_\perp\mathbf{E}_{\text{co}}^*(\mathbf{r}_\perp)\Delta\varepsilon^{\text{AC}}(\mathbf{r}_\perp)\mathbf{E}_{\text{cl}}(\mathbf{r}_\perp), \quad (4.9)$$

$$\sigma_n \equiv \frac{k^2}{2\beta_i}\int\mathrm{d}\mathbf{r}_\perp\mathbf{E}_n^*(\mathbf{r}_\perp)\Delta\varepsilon^{\text{DC}}(\mathbf{r}_\perp)\mathbf{E}_n(\mathbf{r}_\perp), \quad n = \text{co, cl}. \quad (4.10)$$

The detuning describes how close the system is to resonance. The magnitude of coupling constant describes the strength of the gratings. The self-coupling constant describes the change to the individual propagation constant caused by the perturbation. The variable p indicates the harmonic order of the 'AC' term $\Delta\varepsilon^{\text{AC}} = \Delta\varepsilon_p$. Usually, $p = \pm 1$ but higher order harmonic resonances are sometimes seen (see e.g. Fig. 4.13).

At resonance, $\delta = 0$, the propagation constants may be replaced by the effective indices to obtain the resonance condition,

$$\lambda = (n_{\text{co}} - n_{\text{cl}} + \Delta n_{\text{co}} - \Delta n_{\text{cl}})\Lambda_\text{G}, \quad (4.11)$$

where we have introduced $\Delta n_m = \sigma_m/k \simeq \int_\Omega \mathrm{d}\mathbf{r}_\perp \mathbf{E}_m^\dagger(\mathbf{r}_\perp)\langle\Delta n(\mathbf{r}_\perp,z)\rangle_z \mathbf{E}_m(\mathbf{r}_\perp)$, with $\Delta\varepsilon = \Delta(n^2) \simeq 2n\Delta n$, to show that the self-coupling terms correspond to the average change in effective index caused by the inscription of the grating. We will neglect these terms in the following for both quantitative and qualitative reasons. The self-coupling terms correspond to a shift of the resonance wavelength. In practice, the shifts of the resonance wavelength are only a couple of nanometers, and we are satisfied with predicting the resonance wavelength within 5 nm. When used as a sensor the self-coupling terms do not change[1], and they do not provide us with any understanding of the physical mechanisms involved in grating sensors. The resonance condition then reduces to

$$\lambda_\mathrm{r} = (n_\mathrm{co} - n_\mathrm{cl})\Lambda_\mathrm{G}, \tag{4.12}$$

which is in agreement with the intuitive assumption that the grating period should match the beat length, $\Lambda_\mathrm{G} = L_\mathrm{B}$, in the beginning of this chapter.

Although this reduced resonance condition looks strikingly simple it does cover some surprises. The resonance wavelength looks as if it is linear in the grating period with the proportionality constant $n_\mathrm{co} - n_\mathrm{cl}$. However, this is *not* the case. The difference in effective indices, $n_\mathrm{co} - n_\mathrm{cl}$, depends strongly on the wavelength. In fact, it can shown for a PCF a Taylor expansion in the resonance wavelength around $\lambda_\mathrm{r} = 0$, the zero and first order coefficients are zero, since both indices converge to the base material index in the short wavelength limit [90]. Thus to lowest order the resonance wavelength is *inversely* proportional to the grating period.

4.1.1 Analytical solution of CMT equations

It is possible to obtain analytical solutions to the mode amplitudes. By changing the phase of the amplitudes,

$$\tilde{a}_m(z) = \hat{a}_m(z)e^{i\delta z/2} = e^{i(\sigma_m+\delta/2)z}a_m(z)/\sqrt{\beta_m}, \tag{4.13}$$

the matrix in the coupled mode equations (Eq. (4.7)) is constant in z. The matrix is Hermitian and its determinant is non-zero. The eigenvalue method for linear coupled differential equations may be used. The initial values for differential equations are $\tilde{a}_\mathrm{co}(0) = 1, \tilde{a}_\mathrm{cl}(0) = 0$. The particular solution is

$$\tilde{a}_\mathrm{co}(z) = \cos\left(\sqrt{|\kappa|^2 + \delta^2/4}\,z\right) + i\frac{\delta/2}{\sqrt{|\kappa|^2 + \delta^2/4}}\sin\left(\sqrt{|\kappa|^2 + \delta^2/4}\,z\right). \tag{4.14}$$

---

[1]This is not true for most polymer gratings, where the grating can be erased by temperature [89]. But for silica gratings under $100°C$ this is true.

We see that the core transmission is given by

$$T_{\text{co}}(z) = \frac{|a_{\text{co}}(z)|^2}{|a_{\text{co}}(z=0)|^2} = 1 - \frac{4|\kappa|^2}{4|\kappa|^2 + \delta^2} \sin^2(\frac{1}{2}\sqrt{4|\kappa|^2 + \delta^2}z). \quad (4.15)$$

The equation above is plotted as function of the detuning for different lengths in Fig. 4.1 and as function of z for different values of the detuning in Fig. 4.2. The corresponding value for $|\tilde{a}_{\text{cl}}|$ can be found using norm conservation $|\tilde{a}_{\text{co}}|^2 + |\tilde{a}_{\text{cl}}|^2 = 1$. At resonance the core transmission simplifies to

$$T_{\text{co}}(z, \delta = 0) = \frac{1}{2} + \frac{1}{2}\cos(2|\kappa|z). \quad (4.16)$$

The power in an infinite long LPG oscillates between the core and the cladding mode. The first total mode conversion, $a_{\text{co}} = 0$, occurs at $z = \pi/(2|\kappa|)$. Inserting this length in Eq. (4.15) gives

$$T_{\text{co}}\left(\frac{\pi}{2|\kappa|}, \delta\right) = 1 - \frac{\pi^2}{4}\text{sinc}^2\left(\frac{\pi}{2}\sqrt{1 + \frac{\delta^2}{4|\kappa|^2}}\right), \quad (4.17)$$

where the sinc function is $\text{sinc}(x) \equiv \frac{\sin(x)}{x}$. The resulting spectrum is seen in Fig. 4.2.

4.1.2 Analyzing long-period grating spectra

Since this project also involves inscription of long-period gratings, we must be able to identify the characteristics of the LPG spectrum. The inscription of the grating is experimentally monitored in situ. During the inscription $|\kappa|L$ is increased either by the number of periods or by the magnitude of the perturbation. Since the attenuation at resonance is sinusoidal in the grating strength, $|\kappa|L$, according to Eq. (4.16) it is important to stop the inscription, at the maximum attenuation, $|\kappa|L = \pi/2$. In figure 4.1 we have shown four spectra for different grating length, L, but with a constant coupling constant, κ. It is seen that the size of the dip increases with the length, and the formation of the dips is initially slow in the number of periods. At $L = \pi/(8|\kappa|)$ (Fig. 4.1 top right) the attenuation of the LPGs is difficult to detect since the noise in the spectrum analyze is usually larger. At the grating length $L = \pi/|\kappa|$ the incident mode power at resonance has returned to the core mode and two sidelobes appear around the resonance. When analyzing Eq. (4.15) the expression contains two functions: a sinusoidal term and a prefactor that does not depend the grating length, but on the coupling strength, κ, and the detuning, δ. In Figure 4.2 we displayed a

grating spectrum with full attenuation at the resonance wavelength, $\kappa L = \pi/2$. There is also added a dotted line that shows Eq. (4.15) without the sinus factor. Clearly, the maximum attenuation is limited by the fraction in Eq. (4.15), while the position and depth of the resonance peak and side-lobes are controlled by the sinus factor. We have also plotted the evolution of the transmission at resonance, in the sidelobes, and in middle between the sidelobes. The sidelobes corresponds to oscillations along the z-axis. For higher the absolute values of the detuning, the oscillation becomes faster. We thus expect that the sidelobes closest to resonance are the most robust in experiment, while the higher order sidelobes more easily vanish.
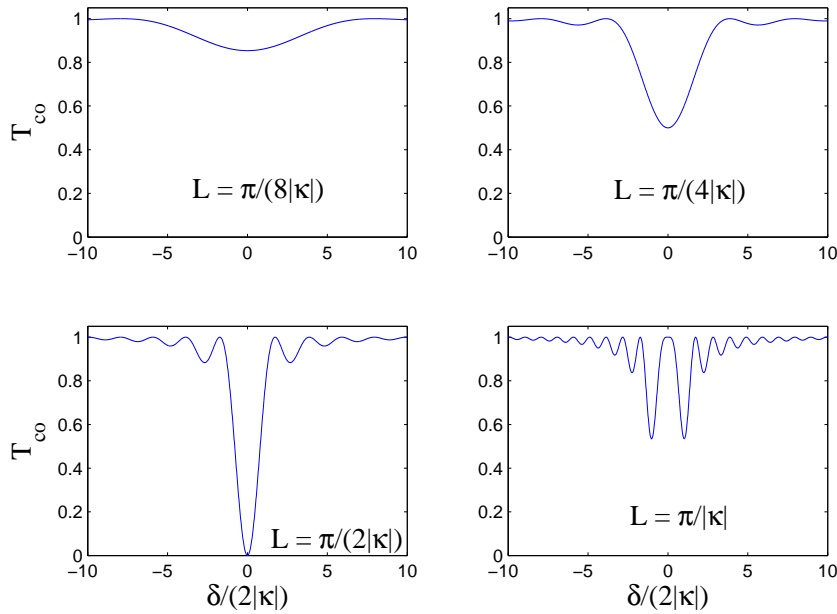
Figure 4.1: The resulting spectra of CMT's Eq. (4.15) for increasing grating length. At resonance ($\delta = 0$) the core mode power is transferred into the cladding mode at $L = \frac{\pi}{2|\kappa|}$ (bottom left). At the double length the mode power has returned to the core mode (bottom right).
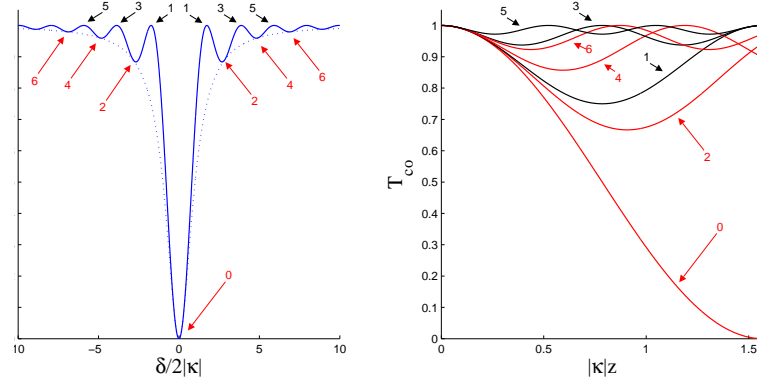
Figure 4.2: Left: The transmission at $L = \pi/(2|\kappa|)$. The dotted line is Eq. (4.17) without the sinus function. Characteristic detunings are marked with numbers and plotted in the right figure. The core mode amplitude as function of length (right) for different characteristic detunings. The oscillations of resonance dip and sidelobes are clearly seen.

4.1.3   Full-width half maximum

With CMT the transmission is considered as function of the detuning, δ. However, experimentally, the transmission is measured as function of wavelength. The full-width half maximum (FWHM) of the dip measured in the wavelength turns out to be dependent on the waveguide dispersion. This is even though the δ_{FWHM} of the wavevector and detuning is not dependent on dispersion.

To find a relation between δ_{FWHM} and λ_{FWHM} let us first consider a transmission spectrum as function of the detuning and the wavelength. For the detuning the FWHM can be found to be $\delta_{\text{FWHM}} = |\delta^+ - \delta^-|$, where $\delta^\pm$ are defined by $T(\delta^\pm) = \frac{1}{2}$. δ_{FWHM} will be shown to be a function of the grating length, L, and coupling constant, κ, and it is unaffected by the waveguide dispersion. For the wavelength we have equivalently, $T(\lambda_{\text{r}} + \Delta\lambda^\pm) = \frac{1}{2}$. The detuning, $\delta(\lambda) = \beta_{\text{co}}(\lambda) - \beta_{\text{cl}}(\lambda) - \frac{2\pi}{\Lambda_{\text{G}}}$, is expanded around

the resonance wavelength, λ_r, to first order

$$
\begin{aligned}
\delta(\lambda_r + \Delta\lambda) &= \beta_{co}(\lambda_r + \Delta\lambda) - \beta_{cl}(\lambda_r + \Delta\lambda) - \frac{2\pi}{\Lambda_G} \\
&\simeq \frac{\partial(\beta_{co} - \beta_{cl})}{\partial k} \frac{\partial k}{\partial \lambda}\bigg|_{\lambda_r} \Delta\lambda \\
&= -(n_{g,co} - n_{g,cl}) \frac{2\pi}{\lambda_r^2} \Delta\lambda.
\end{aligned}
\tag{4.18}
$$

Substituting $\delta(\lambda_r + \Delta\lambda) = \delta_{FWHM}/2$ and $\Delta\lambda = \lambda_{FWHM}/2$ we obtain the expression

$$
\frac{\lambda_{FWHM}}{\lambda_r} = \frac{\lambda_r}{2\pi} \frac{\delta_{FWHM}}{|n_{g,co}(\lambda_r) - n_{g,cl}(\lambda_r)|},
\tag{4.19}
$$

which incorporates the dispersion of the effective indices in a consistent manner.

The constant δ_{FWHM} can be found by Eq. (4.17). Ignoring the wavelength dependence of the coupling constant, $\kappa = \kappa(\lambda_r) = \pi/(2L)$, we solve $T(\delta^\pm L/\pi) = 0.5$ for Eq. (4.17) numerically. This yields $\delta^+ = -\delta^- \simeq 0.80\frac{\pi}{L}$. Inserting in Eq. (4.19) yields

$$
\frac{\lambda_{FWHM}}{\lambda_r} \simeq 0.80 \frac{1}{|n_{g,co}(\lambda_r) - n_{g,cl}(\lambda_r)|} \frac{\lambda_r}{L}.
\tag{4.20}
$$

This expression was originally derived by Vengsarkar *et al.* [91] in 1996 and later corrected by Shu *et al.* [92] in 2002. λ_{FWHM} is obviously large close to group index match, $n_{g,co}(\lambda_r) - n_{g,cl}(\lambda_r) = 0$. We note that the derived expressions are not valid at group index matching between the two resonant modes, $n_{g,co}(\lambda_r) - n_{g,cl}(\lambda_r) = 0$. In Chap. 5 it will be shown that a fiber sensor does not have a linear response to the measurand, and there is no need to expand the theory to also included waveguides with near group index matching.

4.2   Simulation of spectra

For the simulation of spectra we wish to incorporate losses of the modes, in particular the cladding modes, as these will be shown to affect the spectrum.

The analytical CMT of Sec. 4.1 is derived under the assumption of lossless modes and thus the expression do not apply. Although, CMT can be used to solve the problem numerically, including losses, the Green's function method (GFM) is numerical more robust and powerful. Although the

GFM could sound highly advanced, the method is essentially quite similar to CMT, and should correctly be considered a variation of CMT. The GFM does not provide the simple analytical solutions as CMT does, but GFM only uses the mode expansion also used in CMT, and does not use the slowly varying envelope or the phase matching approximation. It does not require that the grating is uniform or even periodic. The numerical implementation is described in Ref. [2]. For lossless, weak ($|\kappa|\Lambda_{\mathrm{G}} \ll 1$) uniform LPGs the GFM and the CMT agree by virtue of the approximations of CMT.

In brief, the method is a perturbative solution to Eq. 4.3 with a general dielectric perturbation, $\Delta\varepsilon(\mathbf{r}_\perp, z)$ rather than a Fourier expansion, by the Lippman-Schwinger equation

$$E_m(z) = E_m^{(0)}(z) - \sum_n^{\mathrm{modes}} \int_0^z \mathrm{d}z' i G_{mm}^{(0)}(z,z') \Delta\varepsilon_{mn}(z') E_n(\mathbf{r}_\perp, z'), \quad (4.21)$$

where $E_m(z)\mathbf{E}(\mathbf{r}_\perp) = \mathbf{E}(\mathbf{r}_\perp, z)$, and $G_{mm}^{(0)}(z,z')$ is the unperturbed Green's function propagator with the property $E_m^{(0)}(\mathbf{r}_\perp, z') = 2\beta_m i G_{mm}^{(0)}(z',z) E_m^{(0)}(\mathbf{r}_\perp, z)$, where the appearance of the propagation constant β_m originates from the normalization of the zero order Green's function. The zero order Green's function simply propagates the electric field along the axis. The Lippman-Scwinger Eq. (4.21) is an integral equation requiring that the solution to $E_m(z)$ is integrable but not necessarily differentiable as with CMT. This makes the numerical solution extremely robust. For example, a discretization with 2 grid points per grating period resolution yields an error in the transmission coefficient typically which is $< 10^{-4}$. In the paper Ref. [2] the so-called Dyson's equation is used, but this equation is equivalent to the Lippman-Schwinger equation. The general Green's function formalism is well known from electromagnetic scattering theory for use with e.g. antennas [74].

4.3   Numerical simulations

The cladding modes are lossy and typically attenuate over some centimeters. Given that the attenuation is weak over the length of a wavelength, the attenuation is proportional to $\exp(-\alpha z)$ as described in Sec. 3.1.1. It has been shown by Daxhelet and Kulishov [93] that the LPG is sensitive to cladding modes losses. The loss weakens the destructive interference by the core and cladding modes. The attenuation at resonances can still be made

complete, but the grating length must be longer. The losses of the cladding mode also smear out the sidelobes in the spectrum, such that the shape of the resonance dip approaches the smooth spectrum shown on the right in Fig. 4.2 (dotted line). The broadening will make the resonance wavelength difficult to estimate. To give a quantitative estimate of the effects of the attenuation, consider an LPG in a LMA10 with 60 grating periods and the parameters, $\Lambda_G = 580\ \mu m, \lambda_r = 1\ \mu m$. Given these parameters, then solving for the transmission spectrum for $\alpha L = 0, 4\pi, 20\pi, 80\pi$, which are plotted in Fig. 4.3. Clearly the sidelobes vanish and the resonance dip is weakend. It must be noted that the resonance dip can be increased, in spite of the losses, by increasing the length of the grating, although this only holds within reasonable cladding mode losses. To summarize, it is clear that any resonant cladding mode of PCF must satisfy two conditions:

1 Only well guided cladding modes with a low attenuation can be resonant (Fig. 4.3).

2 A resonant cladding mode *must* overlap with the core mode, as dictated by Eq. (4.9).
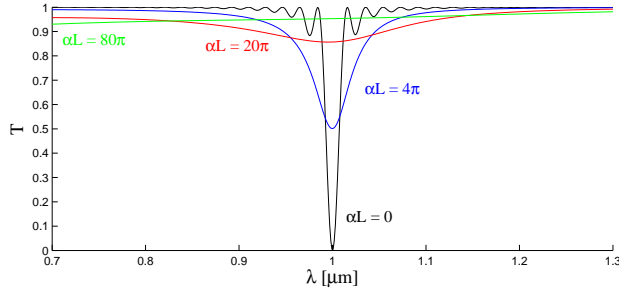
Figure 4.3: The effect of lossy cladding modes on the transmission spectrum. The coupling constant is $|\kappa| = \pi/(2L)$. The increasing attenuation constant, α, smooths out the side lobes and weakens the resonance dip.

4.3.1   Cladding modes: an open boundary problem

To obtain the field distributions and attenuation constants of the cladding modes a simulation using FEM is carried out. The total PCF cross section is simulated with a layer of air around, the PCF supports modes which

propagate in the core, the microstructured cladding, and the bulk silica surrounding the cladding. In Fig. 4.4 a number of representative modes
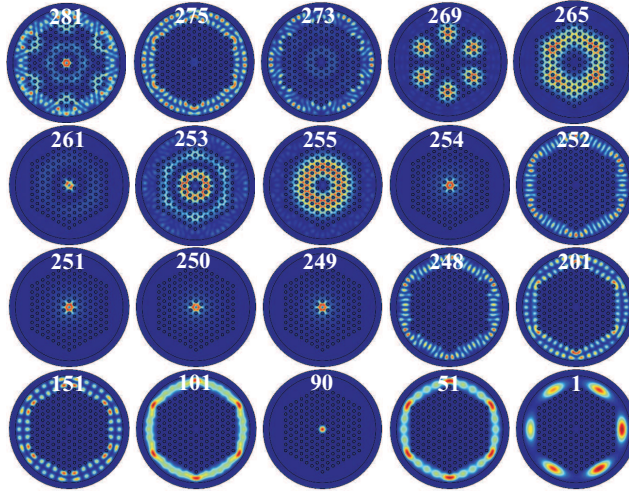
Figure 4.4: Eigenmodes in an LMA10 PCF at 1.0 μm wavelength. The core mode is the 90 lowest mode. The majority of modes are whispering galley modes in the bulk silica. The first cladding modes with overlap with the core are the modes 249-251 and 254, which are practically degenerate.

at the wavelength 1 μm are illustrated for an air filled LMA10 with seven rings of holes, $d/\Lambda = 0.45$, a pitch $\Lambda = 7.1\mu$m, and an outer diameter of 125 μm. The LMA10 is surrounded by 1Λ of air with metallic outer boundary conditions, $\mathbf{n} \times \mathbf{E} = \mathbf{0}$. The number in Fig. 4.4 represents the mode number, i.e. the number of modes minus one having a higher effective index than the current mode. The core mode has mode number 89-90, and the lowest cladding mode is number 249. A two fold degenerate mode is double counted. All but a few of the omitted modes are whispering gallery modes which are non-resonant. The modes tend to be confined to the core

and cladding or bulk material outside the microstructure. Although some
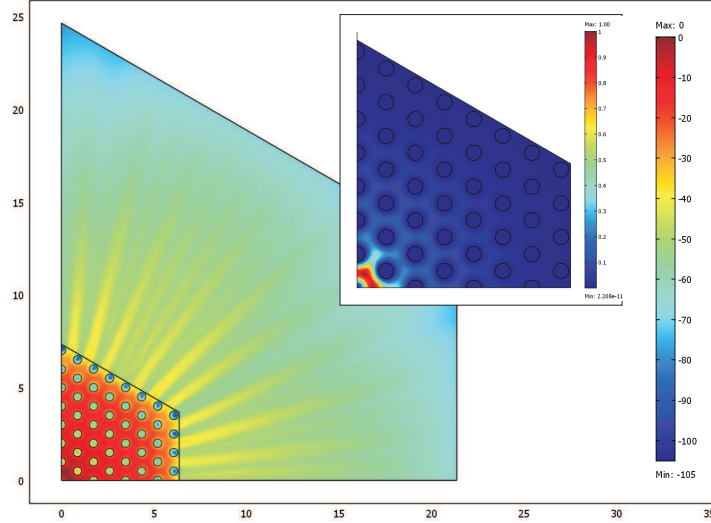
Figure 4.5: The z component of the Poynting vector of first cladding mode (4.17 bottom left) in dB. Inset: same as larger plot but in linear scale. The PML domain in the linear scale is not plotted.

hybridization of the modes in the microstructured cladding and bulk can be seen, this tends to decrease when the accuracy of the simulation is increased The accuracy of the effective indices in the simulation was $\sim 10^{-6}$ while the mode spacing in the bulk is $\sim 10^{-5}$. This does allow for some spurious mixing of the modes. At higher accuracies the cladding modes are still reflected at the outer boundary. In practice, the bulk modes are so closely spaced, that imperfections and bending easily hybridize the modes. Thus the bulk modes form a quasi-continuum. If a cladding mode is scattered into the bulk it is reasonable to assume that the back-scattering from the bulk into the cladding is negligible. The bulk can then be replaced with an open boundary where any incident wave is not reflected. One approach is to use perfectly matched layers (PMLs) introduced in Chap. 3 [74]. For the weakly guided cladding modes a 15Λ thick PML is required in order to converge the attenuation constants (Fig. 4.5).

In conclusion, we may modify the computational domain for the PCF cross section by removing the bulk silica outside the microstructure and replacing it with a PML. This eliminates almost all non-resonant bulk modes. In Fig. 4.5 the lowest cladding mode at $\lambda = 1$ μm is shown to give an

Figure 4.6: The attenuation constants (left) and effective indices (right) of all modes relative to the fundamental core mode, for an air filled LMA10 fiber. See text for details. The attenuation constant for the core mode is zero and not included. The labels refer to the outer boundary conditions on the domain (Fig. 3.5) along the x and y axis.

idea of how the open boundary emulation effects the mode profile. To further narrow down the number of possible resonant modes, the six lowest eigenmodes are found for each of the four possible symmetry configurations shown in Fig. 3.3. The resulting solutions are shown in Figs. 4.17-4.20 for the wavelength $\lambda = 635$ nm. The modes may be inspected experimentally be fabricating a PCF-LPG with resonance at 635 nm, cut the PCF immediately after the LPG and connecting it to a 635 nm laser (Fig. 4.8). The PCF-LPG had an attenuation of 20 dB at resonance. It may seem surprising that apparently, a lot of mode power is still in the core of the LMA10, but as seen in Fig. 4.17 and 4.20, the power flow of the resonant cladding modes is highest in the core. The core mode is readily identified as the fundamental mode in Figs. 4.18 ($\mathbf{n} \times \mathbf{E} = \mathbf{0}$ at x-axis, $\mathbf{n} \times \mathbf{H} = \mathbf{0}$ at y-axis) and 4.19 ($\mathbf{n} \times \mathbf{H} = \mathbf{0}$ at x-axis, $\mathbf{n} \times \mathbf{E} = \mathbf{0}$ at y-axis). None of the higher order modes for these symmetries have any significant overlap with the core. In Figs. 4.17 and 4.20 the lowest four modes have a significant overlap with the core. The modes in each figures seem be to degenerate to numerical accuracy, $\sim 10^{-6}$. Group theory dictates that they are non-degenerate. For our purposes they are both experimentally and numerically degenerate, since their spacing, $\Delta n_{\text{eff}} \sim 5 \times 10^{-7}$, is less than numerical accuracy with
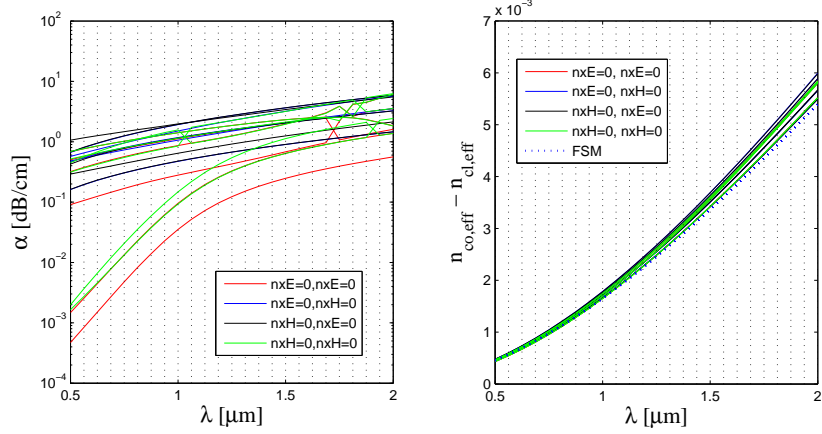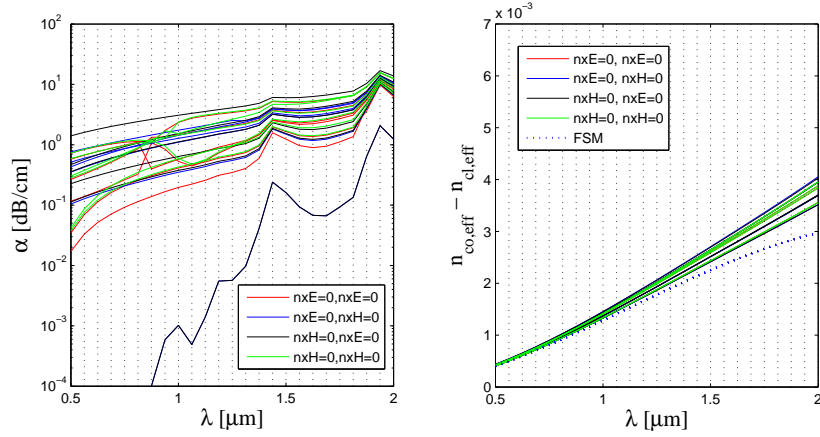
Figure 4.7: The attenuation constants (left) and effective indices (right) of all modes relative to the fundamental core mode, for a water filled LMA10 fiber. See text for details. The attenuation constant for the core modes (lowest black line) is seen approaching the loss of the cladding modes. The labels refer to the outer boundary conditions on the domain (Fig. 3.5) along the x and y axis.

a beat length of $L_B \sim 2$ m. The coupling constant Eq. (4.9) constitute an integral over the core and cladding mode and the perturbation. Since all the cladding modes indicated are *uneven* functions over the cross section of the PCF and the core mode is an *even* functions, the dielectric perturbation induced must also be either *uneven*, i.e. asymmetrical in the PCF cross section, or anisotropic.

The effective indices and the attenuation constants are calculated for all modes for a range of wavelengths. The results are displayed in Fig. 4.6 for an air filled LMA10 and in Fig. 4.7 for a water filled LMA10. Water absorbs in the visible and infrared area. The imaginary part of the refractive index of water is obtained from the data of Segelstein [94] while the real part is from the International Association for the Properties of Water and Steam (IAPWS) [95]. The effective indices are closely spaced. For the air filled LMA10 the difference of the core and cladding effective indices are very close to the difference of the effective indices of core and FSM mode. For estimates that do not requiring a calculation on a specific PCF structure the cladding modes indices may be taken to be equal that of the FSM ($n_{cl} \simeq n_{FSM}$), and the grating periods can easily be estimated in this way.
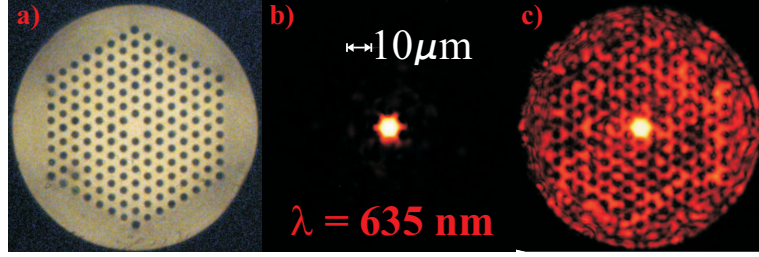
Figure 4.8: An LMA10 fiber (left). The core mode is seen in center. Right a PCF-LPG with resonance at 635 nm connected to a 635 nm laser. A strong intensity is seen in the core of the PCF.

For the water filled LMA10 (Fig. 4.7) the approximation $n_{cl} \simeq n_{FSM}$ is less accurate although, for practical purposes the accuracy may be sufficient.

The susceptibility to errors of the predicted resonance wavelength, at $\lambda_r = 1$ μm, in the numerical analysis is investigated. As the following results show,

$$\Lambda_{err} = \pm 1\% \sim \pm 70 \text{ nm} \quad \Rightarrow \quad \lambda_{r,err} = \pm 23 \text{ nm},$$
$$d_{err} = \pm 1\% \sim \pm 30 \text{ nm} \quad \Rightarrow \quad \lambda_{r,err} = \mp 38 \text{ nm},$$
$$d_{err}(\text{inner}) = \pm 1\% \sim \pm 30 \text{ nm} \quad \Rightarrow \quad \lambda_{r,err} = \pm 7.4 \text{ nm},$$
$$n_{r,err} = \pm 1\% \sim \pm 0.015 \quad \Rightarrow \quad \lambda_{r,err} = \pm 7.1 \text{ nm},$$

the predicted resonance wavelength is very sensitive to the physical parameters. This of course implies that accurate prediction of the resonance wavelength can be difficult. Conversely, it also implies that in experiment the resonance wavelength is also very sensitive to the PCF structure parameters, d, Λ.

4.4 CO$_2$-laser inscription method

In standard optical fibers the silica in the core contains dopants to increase the refractive index. The refractive index of the doped silica is sensitive to UV radiation and this may be used for inscription of gratings. Pure silica PCFs do not have a UV-sensitive core. A natural solution is to include a UV sensitive core in the PCF [96, 34, 97] but this requires drawing a special PCF, which is expensive. For LPGs the inscription can also be done using an electric arc [98] [99, 100] or a CO$_2$ laser [101, 102] to treat the PCF with point-wise, intense heating.
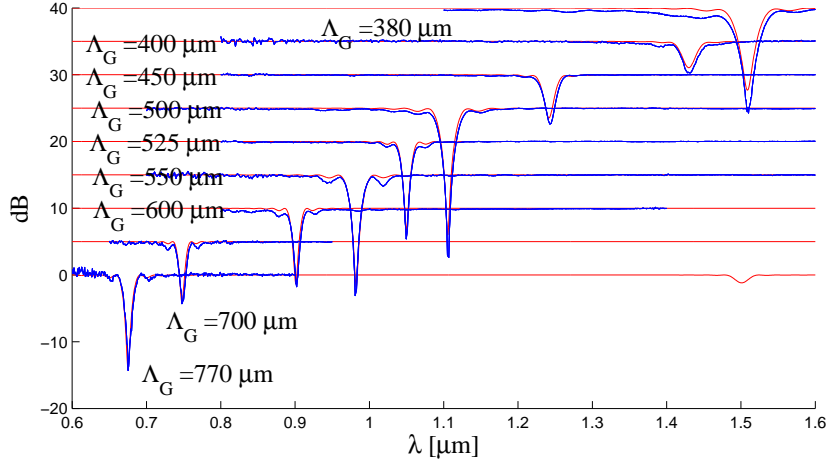
Figure 4.9: LPG spectra for different grating periods, Λ_G. The number of grating periods are (increasing λ_r) 40, 60, 60, 40, 60, 40, 60, 60, and 40. The blue lines indicate experimental data, the red lines are simulations with the GFM. λ_r and $|\kappa|$ has been fitted to the experimental data. The spectra are offset 5 dB for clarity.

The first demonstrated CO_2 laser written LPG by Kakarantzas *et al.* [101] where the holes of the PCF were collapsed in the points of heating. They concluded that the inscription was due to the collapse. This explanation is intuitive and easy to comprehend and it has since then become a common misconception. Hole collapse can occur as side effect of the heat treatment, but it is not instrumental. The collapse is neither necessary nor desirable if the liquids is to be infiltrated into the holes. Collapse has also been rejected by several authors [103, 104, 105]. The coupling constant (Eq. (4.9)) for complete hole collapse yields that its value is orders of magnitude too small for an effective mode coupling in the LPG. Hole collapse is a drastic perturbation to the PCF, but the field intensity inside the holes of the core and cladding modes is very small, implying small coupling constants. In experiments the hole collapse is often accompanied by a general loss in transmission for all wavelengths by a couple of dBs. As we will see, the fabricated LPGs have zero insertion loss.

The CO_2-laser setup was improved two times during the project. We will review each of the three setups to reveal their advantages, short-comings and lessons learned.
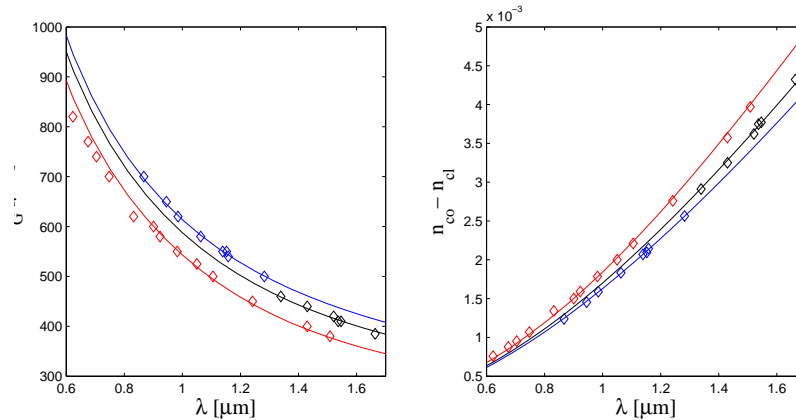
Figure 4.10: Resonance plot for the LMA10. Three pieces are presented blue, black, and red. The red is fitted with a numerical data with a hole diameter $d/\Lambda = 0.4778$, blue $d/\Lambda = 0.4472$, black $d/\Lambda = 0.4576$.

First version

The setup uses a Synrad Fenix CO$_2$ laser with a maximum output power of 75 W. The laser has a built-in controllable mirror, which enables us to control the movement of the laser beam very precisely with the computer program WinMark. The power of the laser can be varied in steps of one percent. The CO$_2$ laser is originally intended for marking of various objects and tasks such as the micromachining described in Chap. 2. The laser has a wavelength in the infrared of 10.6 μm at which silica is completely opaque. Originally the computer controlled built-in mirror was used for the inscription. The PCF was fixed in a stage where it was kept straight by two clamps secured with small screws. A WinMark program was made which simply wrote a number of grating lines on the PCF. The energy absorbed in each grating period was varied by changing the velocity of the laser beam ($\sim$3 mm/s) while keeping the laser power fixed. The velocity was calibrated by choosing a high velocity and then decreasing it gradually until an LPG resonance dip appear in the transmission spectrum.

The setup and procedure was acceptable for writing gratings with a few periods (< 15). It succeeded only to inscribe LPGs a few times. The LPGs had high insertion losses of 2-3 dB, and the inscription was difficult to reproduce. The problem was identified to originate from the use of the built-in mirror of the laser. The focal length of the laser is 70 mm. If the grating
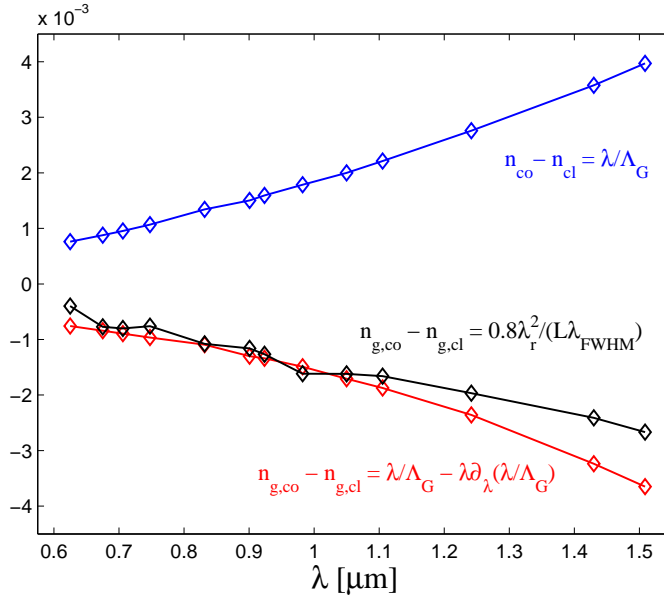
Figure 4.11: Experimental data: the difference in effective indices of the core and cladding mode, λ_r/Λ_G, (blue). The group index mismatch calculated from the effective indices (red) and from the FWHM of the spectra (black).

length is, say 30 mm, then PCF will not remain in the focal point of the laser throughout the grating leading to variation in the intensity. To remedy the problem of the mirror of the CO_2 laser a new setup was constructed.

Second version

In the second version of the setup a single computer controlled linear stage was employed, which could be controlled using a Labview program. At the same time the PCF was fixed in a manual rotational stage, such that it could be exposed from all sides by rotation. In the other end the PCF was fixed on a wheel and kept straight by attaching a small weight on the PCF with tape. The CO_2 laser was then activated to write a single grating period, after which the PCF was translated a length of a period along its axis. This significantly increased the quality of the written gratings. The grating in Ref. [4] was fabricated in this setup. It turned out that exposing the PCF from different sides did not improve the quality of the grating. In practice the length of the inscribed gratings was limited to about 40 periods. The
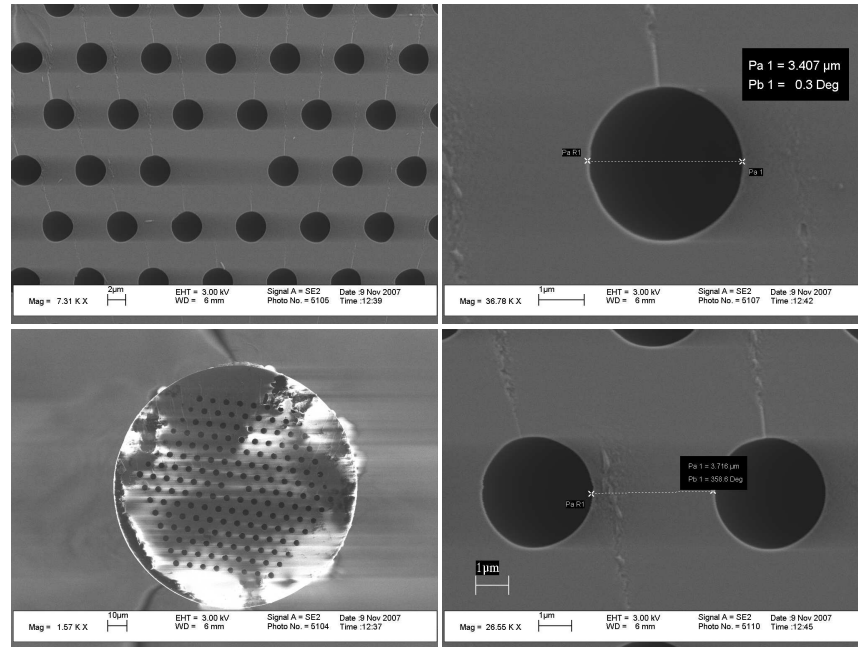
Figure 4.12: Scanning electron micrographs of the LMA10 used in this work. The structure can be seen to be very uniform. The hole diameter and pitch can be estimated from the micrographs. ($d/\Lambda = 0.4778$, $\Lambda = 7.123\,\mu\text{m}$)

reason for this was twofold. Firstly, inscription could be challenging on the patience of the operator, since for each grating period a button had to clicked on two different computers sequentially. With 40 periods and repetitions for several velocity settings, this setup was unnerving. More importantly, the power of the CO$_2$ laser decreases over time. After half an hour the inscription could be ineffective. The setup could reproducible gratings of good quality, although the success varied, in particular due to instability of the CO$_2$ laser. To improve the throughput, processing time, and quality of the LPGs the setup was further automatized.

Final version

In the third version of the setup a second linear stage was employed. This allowed to keep to the laser beam fixed and reduce time effects by a faster inscription. It also allowed the setup to be fully automated using a LabView program. The PCF was then passed through the laser beam in a meandering
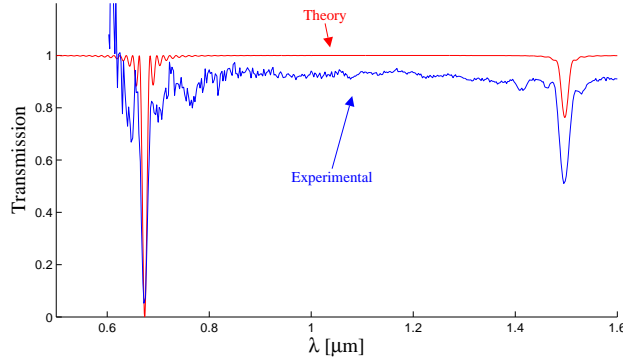
Figure 4.13: A second harmonic dip is seen in the spectrum for this $\Lambda_G = 770\,\mu$m LPG. The blue line is experimental data and the red simulations using the GFM. $n_{co} - n_{cl}$ has been fitted to a third order polynomial to resemble Fig. 4.10. The second order dip is lower since the coupling constant (Eq. (4.9)) decreases with wavelength. The magnitude and width of the second harmonic dip agrees well with experiment, indicating that the mode coupling integral in Eq. (4.9 ($= \kappa/k$) is constant.

pattern illustrated in Fig. 4.14. The PCF passes through the laser beam twice. The reason for this is practical. If a grating with an uneven number of periods is inscribed then the PCF is on the wrong side of the laser beam and has to pass through the beam one more time in order to return to its initial position. The rotational stage and the wheel were retained. The PCF was only exposed on one side and the rotations ceased to be used.

In theory it is possible to start the laser, initiate the LabView program, and then go for coffee. In practice the operate can put his attention exclusively on monitoring the grating inscription progress on the spectrum analyzer. The inscription process takes about one second per grating period. Thus even long gratings of 100+ periods can be inscribed in a couple of minutes. Spectra of LPGs inscribed with this setup are seen in Fig. 4.9.

4.4.1 Experimental results

For the experiment we almost exclusively used the LMA10 [52] large mode area photonic crystal fiber, with the structural parameters pitch $\Lambda \simeq 7.12$ μm, hole diameter, $d/\Lambda \simeq 0.478$. The parameters vary from batch to batch, and may even vary in a PCF from a single drawing. The effect mode field
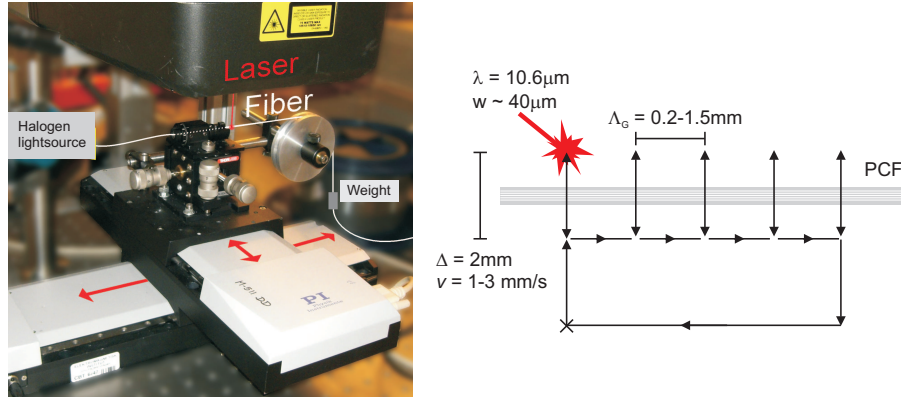
Figure 4.14: CO$_2$ laser inscription setup

Figure 4.15: A photo of the CO$_2$ laser inscription setup left. Right: the movements of the stages seen from above. Photo and graphics (left) reproduced with permission [106].

diameter is $2\Lambda - d \sim 10\,\mu$m. The pieces of LMA10 PCF had slightly different structural parameters, since they probably originated from different drawings. In the initial grating inscription we used both a 5 and 7 ring LMA10. But later we received a large quantity (100 m) of a LMA10 which was very homogeneous in its structure. Scanning electron microscope pictures of this PCF is seen in Fig. 4.12. The LMA10 was chosen since it was easy to work with. Furthermore, its large core makes it easy to couple light into the fiber. Secondly, in practice the setup can not inscribed LPGs with periods less than the PCF outer diameter, $\Lambda_G > 125\,\mu$m. This limits the choice of resonance wavelength, λ_r. For the LMA10 the resonance wavelength can be chosen freely from 400 nm ($\Lambda_G \sim 1.5$ mm) to 1700 nm ($\Lambda_G \sim 0.3$ mm).

A series of scanning electron microscope micrographs are seen in Fig. 4.12. The structural parameters for this specific LMA10 can be estimated to $d = 3.407 \pm 0.03\mu$m $= (0.4778 \pm 0.005)\Lambda$ and $\Lambda = 7.123 \pm 0.03\,\mu$m.

To estimate the PCF structure parameters, Λ, d, from the resonance plots in Fig. 4.10 some numerical simulations were done. It proved difficult to fit both the pitch and the hole diameter to the difference in effective indices, $n_{co} - n_{cl}$, using a least squares method. The partial derivatives of $n_{co} - n_{cl}$ with respect to the hole diameter and pitch proved to be too similar numerically. In mathematical terms this is called badly conditioned. It was chosen

to fix the pitch, $\Lambda = 7.1\,\mu$m, and estimate the hole diameter, since the pitch, Λ, can be determined experimentally with less relative uncertainty than the hole size. At the same time, $n_{\mathrm{co}} - n_{\mathrm{cl}}$, is less sensitive to an error in the pitch than to an error the hole diameter (as shown in Subsec. 4.3.1). The partial derivative $\frac{\partial(n_{\mathrm{co}} - n_{\mathrm{cl}})}{\partial d}$ was estimated by the difference in two simulations with the hole diameters $d/\Lambda = 0.45, 0.46$. The result for the hole diameters for the three different batches are $d/\Lambda = 0.4778$ (red data), $d/\Lambda = 0.4472$ (blue data), $d/\Lambda = 0.4576$ (black data), seen in Fig. 4.10. Comparing the fitted relative hole diameter (0.4778) for the first batch with the diameter obtained in the SEM (Fig. 4.12) for this PCF there is a striking correspondence until fourth decimal: $d/\Lambda = 0.4778$, although neither the numerical method nor the SEM can be expected to provide such high accuracy.

The data for $n_{\mathrm{co}} - n_{\mathrm{cl}}$ for the first batch (red) in Fig. 4.10 can be used to estimate the group index mismatch by Eq. (3.9). The curve is included in Fig. 4.11. Also included in the plot is the group index calculated with Eq. (4.20) from the experimental λ_{FWHM} obtain from the corresponding spectra in Fig. 4.9. The correspondence between the two group index mismatch curves is good, in particular when considering that the group index mismatch is quite sensitive to errors. This proneness to error will be discussed in more detail in Chap. 5.

A representative selection of LPG spectra have been plotted in Fig. 4.9. The grating spectra have been simulated, at each wavelength, with the GFM by choosing λ_{r}, $n_{\mathrm{co}} - n_{\mathrm{cl}} = \lambda_{\mathrm{r}}/\Lambda_{\mathrm{G}} \times (\lambda/\lambda_{\mathrm{r}})^2$ and $|\kappa|$ to fit the attenuation strength at resonance. GFM itself does not give predictions to the resonance wavelength. The attenuation constants given in Fig. 4.6 have been used The numerical spectra are seen to agree excellently with the experiments. The slight deviations of the sidelobes can be attributed to inhomogeneity, as the sidelobes have been shown to sensitive to unintentional apodization and chirp of the LPG in Fig. 4.2.

4.4.2   Heat transfer simulations

The exact mechanisms behind inscription and the refractive changes in the PCF are at present unknown to the best of the author's knowledge. Zhu *et al.* [103] have proposed that the change is caused by a stress-optical effect, and that the inscription is due to stress from the drawing released by the heating. Morishita and Miyake [105] have proposed the inscription is due to glass structure related to the heating and the rate of the subsequent rapid cooling. Pure silica glass has a melting point of $1650°$C after which it becomes a viscous liquid with a boiling point of $2230°$C. To investigate the

heating and cooling of the PCF a FEM simulation was carried out using the heat transfer module of COMSOL Multiphysics [71]. To best of the author's knowledge, this is the first time that the stated problem is addressed with any numerical method.

The cross section of an LMA10 has to be described by a minimum $\sim$ 10.000 finite elements. If the resolution along the fiber axis is, say, one element per 20 micron, and if the simulated piece of PCF is 5 mm, then $250 \times 10.000 = 2.500.000$ elements are needed. There is a mirror symmetry, $z \rightarrow -z$, around the plane in which CO$_2$ laser beam moves. This reduces the size of the problem by a factor of two. 1.250.000 elements is not intractable for a FEM simulation, but very powerful computers are needed. Instead, it is possible to make an approximate solution to the problem. For LMA10 the air filling fraction is $\sim$ 18%, and most of the cross section consists of silica. The air holes may then be neglected. The approximation can seem drastic at first sight, but is nevertheless good. For an LMA10 the error for approximating the PCF to be made of homogeneous silica is within 2 %. At the outer boundary the heat conduction from the air is quite low, and at high temperatures the heat loss is dominated by radiation losses described by the Stefan-Boltzman law, $\sigma_B T^4$. The simulated PCF is 5 mm long. The simulation solves the time dependent problem where a laser beam, $40 \, \mu$m in diameter passes over the PCF from above. Silica is completely opaque at this wavelength, so the energy is transferred to the outer surface of the PCF. Snapshots of the temperature distribution in the PCF are shown in Fig. 4.16 for the parameters $V = 3 \, \text{mm/s}$, and $P = 0.2 \, \text{W}$. The temperature gradients are seen to very large ($\sim 3500 \, ^\circ$C). The temperature gradients in PCF induced by the laser beam are asymmetrical, because the intensity is highest close to the point of incidence of the laser. This could agree with an asymmetrical dielectric perturbation of the LPG. This numerical evidence supports the conclusions of cladding mode analysis (Subsec. 4.3.1), where the dielectric perturbation was also found to be asymmetrical.

Although the temperature is locally above the boiling point of silica ($2230 \, ^\circ$C) at the laser beam point, this only very locally. The model assumes that the heat conductivity and heat capacitance of silica is constant, and this may be unphysical. On the left in Fig. 4.16 the maximum temperature in the core center and on the surface are shown as contour plots. The relevant parameters window in the contour plot constitute a small area if it is assumed that maximum surface temperature is below the boiling point, and the maximum core temperature is above the melting point. The parameters in the contour plot may be helpful for determining the relevant settings for the experimental setup. We note that the 2.25 W indicated on the Synrad

laser which is used in the LPG inscription is probably on a tenth, ~ 0.2 W in practice, since 2.25 W would melt the PCF.
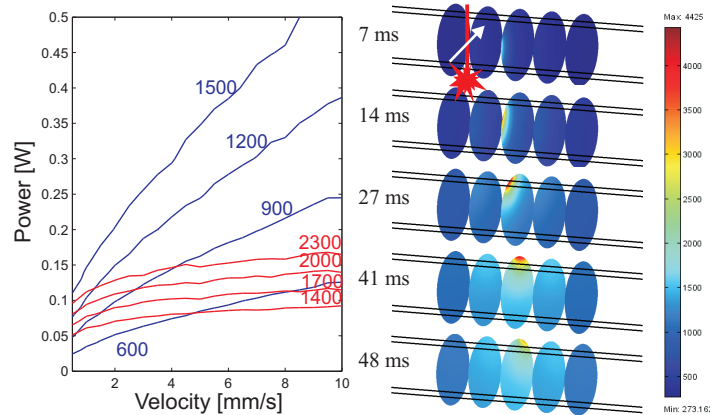
Figure 4.16: Left: the contour lines for the maximum core temperature (blue) and the maximum surface temperature (red) during the LPG inscription. Right: temperature distributions at different times, since the first contact of the PCF and the laser beam. Large asymmetrical temperature gradients are seen, as well as a localized heating of the PCF.

4.5   Summary

An efficient procedure for calculating the resonant cladding modes has been presented. A highly automated setup for writing LPGs with an unprecedented high number of grating periods, throughput, and quality have been presented. The experimental setup is new and has been invented and built in the project. The experimental data agree well with numerical data for resonant wavelengths from 500 to 1700 nm. The effects and origins of lossy cladding modes are discussed. From a combined cladding mode analysis and CMT, it is argued that resonant cladding modes must have an overlap as well as being well guided. By symmetry of the resonant cladding modes the index perturbation induced by the CO_2-laser must be asymmetrical in the PCF cross section. The findings are supported by FEM heat transfer simulations. This is the first time CMT and PCF cladding mode analysis are combined in a numerical study.
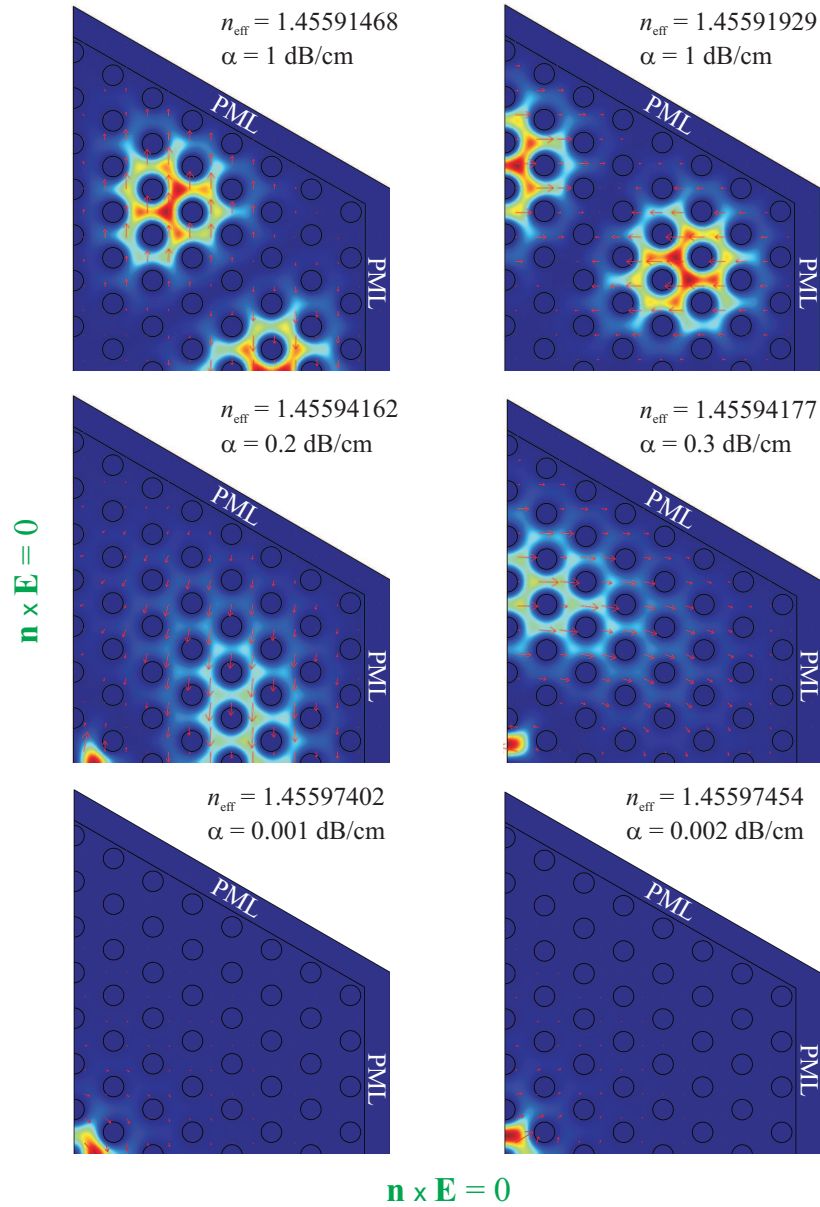
Figure 4.17: The six modes with highest effective index with perfect electric conductor boundary conditions along the x and y-axis. The color indicates the z-component of the Poynting vector, (red high, blue zero). The vectors indicate the direction of the electric field. The center and bottom modes are resonant modes, since they overlap with the core.
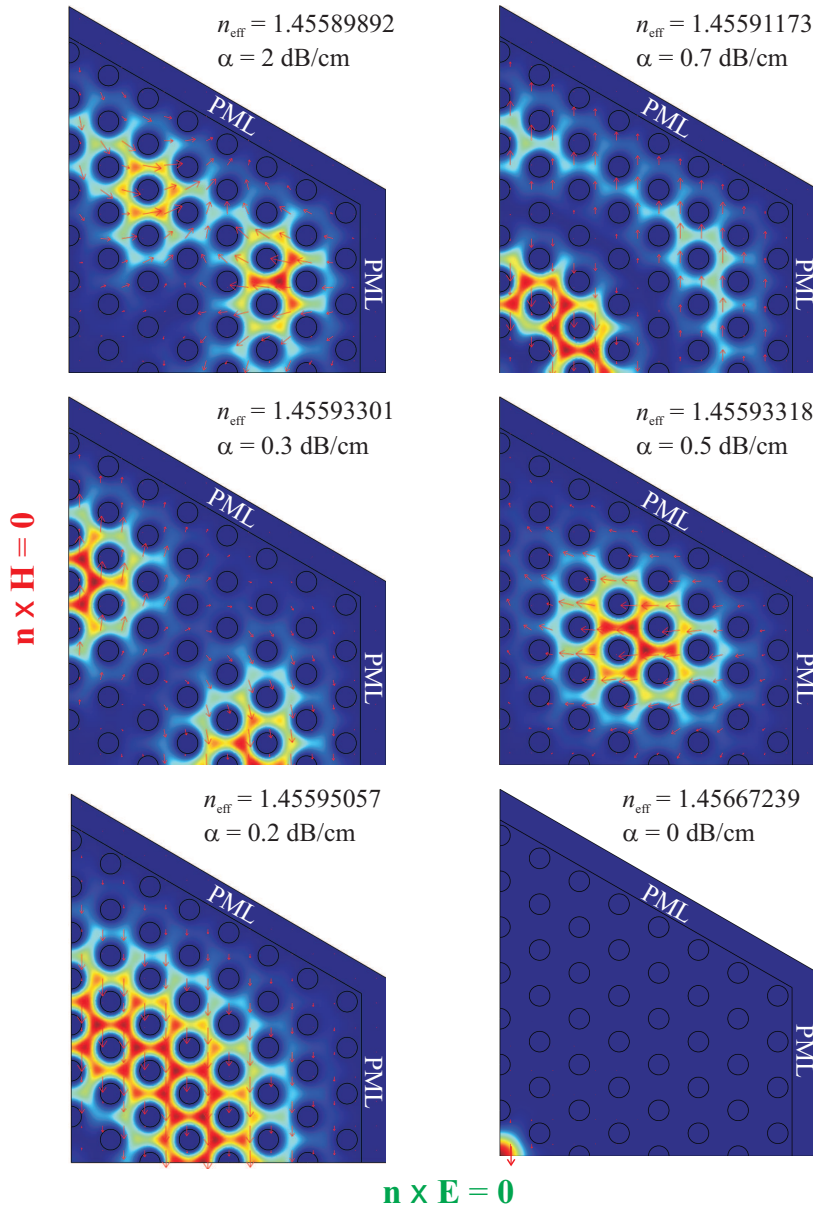
Figure 4.18: The six modes with highest effective index with the boundary conditions: perfect electric conductor along the x-axis and perfect magnetic conductor y-axis. The color indicate the z-component of the Poynting vector, (red high, blue zero). The vectors indicate the direction of the electric field. On the bottom right is the fundamental core mode. None of the other modes have a significant overlap with the core and are non-resonant.
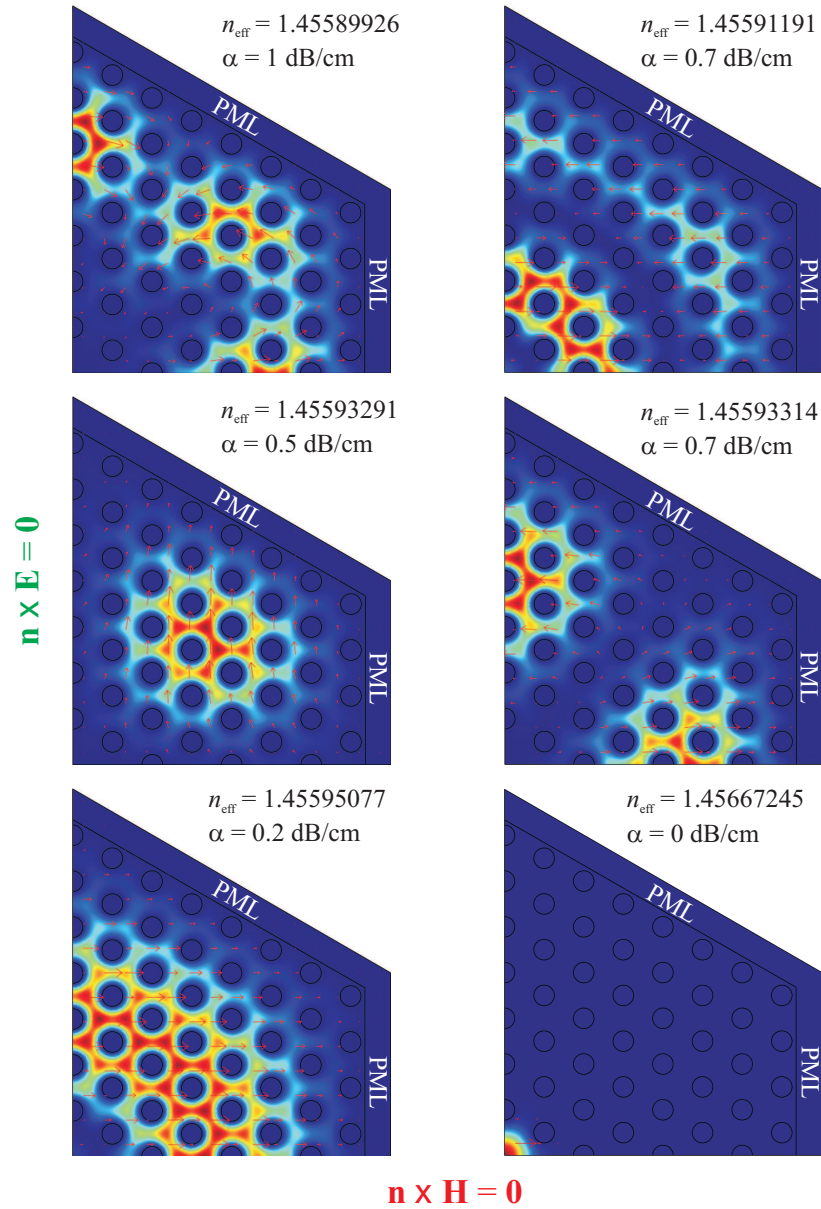
Figure 4.19: The six modes with highest effective index with the boundary conditions: perfect magnetic conductor along the x-axis and perfect electric conductor y-axis. The color indicate the z-component of the Poynting vector, (red high, blue zero). The vectors indicate the direction of the electric field. On the bottom right is the fundamental core mode. None of the other modes have a significant overlap with the core and are non-resonant.
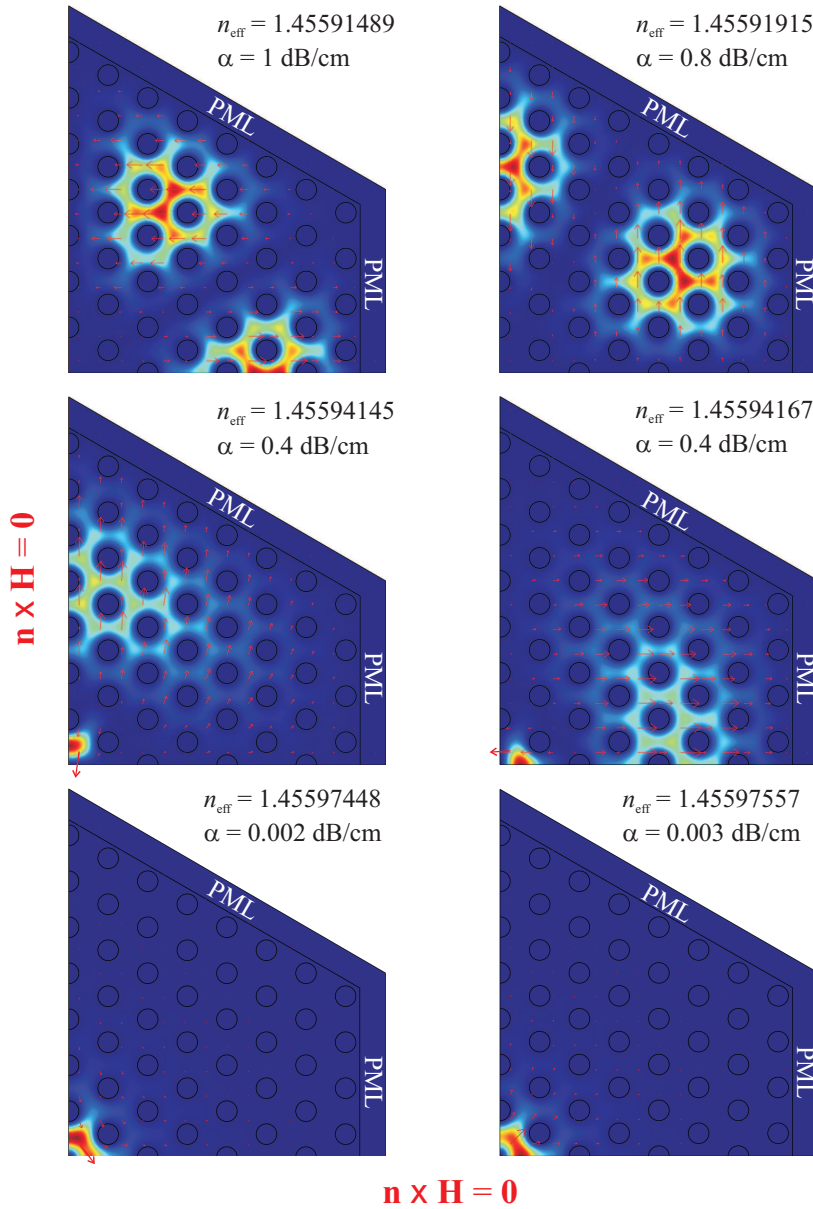
Figure 4.20: The six modes with highest effective index with perfect magnetic conductor boundary conditions along the x and y-axis. The color indicate the z-component of the Poynting vector, (red high, blue zero). The vectors indicate the direction of the electric field. The center and bottom modes are resonant modes, since they overlap with the core.

Chapter 5

Fiber grating sensors

5.1 Linear response theory

The fiber grating sensor is perturbed by a measurand to produce a change in the measured quantity, in our case the resonant wavelength. The measurand can be temperature, strain, refractive index sensing, or biosensing. At the present point it is not necessary to specify the application. For quantitative and qualitative estimation of the measurand a linear relation to the resonant wavelength is wanted. Since the resonant wavelength shifts are generally small compared to the wavelength, it is natural to employ perturbation theory. To reduce the complexity of the expressions we define

$$\bar{n}_{\text{eff}}(\lambda_{\text{r}}) \equiv n_{\text{co}}(\lambda_{\text{r}}) - n_{\text{cl}}(\lambda_{\text{r}}), \quad \bar{n}_{\text{g}}(\lambda_{\text{r}}) = n_{\text{g,co}}(\lambda_{\text{r}}) - n_{\text{g,cl}}(\lambda_{\text{r}}) \tag{5.1}$$

transforming the resonance condition of an LPG Eq. (4.12) to the more compact expression

$$\lambda_{\text{r}} = \bar{n}_{\text{eff}}(\lambda_{\text{r}})\Lambda_{\text{G}}. \tag{5.2}$$

Consider a general measurand, α. Assume that the shift in resonant wavelength as well as in the measurand are sufficiently small, and the resonance condition Eq. (5.2) is expanded in the resonant wavelength and the measurand to first order

$$\lambda_{\text{r}} + \Delta\lambda_{\text{r}} = \left[\bar{n}_{\text{eff}}(\lambda_{\text{r}}, \alpha) + \frac{\partial \bar{n}_{\text{eff}}}{\partial \lambda_{\text{r}}}\Big|_{\lambda_{\text{r}},\alpha}\Delta\lambda_{\text{r}} + \frac{\partial \bar{n}_{\text{eff}}}{\partial \alpha}\Big|_{\lambda_{\text{r}},\alpha}\Delta\alpha\right]\Lambda_{\text{G}} \quad \Leftrightarrow$$

$$\left[1 + \frac{\partial \bar{n}_{\text{eff}}}{\partial \lambda_{\text{r}}}\Big|_{\lambda_{\text{r}},\alpha}\Lambda_{\text{G}}\right]\Delta\lambda_{\text{r}} = \Lambda_{\text{G}}\frac{\partial \bar{n}_{\text{eff}}}{\partial \alpha}\Big|_{\lambda_{\text{r}},\alpha}\Delta\alpha, \tag{5.3}$$

where the $|_{\lambda_{\text{r}},\alpha}$ indicates the the derivative is evaluated at λ_{r} and α Identifying the resonance condition $\Lambda_{\text{G}} \equiv \lambda_{\text{r}}/\bar{n}_{\text{eff}}(\lambda_{\text{r}})$ by Eq. (5.2) and $\bar{n}_{\text{g}} =$

$\bar{n}_{\text{eff}} - \lambda \frac{\mathrm{d}\bar{n}_{\text{eff}}}{\mathrm{d}\lambda}$, we obtain the expression

$$\Delta\lambda_{\text{r}} = \frac{\lambda_{\text{r}}}{\bar{n}_{\text{g}}} \frac{\partial\bar{n}_{\text{eff}}}{\partial\alpha}\bigg|_{\lambda_{\text{r}},\alpha} \Delta\alpha. \tag{5.4}$$

This allows us to define a measure of the sensitivity of the resonant wavelength relative to the measurand [6]

$$\begin{aligned}
\gamma_\alpha &\equiv& \left|\frac{1}{\lambda_{\text{r}}} \frac{\mathrm{d}\lambda_{\text{r}}}{\mathrm{d}\alpha}\right| \\
&=& \left|\frac{1}{\bar{n}_{\text{g}}(\lambda_{\text{r}})} \frac{\partial\bar{n}_{\text{eff}}}{\partial\alpha}\right| \\
&=& \frac{1}{|n_{\text{g,co}} - n_{\text{g,cl}}|}\left|\frac{\partial(n_{\text{co}} - n_{\text{cl}})}{\partial\alpha}\right|,
\end{aligned} \tag{5.5}$$

We have chosen the symbol 'γ_α' to match the notation of by Shu *et al.* [92]. Obviously, when γ_α is large the sensor will give large wavelength shifts, which will give a high sensitivity and accuracy of the measurand. With the high degree of freedom with PCFs of tayloring the dispersion properties, it is tempting optimize the sensitivity by designing a PCF with near group index matching between the core and cladding mode at the resonance. This line of thought has in fact been pursued by some researches [92, 107]. However, the FWHM of the resonance dips of LPGs gratings are typically 5-200 nm, which is much greater than the resolution of the optical spectrum analyzer (typically a few picometers). This means that the minimal detectable change in the measurand is limited not by the sensitivity and the resolution of the spectrum analyzer, but by the sensitivity relative to the FWHM. According to Eq. (4.20) the FWHM of the resonance dip is also affected by the group index matching. We therefore conclude that group index matching does not imply sensitive sensors. To ameliorate the deficiency, we propose a weighted sensitivity by the quality factor, Q, of the grating sensor as a measure of the sensor quality, which is the wavelength shift divided by the FWHM [6],

$$\begin{aligned}
Q_\alpha &\equiv& \frac{1}{\lambda_{\text{FWHM}}}\left|\frac{\mathrm{d}\lambda_{\text{r}}}{\mathrm{d}\alpha}\right| \\
&\simeq& 1.2\frac{L}{\lambda_{\text{r}}}\left|\frac{\partial(n_{\text{co}} - n_{\text{cl}})}{\partial\alpha}\right|.
\end{aligned} \tag{5.6}$$

We note that Q, in contrast to γ, does not increase spuriously when $\bar{n}_{\text{g}} \rightarrow 0$. Q thus allowing for consistent comparison of the different fiber grating sensors. It is clearly seen that the optimal sensor is characterized by a high

differential influence on the core and cladding index and possibly also, a long interaction length, L. In practice and numerically, the group index mismatch is extremely sensitive to the PCF structure parameters.

5.2   Refractive index sensing

Different approaches for for evanescent wave sensing with LPGs using evanescent wave sensing in various types of optical fibers have been demonstrated. Group index matched LPGs in standard optical fibers show a sensitivity of 2.7×10^{-4} by changing the magnitude of the resonance dip rather than the resonance wavelength [107]. Bragg gratings in standard optical fiber can be etched to reduce the size of the cladding. In this way the field fraction is enhanced to achieve a minimal refractive index change of $\sim 5 \times 10^{-4}$ at the refractive index 1.33 [108]. This has also been demonstrated using a special D-shaped fiber [109]. LPGs in standard optical fibers can also be coated with high index material to enhance sensitivity [110]. PCF-LPGs have been characterized to sensitivity to the external refractive index of the surroundings of the PCF-LPG by Dobb and co-workers. This was carried out with an electric arc inscribed PCF-LPG (five rings of holes) which showed a refractive index sensitivity of 80 nm/RI at a refractive index of water [111], $n_r = 1.33$.

Infiltrated PCF-LPGs can also be used to tune the resonance wavelength. Such shifts are particulary large for LPGs in photonic bandgap fibers as done by Steinvurzel *et al.* [112] and Noordegraaf *et al.* [5]. Unfortunately, the photonic bandgap fibers were made by infiltrating with a liquid with an refractive index that was above that of silica to obtain the bandgap effect, and thus will not work for aqueous solutions since water has a refractive index which is less that of silica.

5.2.1   Theoretical considerations

Numerically, the sensitivity can be studied using full numerical approach or semi-analytic approaches. A full numerical study provides readily the results, but does not give any explanations. The semi-analytical approach requires less computation time, but this itself is not important. Rather, the semi-analytic approach provides an understanding and identifies relevant parameters. We rely on the this approach.

A common tool for evaluating small changes is using perturbation theory. Proceeding along the lines of the usual Rayleigh-Schrödinger perturbation theory the fields ($\mathbf{E}$) and eigenvalues (ω) of Eq. (3.5) are expanded

a dimensionless parameter, η, to describe the response to a perturbation to the dielectric function, $\eta\Delta\varepsilon$: $\mathbf{E}(\eta) = \mathbf{E} + \eta\Delta\mathbf{E}_1 + \eta^2\Delta\mathbf{E}_2 + \dots$ and $\omega(\eta) = \omega + \eta\Delta\omega_1 + \eta^2\Delta\omega_2 + \dots$. Inserting these expansions in Eq. (3.5) and collecting η to first order yields a correction to the frequency

$$\Delta\omega = -\frac{\omega}{2}\frac{\int_\Omega d\mathbf{r}_\perp \mathbf{E}^*(\mathbf{r}_\perp)\Delta\varepsilon(\mathbf{r})\mathbf{E}(\mathbf{r}_\perp)}{\int_\Omega d\mathbf{r}_\perp \mathbf{E}^*(\mathbf{r}_\perp)\varepsilon(\mathbf{r})\mathbf{E}(\mathbf{r}_\perp)} + \mathcal{O}(\eta^2), \quad \text{const. } \beta, \quad (5.7)$$

where subscript '1' has been omitted on the frequency shift, $\Delta\omega$, and the asterisk indicates complex conjugate. The expression is exact until second order in η, thus for sufficiently small perturbations the shift is exact.

We work with refractive indices rather than the dielectric function and the perturbation inside the holes rewrites $\Delta\varepsilon = (n_\mathrm{h}+\Delta n_\mathrm{h})^2 - n_\mathrm{h}^2 \simeq 2n_\mathrm{h}\Delta n_\mathrm{h}$, where n_h is the refractive index of the holes, e.g. that of water or air. The integral over the perturbation is then an integral of a constant times $|\mathbf{E}|^2$ over the holes in the fiber cross section of the PCF. It is then easy to show that the wavelength shift is proportional to the fraction of field energy intensity, $u = \frac{1}{2}\mathbf{D}^* \cdot \mathbf{E}$, inside the air holes,

$$f_u \equiv \frac{\int_\mathrm{holes} d\mathbf{r}_\perp \mathbf{D}^*(\mathbf{r}_\perp) \cdot \mathbf{E}(\mathbf{r}_\perp)}{\int_\mathrm{PCF} d\mathbf{r}_\perp \mathbf{D}^*(\mathbf{r}_\perp) \cdot \mathbf{E}(\mathbf{r}_\perp)}. \quad (5.8)$$

In Sec. 2 the field fraction, f_u, appears from heuristic arguments, but here it has been derived rigorously. The field fraction is thus a fundamental parameter for any PCF sensor application. The first correction Eq. (5.7) can be written more compactly as

$$\frac{d\omega}{dn_\mathrm{h}} = -f_u\frac{\omega}{n_\mathrm{h}}, \qquad \text{const. } \beta. \quad (5.9)$$

For the calculations in following, the change in effective index at a fixed frequency is interesting rather than the change in frequency at a fixed propagation constant. Using partial derivatives we get $\Delta\omega = \frac{\partial\omega}{\partial\beta}\Delta\beta + \frac{\partial\omega}{\partial n_\mathrm{h}}\Delta n_\mathrm{h}$. At constant frequency $\Delta\omega = 0$ we get

$$\begin{aligned}\frac{dn_\mathrm{eff}}{dn_\mathrm{h}} &= \frac{1}{k}\frac{d\beta}{dn_\mathrm{h}} \\ &= \frac{n_\mathrm{g}}{n_\mathrm{h}}f_u, \qquad \text{const. } \omega, \quad (5.10)\end{aligned}$$

where $\frac{1}{\omega}\frac{d\omega}{dn_\mathrm{h}} = f_u$ The change in effective index is again proportional to the field fraction. The appearance of the group index can be interpreted as the

change is proportional to the time the electromagnetic wave interacts with the hole content, since the interaction time, t_f, is proportional to the inverse of the group velocity of electromagnetic wave, $t_f \propto 1/v_g = n_g/c_0$.

To obtain the resonant wavelength shift of an LPG, the result is inserted in Eq. (5.4) to obtain

$$\frac{d\lambda_r}{dn_h} = \frac{\lambda_r}{\bar{n}_g}\left(\frac{n_{g,co}}{n_h}f_{u,co} - \frac{n_{g,cl}}{n_h}f_{u,cl}\right), \tag{5.11}$$

where $f_{u,co}$ and $f_{u,cl}$ are the field fractions for the core and cladding modes, which may be very different. This expression is dominated by two variables: the group index mismatch, $\bar{n}_g$, and the field fraction for the cladding mode, $f_{u,cl}$ which is usually considerably large than the corresponding value for the core mode. The equation may divided by the resonance wavelength to obtain the dimensionless sensitivity, $\gamma_{RI} = \frac{1}{\lambda_r}\left|\frac{d\lambda_r}{dn_h}\right|$. The quality factor becomes

$$\begin{aligned} Q_{RI} &= \frac{1}{\lambda_{FWHM}}\left|\frac{d\lambda_r}{dn_h}\right| \\ &= 1.2\frac{L}{\lambda_r}\left|\frac{n_{g,co}}{n_h}f_{u,co} - \frac{n_{g,cl}}{n_h}f_{u,cl}\right|, \end{aligned} \tag{5.12}$$

which has no spurious enhancements due to the group index mismatch. Again, we realize that $f_{u,cl}$ is the dominating parameter for refractive index sensing since $f_{u,cl}$ is generally much larger than $f_{u,co}$ as seen in Figs. 5.3 and 5.5.

5.2.2 Experimental and numerical characterization

First, it is tried to validate the presented theory by accurate calculations on a specific PCFs, namely the LMA10. Secondly, PCF-LPGs are infiltrated with water and methanol to investigate the refractive index sensitivities. The infiltration increases the refractive index of the holes from 1.0 to ~1.33. The refractive index contrast between the hole and base material is thus reduced from 1.45-1.00 = 0.45 to 1.45-1.33 = 0.12. This produces a large shift in the resonance wavelength as seen in Figs. 5.2 and 5.4. Although the RI sensitivity can be estimated from these shifts, the sensitivity is not linear over such a broad wavelength range. Instead, the thermo-optic effect of the liquids is used. By increasing the temperature the refractive index of the liquids decreases according to their thermo-optic coefficients: $c_{H_2O}(700\,nm) = -1.8 \times 10^{-4}/°C$, $c_{Meth.}(839\,nm) = -4.1 \times 10^{-4}/°C$. The refractive index of the liquids are given in Fig. 5.1 due to different sources, the
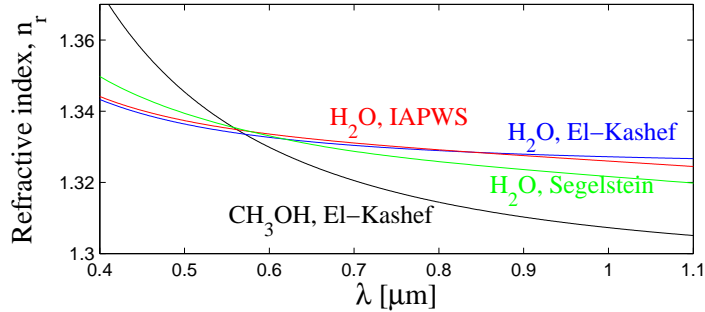
Figure 5.1: Refractive indices of the used liquids. The refractive index of H_2O according to different sources: The International Association for the Properties of Water and Steam (IAPWS), El-Kashef, and David Segelstein. The refractive index of methanol is due to El-Kashef.

International Association for the Properties of Water and Steam (IAPWS) [95], El-Kashef [113], and David Segelstein [94]. The data for H_2O differ slightly for the different sources. The data by Segelstein appear to be the least accurate, but his data also include the imaginary part of the refractive index accounting for absorbtion or optical heating of the water. The thermal tuning of the PCF-LPG is negligible and will be addressed in more detail in a following section.

For the experiments with methanol (CH_3OH) four PCF-LPGs are prepared with the grating periods, 820, 740, 620, and 580 μm and 60 periods, making the respective LPGs 49, 44, 37, and 35 mm in length. Methanol was chosen because the thermo-optic coefficient is larger than that of water, their refractive indices are similar. The methanol is infiltrated into the PCF-LPGs by using a pressure chamber with an overhead of 200 kPa. The methanol was degassed 30 min in vacuum to avoid the formation of air bubbles inside the PCF-LPGs. The PCF-LPG can also be filled using capillary forces, but by using an overhead the methanol will exit at the outside PCF-facet, and with an optical microscope ($\times 5$) it is possible verify that no air bubbles exited. The resonance wavelengths are presented in Table 5.1 and the spectra are presented in Fig. 5.2. The weakening of the resonance dip is believed to be caused by increased attenuation of the cladding modes constant, according to Figs. 4.3 and 4.7, by increasing confinement losses due to poorer guidance and absorbtion by the methanol.
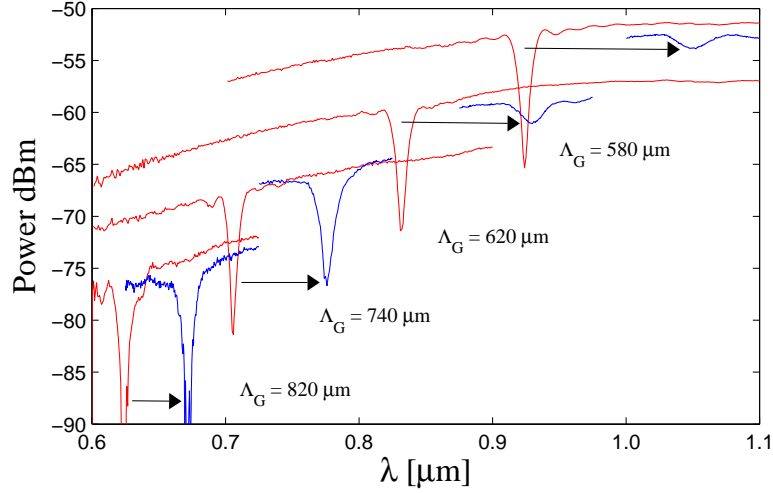
Figure 5.2: The sensitivity of the methanol filled PCF-LPG on temperature (blue). The arrows indicate the resonance shifts from the air filled PCF-LPGs (red)
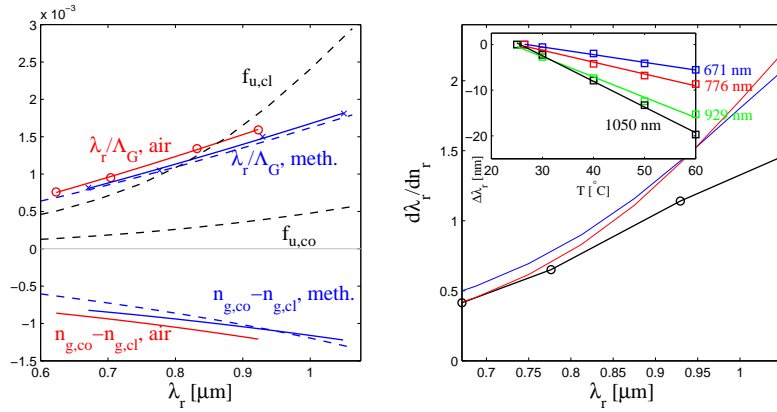
Figure 5.3: Left: λ_r/Λ_G and group index mismatch plots for air and methanol filled LPGs. Dashed lines: calculations (see text). Right: sensitivity experimental (black) and calculated (blue) and calculated using experimental $\bar{n}_g$ (red). Inset: resonance wavelength shift as function of temperature.

	Air	**Methanol**			
Λ_G	λ_r	λ_r	$\frac{\mathrm{d}\lambda_r}{\mathrm{d}n_r}$	n_r	$\frac{\mathrm{d}n_r}{\mathrm{d}T}$
820 μm	623 nm	671 nm	415nm	1.3228	-4.067×10^{-4}
740 μm	704 nm	776 nm	651nm	1.3157	-3.977×10^{-4}
620 μm	832 nm	929 nm	1140nm	1.3093	-3.896×10^{-4}
580 μm	923 nm	1050 nm	1460nm	1.3061	-3.856×10^{-4}

Table 5.1: Resonant wavelengths, λ_r, and grating periods, Λ_G. The resonant wavelengths for methanol filled PCF-LPGs and the corresponding material parameter for methanol, n_r, $\frac{\mathrm{d}n_r}{\mathrm{d}T}$, at the resonance wavelength.
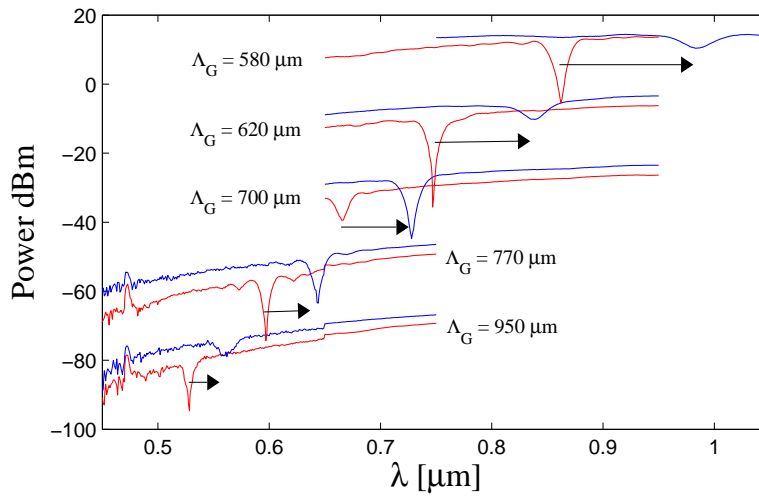
Figure 5.4: The sensitivity of the water filled PCF-LPG on temperature (blue). The arrows indicate the resonance shifts from the air filled PCF-LPGs (red)

The refractive index of the methanol was tuned by temperature. The PCF-LPGs were then mounted onto a heater stage with temperature control (MC60 & TH60, Linkam Scientific Instruments). The temperature was increased in steps of 5°C up to 60°C. The refractive index of the methanol decreases with temperature, since the thermo-optic coefficient is negative causing a blue-shifting the resonance wavelengths, Table 5.1 and Fig. 5.3. Following each experiment the temperature was decreased to 30°C to esti-
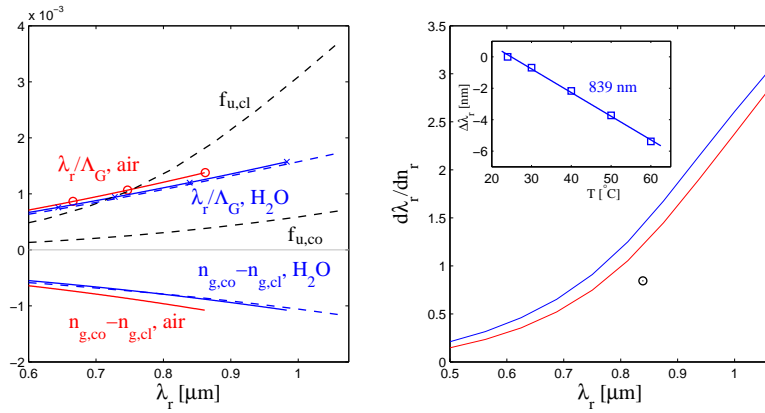
Figure 5.5: Left: λ_r/Λ_G and group index mismatch plots for air and water filled LPGs. Dashed lines: calculations (see text). Right: sensitivity experimental (black) and calculated (blue) and calculated using experimental $\bar{n}_g$ (red). Inset: resonance wavelength shift as function of temperature.

mate the hysteresis. The hysteresis was 1.4, 0.4, 0.05, and -1.0 nm, for the grating pitch Λ_G = 580, 620, 740, and 820 μm, respectively. The constant for the linear wavelength shift as function of temperature, $\frac{d\lambda_r}{dT}$, is plotted in Fig. 5.3. The constant clear increases with wavelength, experiencing a three fold enhancement over a 400 nm range. As mentioned in the previous subsection, the dominating parameters for the refractive index sensitivity is the group index mismatch, $\bar{n}_g$, and the field fraction for the cladding mode, $f_{u,cl}$, since this larger than $f_{u,co}$ as seen in Figs. 5.3 and 5.5. The field fraction can evaluated easily to a high precision using numerical simulations and is plotted for methanol filled PCF-LPG in Fig. 5.3. $\bar{n}_g$ is both numerically and experimentally prone to error. This is because the first and last term in $\bar{n}_g = \bar{n}_{eff} - \lambda\partial_\lambda\bar{n}_{eff}$ cancel to some extent. Fortunately, the group index mismatch can be estimated directly from experimental data, by replacing

Λ_{G}	**Air**	**H$_2$O**			
	λ_{r}	λ_{r}	$\frac{\mathrm{d}\lambda_{\mathrm{r}}}{\mathrm{d}n_{\mathrm{r}}}$	n_{r}	$\frac{\mathrm{d}n_{\mathrm{r}}}{\mathrm{d}T}$
950 μm	528.3 nm	561.9 nm	N.A.	1.3347	-1.82$\times10^{-4}$
850 μm	597.0 nm	644.1 nm	N.A.	1.3323	-1.80$\times10^{-4}$
770 μm	665.9 nm	728.0 nm	N.A.	1.3304	-1.79$\times10^{-4}$
700 μm	746.9 nm	839.0 nm	844 nm	1.3284	-1.78$\times10^{-4}$
625 μm	862.1 nm	983.1 nm	N.A.	1.3262	-1.77$\times10^{-4}$

Table 5.2: Resonant wavelengths, λ_{r}, and grating periods, Λ_{G}. The resonant wavelengths for water filled PCF-LPGs and the corresponding material parameter for methanol at the resonance wavelength.

$\lambda_{\mathrm{r}}/\Lambda_{\mathrm{G}} = \bar{n}_{\mathrm{eff}}$, in the expression for $\bar{n}_{\mathrm{eff}}$

$$\bar{n}_{\mathrm{g}} = \lambda_{\mathrm{r}}/\Lambda_{\mathrm{G}} - \lambda_{\mathrm{r}}\frac{\mathrm{d}\left(\lambda_{\mathrm{r}}/\Lambda_{\mathrm{G}}\right)}{\mathrm{d}\lambda_{\mathrm{r}}}, \qquad (5.13)$$

where the grating pitch, Λ_{G}, is taken to be equal to the beat length.

In the numerical simulations the effective indices is evaluated as described in the previous chapter. For the silica a Sellmeier expression is used while for the methanol, the refractive index is approximated by empirical Cauchy expressions, $n(\lambda) = A + B/\lambda^2$, with the fitted parameters (400-800 nm): methanol $A = 1.29461 \pm 1 \times 10^{-5}, B = 12706.1 \pm 0.1\mathrm{nm}^2$, due to some accurate measurements by El-Kashef [113]. The thermo-optic coeficient of methanol is dependent on the wavelength and can be found using the equation of Murphy and Alpert. The PCF structure parameters are pitch $\Lambda_{\mathrm{G}} = 7.12$ μm and hole diameter $d/\Lambda = 0.478$ estimated in the SEM in Fig. 4.12.

The procedure described above was repeated with demineralized water (H$_2$O) instead of methanol. The refractive index of H$_2$O is calculated using data from the IAPWS. The thermo-optic coefficient calculated with these data agreed poorly with the accurate measurements of El-Kashef who's data was used instead for thermo optic-coefficient while retaining the IPAWS data for the refractive index. The data for the refractive index agree well, 5.1. The results are summarized in Table 5.2 while the spectra are seen in Fig. 5.4.

The infiltration of water into PCF-LPG also causes larger wavelength shifts than methanol since its refractive index is slightly higher (Fig. 5.1). The

large-core	Refractive index sensing			
PCF	γ_{RI}	Q_{RI}	$\Delta\lambda/\Delta n_{\mathrm{h}}$ [nm]	λ_{FWHM}
LPG, 600 nm	1.6	43	980 nm	23 nm
LPG, 900 nm	3.2	88	2700 nm	32 nm
LPG, 1550 nm	14	210	22×10^3 nm	109 nm
BG, 600 nm	0.10×10^{-3}	5.8	0.060 nm	10 pm
BG, 900 nm	0.34×10^{-3}	13	0.30 nm	24 pm
BG, 1550 nm	1.6×10^{-3}	35	2.5 nm	70 pm
small-core	Refractive index sensing			
PCF	γ_{RI}	Q_{RI}	$\Delta\lambda/\Delta n_{\mathrm{h}}$	λ_{FWHM}
LPG, 600 nm	73	6500	-44×10^3 nm	6.8 nm
LPG, 900 nm	11	8600	-9.8×10^3 nm	1.1 nm
LPG, 1550 nm	6.4	7400	-9.9×10^3 nm	1.3 nm
BG, 600 nm	6.0×10^{-3}	350	3.6 nm	10 pm
BG, 900 nm	18×10^{-3}	690	16 nm	23 pm
BG, 1550 nm	74×10^{-3}	1700	115 nm	70 pm

Table 5.3: Comparison of sensitivity and the quality factor for PCF refractive index sensors for both LPGs and BGs at different wavelengths for two different PCFs: a large core of 10 μm and a small core PCF of 2.5 μm, with parameters $\Lambda = 7$ μm and μm$/\Lambda = 0.45$ and $\Lambda = 2$ μm, $d/\Lambda = 0.75$, respectively.

temperature optic-coefficient is roughly half that of water and the temperature tuning of the resonant wavelengths produces smaller shifts (Fig. 5.4, Table 5.2).

For both liquids the theoretical calculations overestimate the sensitivity. To some extent this is caused by an underestimation of the group index mismatch, $\bar{n}_{\mathrm{g}}$, and a subsequent overestimation of the wavelength shift according to Eq. (5.11). This can be corrected by replacing the theoretical group index mismatch with the experimental obtained. In Figs. 5.3 and 5.5 this is seen to correct the discrepancy to some degree.

The investigation has until now been done solely on the LMA10 PCF. Small core PCFs can achieve field fractions an order of magnitude greater. To make a general survey, we study a PCF-LPG where the effective cladding index is assumed to be equal to the fundamental space filling mode. The validity of the approximation can verified in Figs. 4.6 and 4.7 for a PCF

structure with seven rings of holes. The survey is described in more detail in Ref. [6]. As a comparison two PCFs are studied: a large core fiber, $\Lambda_{\mathrm{G}} = 7$ μm, $d/\Lambda = 3.15$ μm$/\Lambda = 0.45$, similar to the LMA10, with a mode field diameter of 10 μm, and a small core PCF, $\Lambda_{\mathrm{G}} = 2$ μm, $d/\Lambda = 1.5$ μm$/\Lambda = 0.75$, with a mode field diameter of $2\Lambda - d = 2.5$ μm. The results are presented in Table 5.3. As a further comparison the sensitivity, quality, and FWHM for Bragg gratings are also included. The length of the grating enters in the quality factor and has been assumed to be $L = 30$mm. It is seen that the dimensionless sensitivity, γ_{RI}, for the two PCFs are of the same order of magnitude, but the quality factor, Q_{RI}, differs by two orders of magnitude. This enhancement is caused by a narrower λ_{FWHM} since it is much smaller for the small core PCF. Note, that even though it would be expected that a small core PCF would perform better because of the higher field fraction, the enhancement is due the dispersion properties giving a small λ_{FWHM} through a larger group index mismatch, $\bar{n}_{\mathrm{g}}$, by Eq. (4.19) rather than the higher field fraction.

5.3   Label-free biosensing

Biosensing rely on capturing biomolecules selectively by a biochemical element. The second part of biosensing is the optical detection, and the focus is on this part in the thesis. In the present case this amounts to measuring the average thickness of a layer of biomolecules on the surface of a hole. Since the thickness of the layer of biomolecules is much smaller than the wavelength, $t_{\mathrm{Bio}} < \lambda$, we may apply perturbation theory. Capturing molecules on the exterior of an LPG in a standard optical fiber has been studied by Wang *et al.* [114]

The refractive index of biomolecules is ~ 1.45 and thus constitutes a large change in refractive index compared with water, $n_{\mathrm{r}} \sim 1.33$. For such high-index contrast variations in the PCF the standard perturbation theory in Eq. (5.7) does not apply. The reason for this is the vectorial nature of the electromagnetic fields, rendering some polarizations of the electric field discontinuous at the material boundaries. The problem was first addressed by Johnson *et al.* [115] who derived a modified equation for the first order frequency shift,

$$\Delta\omega = -\frac{\omega}{2} \int d\mathbf{r}_\perp \, \Delta\varepsilon(\mathbf{r}) \big|\mathbf{E}_\parallel(\mathbf{r}_\perp)\big|^2 + \Delta\Big(\frac{1}{\varepsilon(\mathbf{r})}\Big)\big|\mathbf{D}_\perp(\mathbf{r}_\perp)\big|^2. \qquad (5.14)$$

$\mathbf{E}_\parallel$ is the electric field parallel to the surface and $\mathbf{D}_\perp$ is the electric charge field orthogonal to the surface. Although the task of evaluating the integral

posed by the equation numerically above certainly is manageable, there exists a simpler solution to the problem. Since $n_{\mathrm{r,Bio}} \sim n_{\mathrm{SiO_2}}$ and the layer is supposed to be *uniform* on the entire surface we may without loss of generality use

$$\frac{\mathrm{d}n_{\mathrm{eff}}}{\mathrm{d}t_{\mathrm{Bio}}} = -2\frac{\mathrm{d}n_{\mathrm{eff}}}{\mathrm{d}d}, \tag{5.15}$$

where d is the diameter of the holes. To recapitulate, if the biofilm forms a uniform layer on the scale of a wavelength, and the average refractive index of the layer is 1.45, then it is an exact assumption that the deposition of a layer of molecules t_{Bio} thick corresponds to a *decrease* of the diameter of the holes of -2 t_{Bio}. The sensitivity then becomes

$$\frac{\mathrm{d}\lambda_{\mathrm{r}}}{\mathrm{d}n_{\mathrm{h}}} = \frac{2\lambda_{\mathrm{r}}}{\bar{n}_{\mathrm{g}}}\left(\frac{\mathrm{d}n_{\mathrm{co}}}{\mathrm{d}d} - \frac{\mathrm{d}n_{\mathrm{cl}}}{\mathrm{d}d}\right) \tag{5.16}$$

where the corresponding expression for γ_{Bio} is obtained by eliminating λ_{r} on the right hand side. The quality factor becomes

$$
\begin{aligned}
Q_{\mathrm{Bio}} &= \frac{1}{\lambda_{\mathrm{FWHM}}}\frac{\mathrm{d}\lambda_{\mathrm{r}}}{\mathrm{d}n_{\mathrm{h}}} \\
&= 2.4\frac{L}{\lambda_{\mathrm{r}}}\left|\frac{\mathrm{d}n_{\mathrm{co}}}{\mathrm{d}d} - \frac{\mathrm{d}n_{\mathrm{cl}}}{\mathrm{d}d}\right|.
\end{aligned} \tag{5.17}
$$

The sensitivities and the quality factor are shown in Fig. 5.6. Also shown are the corresponding sensitivities if the numerical group index mismatch is replaced with the experimental group index mismatch obtained from Fig. 5.5. The numerical and experimental group index mismatch differ slightly as seen in the inset Fig. 5.6.

As a preliminary experiment we have carried out an experiment where poly-L-lysine (PLL) was immobilized onto a the surfaces of the holes. In an aqueous environment the positively charged PLL binds to the negatively charged silica surface through a ionic bond and forms a layer ~ 5 nm thick on average. Onto the positively charged PLL it is possible to immobilize double stranded DNA molecules since the phosphate groups that constitute the backbone of the spirals are negatively charged. Double stranded DNA is approximately 2 nm in diameter. The biomolecular complex is presented in Fig. 5.7. The biochemical procedure is described in more detail in Ref. [4]. The LPG had 26 periods and a grating period of 700 μm with a resonance wavelength. The piece of PCF was 30 cm in total length. The immobilization of PLL causes a shift of the resonance wavelength of $t_{\mathrm{PLL}} = 6.7$ nm, and
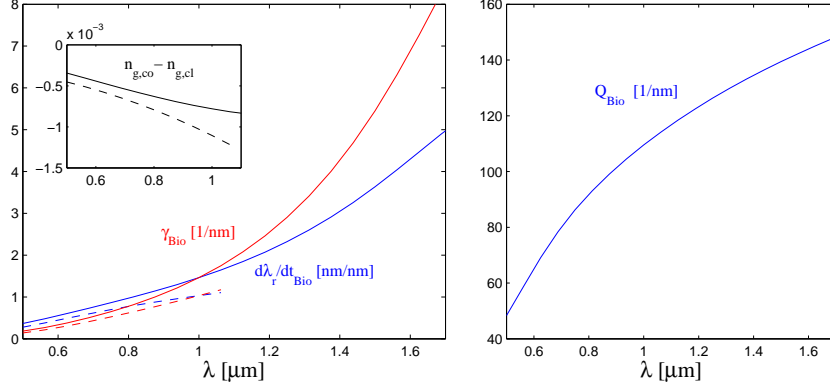
Figure 5.6: Sensitivity, dimensionless sensitivity (γ_{Bio}), and quality factor (Q_{Bio}) for the LMA10. The dashed lines represents the results where the numerical group index mismatch is replaced with experimental group index mismatch (inset).

the immobilization of DNA causes a shift of the resonance wavelength of $t_{\mathrm{PLL}} = 2.3$ nm. A broadband lightsource (Ocean Optics HL-2000) was used with an ANDO AQ-6315A Optical Spectrum Analyzer (450-1700 nm) set at a resolution of 2 nm. The resulting spectra are seen in Fig. 5.8. The PLL and DNA may form monolayers but it is likely that the layers are non-uniform at a molecular level. This, of course, makes no difference for the optical sensing, since the variations (~ 1nm) are much smaller than the wavelength ($\sim 1\mu$m). But it is difficult to estimate the exact thickness of the monolayers. Ignoring this uncertainty, gives the sensitivities for $\Delta\lambda_{\mathrm{r}}/t_{\mathrm{PLL}} = 6.7$nm/5nm $= 1.3$ nm/nm for the PLL and $\Delta\lambda_{\mathrm{r}}/t_{\mathrm{DNA}} = 2.3$nm/2nm $= 1.2$ nm/nm for the DNA, which agree well with the numerical results 1.8 nm/nm and if the experimental group index mismatch is used the sensitivity is 1.4 nm/nm. In the case of refractive index sensing the theoretical predictions overestimate the sensitivities. If the sensitivity is also overestimate in the case of biosensing, then the PLL and DNA most likely form monolayers on average.

With refractive index sensing the quality of the refractive index sensor could be enhanced with a PCF with a smaller core. Again the effective cladding index is assumed to be equal to the fundamental space filling mode. The

large-core	Biosensing			
PCF	γ_{Bio} [1/nm]	Q_{Bio} [1/nm]	$\Delta\lambda/t_{\mathrm{Bio}}$	λ_{FWHM}
LPG, 600 nm	2.4×10^{-3}	63×10^{-3}	1.4 nm/nm	23 nm
LPG, 900 nm	3.0×10^{-3}	85×10^{-3}	2.7 nm/nm	32 nm
LPG,1550 nm	8.1×10^{-3}	120×10^{-3}	12 nm/nm	109 nm
BG, 600 nm	3.0×10^{-7}	17×10^{-3}	0.18 pm/nm	10 pm
BG, 900 nm	6.5×10^{-7}	25×10^{-3}	0.59 pm/nm	24 pm
BG, 1550 nm	19×10^{-7}	41×10^{-3}	2.8 pm/nm	70 pm
small-core	Biosensing			
PCF	γ_{Bio} [1/nm]	Q_{Bio} [1/nm]	$\Delta\lambda/t_{\mathrm{Bio}}$	λ_{FWHM}
LPG, 600 nm	89×10^{-3}	7.9	-54 nm/nm	6.8 nm
LPG, 900 nm	7.7×10^{-3}	6.2	-7.0 nm/nm	1.1 nm
LPG, 1550 nm	2.7×10^{-3}	3.0	-4.1 nm/nm	1.3 nm
BG, 600 nm	17×10^{-6}	1.0	10 pm/nm	10 pm
BG, 900 nm	35×10^{-6}	1.3	31 pm/nm	23 pm
BG, 1550 nm	83×10^{-6}	1.9	130 pm/nm	70 pm

Table 5.4: Comparison of sensitivity and the quality factor for PCF biosensors for both LPGs and BGs at different wavelengths for two different PCFs: a large core of 10 μm and a small core PCF of 2.5 μm, with parameters $\Lambda = 7$ μm and μm/$\Lambda = 0.45$ and $\Lambda = 2$ μm, $d/\Lambda = 0.75$, respectively.
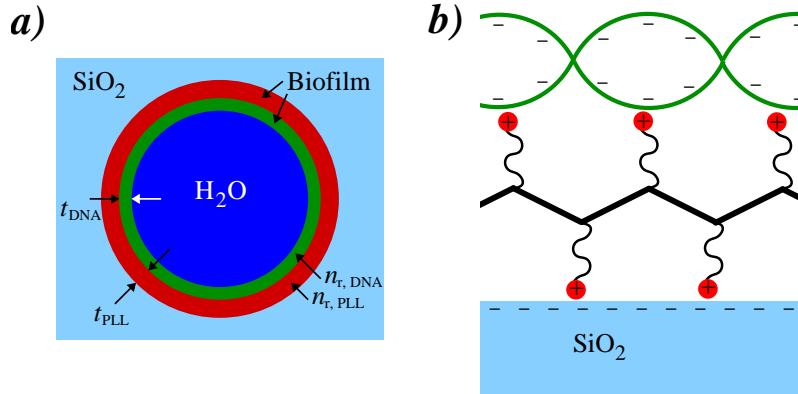
Figure 5.7: a) A hole of a photonic crystal fiber. The side is coated with poly-L-lysine (PLL) and DNA. The thickness of the biofilms is vastly exaggerated compared to the hole diameter. b) The molecular structure of poly-L-lysine (red & black) with positive charges immobilized onto the negatively charged silica surface (SiO_2). The negatively charged DNA (green) is immobilized on the poly-L-lysine

validity can be checked in Figs. 4.6 and 4.7. The survey is described in more detail in Ref. [6]. As a comparison two PCFs are studied: a large core fiber, $\Lambda = 7$ μm, $d/\Lambda = 3.15$ μm$/\Lambda = 0.45$, similar to the LMA10, with a mode field diameter of 10 μm, and a small core PCF, $\Lambda = 2$ μm, $d/\Lambda = 1.5$ μm$/\Lambda = 0.75$, with a mode field diameter of $2\Lambda - d = 2.5$ μm. The results are presented in Table 5.4 and the corresponding values for Bragg gratings are also included. The length of the grating has been assumed to be $L = 30$ mm. For the large core we see an increase in the dimensionless sensitivity, γ_{Bio} with increasing wavelength. This generally also holds for BGs. Surprisingly, the sensitivity actually *decreases* for a small core PCF with increasing wavelength. The quality factor, Q_{Bio}, also decreases with wavelength. It would be expected that the biosensing sensitivity would follow the behavior of the refractive index sensor, which itself is dependent on the field fractions of the two resonant modes. For biosensing, the performance is not governed by the field fractions in the holes, rather it it dependent on the field energy intensity at the surface of the holes. This opens the possibility if making highly sensitive biosensors with low cross sensitivity to refractive index changes. Such refractive index changes can be caused be changing the aqueous solutions or therm-optic effects.
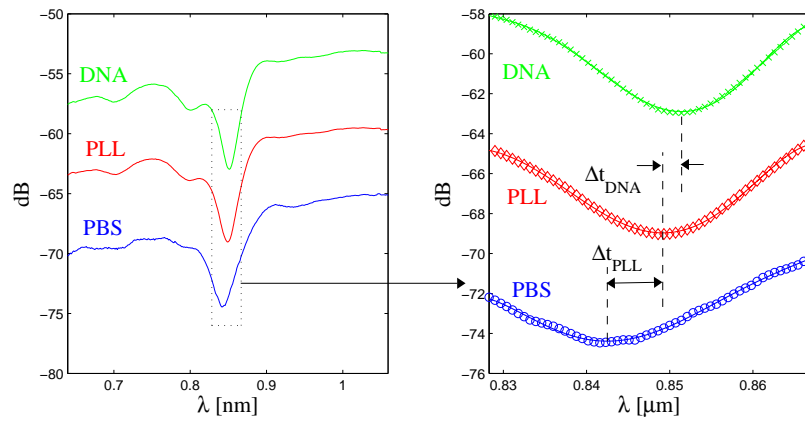
Figure 5.8: Left: The experimental transmission spetra for PBS (phosphate buffered saline solution), PLL (poly-L-lysine) and double-stranded DNA. The curve for PBS shows the absolute transmission in dBm, The two other curves, PLL, DNA, are offset on the y-axis for clarity. Right: Close up of dotted rectangle. The transmission spetra for PBS (circles), PLL (diamonds) and double stranded DNA (crosses). Each spectrum has been interpolated with a curve. The curve for PBS shows the absolute transmission in dBm, The two other curves, PLL, DNA, are offset on the y-axis for clarity

5.4   Susceptibility to temperature

A major concern in sensors, particularly biosensors, is the cross sensitivity to temperature. Temperature changes both the material refractive indices of the PCF through the thermo-optic effect and also by expansion of the PCF structure. The thermo-optic coefficient for the refractive index of silica glass is $\eta_o \simeq 9 \times 10^{-6}/\text{K}$ and the thermal expansion coefficient is $\alpha_T \simeq 0.55 \times 10^{-6}/\text{K}$. Since the perturbation of the PCF is sufficiently small we may expand the effective index to first order in the temperature. Since both the pitch, length and the refractive index of the silica are dependent on silica, we use the partial derivatives of the effective refractive index (the chain rule)

$$
\begin{aligned}
\frac{\partial n_{\text{eff}}}{\partial T}\Big|_{\lambda_{\text{r}}} &= \frac{\mathrm{d}n_{\text{eff}}\big(L(T), \Lambda(T), n_{\text{r}}(T)\big)}{\mathrm{d}T} \\
&= \frac{\partial n_{\text{eff}}}{\partial L}\frac{\partial L}{\partial T} + \frac{\partial n_{\text{eff}}}{\partial \Lambda}\frac{\partial \Lambda}{\partial T} + \frac{\partial n_{\text{eff}}}{\partial n_{\text{b}}}\frac{\partial n_{\text{b}}}{\partial T}.
\end{aligned}
\tag{5.18}
$$

The full derivation is carried out in Ref. [6] and we will not go into details. It must be mentioned that the effective index change, through the thermo-optic coefficient, in the base material is proportional to $n_{\text{g}}(1 - f_{\text{u}})$. This should not come as a surprise since the effective change by a refractive index change of the holes is proportional to the product of the field fraction and the group index, $n_{\text{g}}f_{\text{u}}$, in Eq. (5.11). The final equation yields,

$$
\frac{\partial \bar{n}_{\text{eff}}}{\partial T}\Big|_{\lambda_{\text{r}}} = \alpha\big(\bar{n}_{\text{eff}} + \Lambda\frac{\partial \bar{n}_{\text{eff}}}{\partial \Lambda}\big) + \frac{\eta_o}{n_{\text{SiO}_2}}\Big[(1 - f_{u,\text{co}})n_{\text{g,co}} - (1 - f_{u,\text{cl}})n_{\text{g,cl}}\Big].
\tag{5.19}
$$

The first term is due to the elongation of the PCF through the thermal expansion coefficient. The second term is the widening of the PCF cross section by the thermal expansion coefficient.

    We evaluate this expression numerically using FEM simulations. The same LMA10 structure values as in the previous sections, $\Lambda_{\text{G}} = 7.12\ \mu\text{m}$ pitch and $d/\Lambda = 0.478$, are used. The partial derivative in Eq. (5.19) is evaluated using a finite difference. The results are plotted in Fig. 5.9. Two experiments were conducted with PCF-LPGs in the LMA10 with grating periods, $\Lambda_{\text{G}} = 500\ \mu\text{m}$, and 120 periods. The resonant wavelengths were 1083 nm. There is a remarkable agreement of the numerical simulation and the experimental data. The agreement is within the expected numerical and experimental uncertainty, e.g. the thermo-optic coefficient is only known
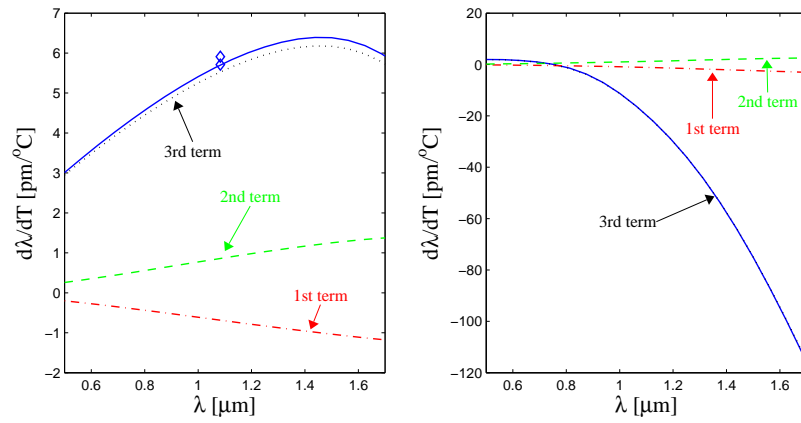
Figure 5.9: Left: The numerically calculated temperature sensitivity of an air filled LPG. The two diamonds are experimental measurements. The terms (dashed and dotted lines) referred to, are given in Eq. (5.18) Right: The numerically calculated temperature sensitivity contribution of a methanol filled LPG from the PCF-LPG itself, *i.e. ignoring the thermo-optic coefficient of methanol*. The terms (dashed and dotted lines) referred to, are given in Eq. (5.18)

with one decimal, and to minor extent, the agreement is coincidence. To demonstrate the influence of each term, these have been included in the plots. It is seen that the third term, the thermo-optic term is dominating, to extent because the two first terms cancel each other to a large extent. The third term involves both the group indices and the field fractions. Since the magnitude of the term is dependent on the cancelation of the core and cladding modes product of group index and field fraction, it is suspected that magnitude of the overall term increases when the field fraction is increased. To test this, a methanol filled PCF-LPG is numerically simulated with the contribution of the thermo-optic coefficient of methanol is neglected. I.e. the thermal response of the resonance wavelength if the methanol had a thermo-optic coefficient equal to zero. Indeed the sensitivity increases drastically (Fig. 5.9 right) and becomes negative, whereas it was positive for the air filled PCF-LPG. For the resonance wavelengths 623, 776, 929, 1050 nm given in Table 5.1 the sensitivity is $\frac{\mathrm{d}\lambda_\mathrm{r}}{\mathrm{d}T}(\mathrm{meth}) = 1.61, -0.55, -6.57, -15.25\,\mathrm{pm}/^\circ\mathrm{C}$, respectively. For a $35\,^\circ\mathrm{C}$ (=60-25 $^\circ\mathrm{C}$) increase in temperature leads to a negligible maximum error of -0.4 nm.

5.5 Conclusions

5.5.1 Discussion

The beat length in small core PCFs is too small to allow LPG inscription by the CO_2 laser method. LPGs in such PCFs may be inscribed using a new UV inscription method [97].

An expression for the temperature sensitivity has been derived heuristically by Shu *et al.* [92] but this expression is only valid for standard optical fibers and not for a non-circular, two material PCF. Petrovic *et al.* [116] have derived an expression similar to Eq. (5.19) but without the second term (thermal expansion of PCF cross-section) and with the third term to evaluated numerically rather than through the field fractions and group indices. In Fig. 5.9 it is seen that the sensitivity is controlled by the third term. The second term in Eq. (5.19) cancels almost with the first term and the term must be included to avoid significant errors. The estimation of the temperature sensitivity by Petrovic *et al.* overestimates by a factor of two, while the presented expression gives less than 5 %.

5.5.2 Summary

New expressions for the sensitivity for refractometers, biosensors, and temperature sensors have been rigorously derived, and presented for the first time, to the best of the author's knowledge. The expression are significantly different from previous expressions and are valid for PCFs. Very good agreement have been found with the experiment.

It has been shown that PCF-LPGs make highly sensitive refractometers. The PCF-LPGs have been characterized at different wavelengths and good correspondence with theory has been observed. As biosensors a standard PCF is fairly sensitive. The sensitivity and quality Q in both applications can likely augmented by two orders of magnitude as indicate by realistic numerical simulations.

Chapter 6

Conclusion

6.1 Outlook

The PCF-LPGs performs well in sensitivity; being sensitive to the layer of biomolecules and insensitive to temperature. By designing the PCF structure the sensitivities may be chosen according the present needs.

The future for label-free PCF-LPGs seem uncertain for a number of reasons, namely: response time, sample size, and production facilities. The fluidic flow is inherently slow in PCFs due to the small hole diameters. The hole diameters can be increased only at the expense the performance of the sensor. An SPR sensor has a minimal interaction area of $\sim 100~\mu m \times 100~\mu m = 10^4 \mu m^2$. This limits the minimal detectable amount of sample. An extremely optimized PCF-LPG has 6 holes of 3 μm in diameter and is 30 mm long. This gives an interaction area of $\sim 10^6 \mu m^2$, which is two orders of magnitude large than the SPR. Secondly, while planar photonic crystal waveguide technology can share production platforms with computer chips, no production facilities, to the author's best of knowledge, exist that can integrate PCFs in microfluidic system. There is a risk that production facilities may be too expensive to develop and run.

6.2 Summary

The integration of a PCF in a biochip has been demonstrated. The integrated 16 mm long piece of PCF was used in a biosensing experiment and was shown to be highly sensitive in an absorbance measurement.

The performance of PCF-LPGs for label-free biosensing has been studied using both numerics and experiments. PCF-LPGs require accurate numer-

ical modelling. It has been shown that such modeling can be done using FEM and further improved by exploiting the rotational symmetry of the triangular PCF structure. A highly efficient CO_2 laser inscription has been described. The automated setup can write LPG-PCFs of high quality. The fabricated LPG-PCFs have been compared with numerical simulations and good correspondence have been found for both the resonant wavelengths and the spectra. It has been argued that only well guided cladding modes with an overlap with the core can be resonant with the core mode.

Using rigorous perturbation theory it is shown that the sensitivity and the FWHM of the resonance dip are intimately related to the dispersion of the PCF. A quality factor, Q, for the sensitivity is proposed, since the sensitivity can be greatly enhanced by the waveguide dispersion without increasing the effective sensitivity. Expressions for the sensitivity with respect to refractive index and biosensing are derived and presented for the first time. An expression for the temperature sensitivity is also presented. To the best of the author's knowledge, this is the first time these expressions are derived correctly for PCF-LPGs. The expressions are validated with experiments.

In conclusion the PCF-LPG is sufficiently sensitive as a biosensor, and its sensitivity and Q may be improved by two orders of magnitude.

Bibliography

[1] L. Rindorf and N. A. Mortensen. Non-perturbative approach to high-index-contrast variations in electromagnetical systems. *Opt. Com.*, 261:181–186, 2006.

[2] L. Rindorf and N. A. Mortensen. Calculation of optical-waveguide grating characteristics using greens functions and dysons equation. *Phys. Rev. E*, 74:036616, 2006.

[3] L. Rindorf, P. E. Hoiby, J. B. Jensen, L. H. Pedersen, O. Bang, and O. Geschke. Towards biochips using microstructured optical fiber sensors. *Analytical and Bioanalytical Chemistry*, 385(8):1370–1375, 2006.

[4] L. Rindorf, J. B. Jensen, M. Dufva, L. H. Pedersen, P. E. Hoiby, and O. Bang. Biochemical sensing using photonic crystal fiber long-period gratings. *Opt. Express*, 14(18):8824–8831, 2006.

[5] Danny Noordegraaf, Lara Scolari, Jesper Lgsgaard, Lars Rindorf, and Thomas Tanggaard Alkeskjold. Electrically and mechanically induced long period gratings in liquid crystal photonic bandgap fibers. *Opt. Lett.*, 15:7901–7912, 2007.

[6] L. Rindorf and O. Bang. Sensitivity of photonic crystal fiber grating sensors: biosensing, refractive index, strain, and temperature sensing. *J. Opt. Soc. Am. B*, 25(3):310–324, 2008.

[7] L. Rindorf and O. Bang. Highly sensitive refractometer with photonic crystal fiber long-period grating. *Opt. Lett.*, 33(6):563–565, 2008.

[8] International Union of Pure and Applied Chemistry. "biosensor". Compendium of Chemical Terminology Internet edition.

[9] R. Bashir. Biomems: state-of-the-art in detection, opportunities and prospects. *Advanced Drug Delivery Reviews*, 56:1565–1586, 2004.

[10] O. S. Wolfbeis. Fiber-optic chemical sensors and biosensors. *Analytical Chemistry*, 78:3859–3873, 2006.

[11] I. Lundstrom B. Liedberg and E. Stenberg. Principles of biosensing with an extended matrix and surface-plasmon resonance. *Sens. Actuators B*, 11:63, 1993.

[12] Luc Bissonnette and Michel G Bergeron. Next revolution in the molecular theranostics of infectious diseases: microfabricated systems for personalized medicine. *Expert Review of Molecular Diagnostics*, 6(3):433–450, 2006.

[13] R. W. Boyd and J. E. Heebner. Sensitive disk resonator photonic biosensor. *Appl. Opt.*, 40:5742–5747, 2001.

[14] H. Y. Zhu, J. D. Suter, I. M. White, and X. D. Fan. Aptamer based microsphere biosensor for thrombin detection. *Sensors*, 6:785–795, 2006.

[15] E. Chow, A. Grot, L.W. Mirkarimi, M. Sigalas, and G. Girolami. Ultracompact biochemical sensor built with two-dimensional photonic crystal microcavity. *Opt. Lett.*, 29:1093–1095, 2004.

[16] S. John. Strong localization of photons in certain disordered dielectric superlattices. *Phys. Rev. Lett.*, 58:2486–2489, 1987.

[17] J. D. Joannopoulos, R. D. Meade, and J. N. Winn. *Photonic crystals: molding the flow of light*. Princeton University Press, Princeton, 1995.

[18] J. C. Knight, T. A. Birks, P. St. J. Russell, and D. M. Atkin. All-silica single-mode optical fiber with photonic crystal cladding. *Opt. Lett.*, 21:1547–1549, 1996.

[19] T. M. Monroe, D. J. Richardson, and P. J. Bennett. Developing holey fibres for evanescent field devices. *Electron. Lett.*, 35:1188–1189, 1999.

[20] Y. L. Hoo, W. Jin, C. Z. Shi, H. L. Ho, D. N. Wang, and S. C. Ruan. Design and modeling of a photonic crystal fiber gas sensor. *Appl. Opt.*, 42:3509–3515, 2003.

[21] K. L. Brogan and D. R. Walt. Optical fiber-based sensors: application to chemical biology. *Current Opinion in Chemical Biology*, 9:494–500, 2005.

[22] B. Lee. Review of the present status of optical fiber sensors. *Optical Fiber Technology*, 9:57–79, 2003.

[23] J. M. Fini. Microstructure fibres for optical sensing in gases and liquids. *Meas. Sci. & Technol.*, 15:1120–1128, 2004.

[24] T. Ritari, J. Tuominen, H. Ludvigsen, J. C. Petersen, T. Sørensen, T. P. Hansen, and H. Simonsen. Gas sensing using air-guiding photonic bandgap fibers. *Opt. Express*, 12:4080–4087, 2004.

[25] J. Henningsen, J. Hald, and J.C. Petersen. Experimental evidence for supercontinuum generation by fission of higher-order solitons in photonic fibers. *Opt. Express*, 12:10475–10482, 2005.

[26] F. M. Cox, A. Argyros, and M. C. J. Large. Liquid-filled hollow core microstructured polymer optical fiber. *Opt. Express*, 14:4135–4140, 2006.

[27] Y. N. Zhu, H. Du, and R. Bise. Design of solid-core microstructured optical fiber with steering-wheel air cladding for optimal evanescent-field sensing. *Opt. Express*, 14:3541–3546, 2006.

[28] S. O. Konorov, A. M. Zheltikov, and M. Scalora. Photonic-crystal fiber as a multifunctional optical sensor and sample collector. *Opt. Express*, 13:3454–3459, 2005.

[29] J. B. Jensen, L. H. Pedersen, P. E. Hoiby, L. B. Nielsen, T. P. Hansen, J. R. Folkenberg, J. Riishede, D. Noordegraaf, K. Nielsen, A. Carlsen, and A. Bjarklev. Photonic crystal fiber based evanescent-wave sensor for detection of biomolecules in aqueous solutions. *Opt. Lett.*, 29:1974–1976, 2004.

[30] S. Smolka, M. Barth, and O. Benson. Selectively coated photonic crystal fiber for highly sensitive fluorescence detection. *App. Phys. Lett.*, 90:111101, 2007.

[31] S. Smolka, M. Barth, and O. Benson. Highly efficient fluorescence sensing with hollow core photonic crystal fibers. *Opt. Express*, 15:12783–12791, 2007.

[32] V. Matejec, J. Mrazek, M. Hayer, I. Kasik, P. Peterka, J. Kanka, P. Honzatko, and D. Berkova. Microstructure fibers for gas detection. *Materials Science & Engineering C-Biometic and Supramolecular Systems*, 26:317–321, 2006.

[33] Matthew P. DeLisa, Zheng Zhang, Mira Shiloach, Saeed Pilevar, Christopher C. Davis, James S. Sirkis, and William E. Bentley. Evanescent wave long-period fiber bragg grating as an immobilized antibody biosensor. *Analytical Chemistry*, 72:2895–2900, 2000.

[34] M. C. Phan Huy, G. Laffont, Y. Frignac, V. Dewynter-Marty, P. Ferdinand, P. Roy, J-M Blondy, D. Pagnoux, W. Blanc, and B. Dussardier. Fibre bragg grating photowriting in microstructured optical fibres for refractive index measurement. *Meas. Sci. Technol.*, 17:992–997, 2006.

[35] M. C. Phan Huy, V. Dewynter-Marty, P. Ferdinand, P. Roy, J. L. Auguste, D. Pagnoux, W. Blanc, and B. Dussardier. Three-hole microstructured optical fiber for efficient fiber bragg grating refractometer. *Opt. Lett.*, 32:2390–2392, 2007.

[36] H. Yan, C. Gua, C. X. Yang, J. Liu, G. F. Jin, J. T. Zhang, L. T. Hou, and Y. Yao. Hollow core photonic crystal fiber surface-enhanced raman probe. *App. Phys. Lett..*, 89:204101, 2006.

[37] K. Kneipp, Y. Wang, H. Kneipp, L. T. Perelman, I. Itzkan, R. Dasari, and M. S. Feld. Single molecule detection using surface-enhanced raman scattering (sers). *Phys. Rev. Lett.*, 78:1667–1670, 1997.

[38] B. Gauvreau, A. Hassani, M. F. Fehri, A. Kabashin, and M Skorobogatiy. Photonic bandgap fiber-based surface plasmon resonance sensors. *Opt. Express*, 15:11413–11426, 2007.

[39] J. B. Jensen, P. E. Hoiby, G Emiliyanov, O Bang, L. H. Pedersen, and A. Bjarklev. Selective detection of antibodies in microstructured polymer optical fibers. *Opt. Express*, 13:5883–5889, 2005.

[40] G. Emiliyanov, J. B. Jensen, O. Bang, P. E. Hoiby, L. H. Pedersen, E. M. Kjaer, and L. Lindvold. Localized biosensing with topas microstructured polymer optical fiber. *Opt. Lett.*, 32:460–462, 2007.

[41] A. Dupuis, N. Guo, Y. Gao, N. Godbout, S. Lacroix, C. Dubois, and M. Skorobogatiy. Prospective for biodegradable microstructured optical fibers. *Opt. Lett.*, 32:109–111, 2007.

[42] C. Monat, Domachuk, and B. J. Eggleton. Integrated optofluidics: A new river of light. *Nature Photonics*, 1(2):106–114, 2007.

[43] K. B. Mogensen, H. Klank, and J. P. Kutter. Recent developments in detection for microfluidic systems. *Electrophoresis*, 25:3498–3512, 2004.

[44] O. Geschke, H. Klank, and P. Telleman. *Microsystem engineering of lab-on-a-chip devices*. Wiley-VCH, Weinheim, 2004.

[45] H. Bruus and K. Flensberg. *Many-Body Quantum Theory in Condensed Matter Physics*. Oxford University Press, Oxford, 2004.

[46] A. U. Haque, M. R. Chatni, G. Li, and D. M. Porterfield. Biochips and other microtechnologies for physiomics. *Expert Review of Proteomics*, 4:553–563, 2007.

[47] X. D. Hoa, A. G. Kirk, and M. Tabrizian. Towards integrated and sensitive surface plasmon resonance biosensors: A review of recent progress. *Biosens. & Bioelec.*, 23:151–160, 2007.

[48] S. Haeberle and R. Zengerle. Microfluidic platforms for lab-on-a-chip applications. *Lab on a Chip*, 7:1094–1110, 2007.

[49] C. S. Zhang and D. Xing. Miniaturized pcr chips for nucleic acid amplification and analysis: latest advances and future trends. *Nucleic Acids Research*, 35:4223–4237, 2007.

[50] C. D. Chin, V. Linder, and S. K. Sia. Lab-on-a-chip devices for global health: Past studies and future opportunities. *Lab on a Chip*, 7:41–57, 2007.

[51] H. Bruus. *Theoretical Microfluidics*. Oxford University Press, Oxford, 2007.

[52] Crystal-Fibre A/S `http://www.crystal-fibre.com`.

[53] G. Taylor. Dispersion of soluble matter in solvent flowing slowly through a tube. *Proc. of the Royal Soc. of London. Series A, Math. Phys. Sci.*, 219:186–203, 1953.

[54] D. Snakenborg, H. Klank, and J. P. Kutter. Microstructure fabrication with a co2 laser system. *J. Micromech. & Microeng.*, 14:182–189, 2004.

[55] J. C. Knight, J. Broeng, T. A. Birks, and P. St. J. Russell. Photonic band gap guidance in optical fibers. *Science*, 282:1476–1478, 1998.

[56] P. Yeh, A. Yariv, and E. Marom. Theory of bragg fiber. *J. Opt. Soc. Am.*, 68:1196–1201, 1978.

[57] M. A. van Eijkelenborg, M. C. J. Large, A. Argyros, J. Zagari, S. Manos, N. A. Issa, I. Bassett, S. Fleming, R. C. McPhedran, C. M. de Sterke, and N. A. P. Nicorovici. Microstructured polymer optical fibre. *Opt. Express*, 9:319–327, 2001.

[58] N. A. Mortensen. Semianalytical approach to short-wavelength dispersion and modal properties of photonic crystal fibers. *Opt. Lett.*, 30:1455–1457, 2006.

[59] N. A. Mortensen, J. R. Folkenberg, M. D. Nielsen, and K. P. Hansen. Modal cutoff and the v parameter in photonic crystal fibers. *Opt. Lett.*, 28:1879–1881, 2003.

[60] B. T. Kuhlmey, R. C. McPhedran, and C. M. de Sterke. Modal cutoff in microstructured optical fibers. *Opt. Lett.*, 27:1684–1686, 2002.

[61] G. Renversez, F. Bordas, and B. T. Kuhlmey. Second mode transition in microstructured optical fibers: determination of the critical geometrical parameter and study of the matrix refractive index and effects of cladding size. *Opt. Lett.*, 30(11):1264–1266, 2005.

[62] T. P. White, B. T. Kuhlmey, R. C. McPhedran, D. Maystre, G. Renversez, C. M. de Sterke, and L. C. Botton. Multipole method for microstructured optical fibers. i. formulation. *J. Opt. Soc. Am. B*, 19:2322–2330, 2002.

[63] B. T. Kuhlmey, T. P. White, G. Renversez, D. Maynstre, L. C. Botton, C. M. de Sterke, and R. C. McPhedran. Multipole method for microstructured optical fibers. ii. implementation and results. *J. Opt. Soc. Am. B*, 19:2331–2340, 2002.

[64] M. D. Nielsen, N. A. Mortensen, M. Albertsen, J. R. Folkenberg, A. Bjarklev, and D. Bonacinni. Predicting macrobending loss for large-mode area photonic crystal fibers. *Opt. Express*, 12(8):1775, 2004.

[65] M. D. Nielsen, G. Vienne, J. R. Folkenberg, and A. Bjarklev. Investigation of micro deformation induced attenuation spectra in a photonic crystal fiber. *Opt. Lett.*, 28:236–238, 2003.

[66] P. R. Isaac. Symmetry-induced modal characteristics of uniform waveguides .1. summary of results. *IEEE Transactions on microwave theory and techniques*, 5:421–429, 1975.

[67] P. R. Isaac. Symmetry-induced modal characteristics of uniform waveguides .2. theory. *IEEE Transactions on microwave theory and techniques*, 5:429–433, 1975.

[68] M. J. Steel, T. P. White, C. M. de Sterke, R. C. McPhedran, and L. C. Botton. Symmetry and degeneracy in microstructured optical fibers. *Opt. Lett.*, 26:488–490, 2001.

[69] N. A. Mortensen, M. D. Nielsen, J. R. Folkenberg, K. P. Hansen, and J. Lægsgaard. Small-core photonic crystal fibers with weakly disordered air-hole claddings. *J. Opt. A: Pure Appl. Opt.*, 6:221–223, 2004.

[70] MIT Photonic Bands, `http://ab-initio.mit.edu/mpb`.

[71] Comsol Multiphysics, `http://www.comsol.com`.

[72] M. Pedersen. *Functional Analysis in Applied Mathematics and Engineering*, volume 31 of *Studies in Advanced Mathematics*. CRC Press, London, 1999.

[73] S. C. Brenner and L. Ridgway Scott. *The Mathematical Theory of Finite Element Methods*. Springer-Verlag New York Inc., 2000.

[74] J. Jin. *The Finite Element Method in Electromagnetics*. Springer-Verlag New York Inc., 2002.

[75] S. Ahmed. Finite-element method for waveguide problems. *Electron. Lett.*, 4:387–389, 1968.

[76] M. Koshiba, K. HAYATA, and M .SUZUKI. Vectorial finite-element method without spurious solutions for dielectric waveguide problems. *Electron. Lett.*, 20:409–410, 1984.

[77] B. M. A. Rahman and J. B. Davies. Finite-element analysis of optical and microwave waveguide problems. *IEEE Transactions on Microwave Theory and Techniques*, 32:20–28, 1984.

[78] S. Selleri and M. Zoboli. Performance comparison of finite-element approaches for electromagnetic waveguides. *J. Opt. Soc. Am. A*, 14:1460–1466, 1997.

[79] C. Geuzaine, B. Meys, F. Henrotte, P. Dular, and W. Legros. A galerkin projection method for mixed finite elements. *IEEE Transactions on Magnetics*, 35:1438–1441, 1999.

[80] C. Geuzaine, B. Meys, P. Dular, and W. Legros. Convergence of high order curl-conforming finite elements. *IEEE Transactions on Magnetics*, 35:1442–1445, 1999.

[81] Kane Yee. Numerical solution of initial boundary value problems involving maxwell's equations in isotropic media. *Antennas and Propagation, IEEE Transactions on*, 14:302307, 1966.

[82] K. M. Ho, C. T. Chan, and C. M. Soukoulis. Existence of a photonic gap in periodic dielectric structures. *Phys. Rev. Lett.*, 65:3152–3155, 1990.

[83] S. G. Johnson and J. D. Joannopoulos. Block-iterative frequency-domain methods for Maxwell's equations in a planewave basis. *Opt. Express*, 8:173–190, 2001.

[84] H. S. Sözüer, J. W. Haus, and R. Inguva. Photonic bands: Convergence problems with the plane-wave method. *Phys. Rev. B*, 45:13962–13972, June 1992.

[85] CudosMof http://www.physics.usyd.edu.au/cudos/mofsoftware.

[86] M. Szpulak, W. Urbanczyk, E. Serebryannikov, A. Zheltikov, A. Hochman, Y. Leviatan, R. Kotynski, and K. Panajotov. Comparison of different methods for rigorous modeling of photonic crystal fibers. *Opt. Express*, 14:5699–5714, 2006.

[87] A. Yariv. Coupled-mode theory for guided-wave optics. *IEEE J. Quant. Electron.*, QE-9:919 – 933, 1973.

[88] A. Yariv and P. Yeh. *Photonics*. Oxford University Press, Oxford, 2007.

[89] K. E. Carroll, C. Zhang, D. J. Webb, K. Kalli, A. Argyros, and M. C. J. Large. Thermal response of bragg gratings in pmma microstructured optical fibers. *Opt. Express*, 15:8844–8850, 2007.

[90] A. W. Snyder and J. D. Love. *Optical Waveguide Theory*. Chapman & Hall, New York, 1983.

[91] A. M. Vengsarkar, P. J. Lemaire, J. B. Judkins, V. Bhatia, T. Erdogan, and J. E. Sipe. Long-period fiber gratings as band-rejection filters. *J. Lightwave Technol.*, 14:58–65, 1996.

[92] X. W. Shu, L. Zhang, and I. Bennion. Sensitivity characteristics of long-period fiber gratings. *J. Lightwave Technol.*, 20:255–266, 2002.

[93] X. Daxhelet and M. Kulishov. Theory and practice of long-period gratings: when a loss becomes a gain. *Opt. Lett.*, 28:686–689, 2003.

[94] D. Segelstein, "The Complex Refractive Index of Water", M.S.Thesis, University of Missouri–Kansas City, 1981.

[95] The International Association for the Properties of Water and Steam, IAPWS 5C, 1997, `http://www.iapws.org/relguide/rindex.pdf`.

[96] B. J. Eggleton, P. S. Westbrook, R. S. Windeler, S. Spälter, and T. A. Strasser. Grating resonances in air-silica microstructured optical fibers. *Opt. Lett.*, 24(21):1460 – 1462, 1999.

[97] H. R. Sorensen, J. Canning, J. Laegsgaard, K. Hansen, and P. Varming. Liquid filling of photonic crystal fibres for grating writing. 270 (2):207–210, 2007.

[98] M. Albertsen, J. Lægsgaard, S.E. Barkou Libori, K. Hougaard, J. Riishede, and A. Bjarklev. Coupling-reducing k-points for photonic crystal fibre calculations. *Photonics and Nanostructures*, 1:43–53, 2003.

[99] G. Humbert, A. Malki, S. Fevrier, P. Roy, and D. Pagnoux. Electric arc-induced long-period gratings in ge-free air-silica microstructure fibres. *Electron. Lett.*, 4:349–350, 2003.

[100] H. Dobb, K. Kalli, and D.J. Webb. Temperature-insensitive long period grating sensors in photonic crystal fibre. *Electron. Lett.*, 11:657–658, 2004.

[101] G. Kakarantzas, T. A. Birks, and P. St. J. Russell. Strucural long-period gratings in photonic crystal fibers. *Opt. Lett.*, 27:1013–1015, 2002.

[102] Y. Zhu, P. Shum, J.-H. Chong, M. K. Rao, and C. Lu. Deep-notch, ultracompact long-period grating in a large-mode-area photonic crystal fiber. *Opt. Lett.*, 28:2467–2469, 2003.

[103] Y. Zhu, P. Shum, H.-W. Bay, X. Chen, C.-H. Tan, and C. Lu. Wide-passband, temperature-insensitive, and compact pi-phase-shifted long-period gratings in endlessly single-mode photonic crystal fiber. *Opt. Lett.*, 29:2608–2610, 2004.

[104] Y. Zhu, P. Shum, H.-W. Bay, M. Yan, X. Yu, J. Hu, J. Hao, and C. Lu. Strain-insensitive and high-temperature long-period gratings inscribed in photonic crystal fiber. *Opt. Lett.*, 30:367–369, 2005.

[105] K. Morishita and Y. Miyake. Fabrication and resonance wavelengths of long-period gratings written in a pure-silica photonic crystal fiber by the glass structure change. *J. Lightwave Technol.*, 22:625–630, 2004.

[106] "Fiber-optic sensors", Student project by Rune Thode Nielsen and Christian Iversen Vorm. In Danish.

[107] Z. Y. Wang and S. Ramachandran. Ultrasensitive long-period fiber gratings for broadband modulators and sensors. *Opt. Lett.*, 28:2458–2460, 2003.

[108] W. Liang, Y. Y. Huang, Y. Xu, R. K. Lee, and A. Yariv. Highly sensitive fiber bragg grating refractive index sensors. *App. Phys. Lett.*, 86:151122, 2005.

[109] K. Zhou, X. Chen, L. Zhang, and I. Bennion. High-sensitivity optical chemsensor based on etched d-fibre. *Electron. Lett.*, 40:232–234, 2004.

[110] A. Cusano, A. Iadicicco, P. Pilla, L. Contessa, S. Campopiano, A. Cutolo, M. Giordano, and G. Guerra. Coated long-period fiber gratings as high-sensitivity optochemical sensors. *J. Lightwave Technol.*, 24:1776–1786, 2006.

[111] H. Dobb, K. Kalli, and D.J. Webb. Measured sensitivity of arc-induced long-period grating sensors in photonic crystal fibre. *Opt. Com.*, 260:184–191, 2006.

[112] P. Steinvurzel, E. D. Moore, E. C. Magi, and B. J. Eggleton. Tuning properties of long period gratings in photonic bandgap fibers. *Opt. Lett.*, 31:2103–2105, 2006.

[113] H. El-Kashef. The necessary requirements imposed on polar dielectric laser dye solvents. *Physica B*, 279:295–301, 2000.

[114] Z. Y. Wang, J. R. Heflin, R. H. Stolen, and S. Ramachandran. Analysis of optical response of long period fiber gratings to nm-thick thin-film coatings. *Opt. Express*, 13:2808–2813, 2005.

[115] S. G. Johnson, M. Ibanescu, M. A. Skorobogatiy, O. Weisberg, J. D. Joannopoulos, and Y. Fink. Perturbation theory for maxwell's equations with shifting material boundaries. *Phys. Rev. E*, 65:066611, 2002.

[116] J. S. Petrovic, H. Dobb, V. K. Mezentsev, K. Kalli, D. J. Webb, and I. Bennion. Sensitivity of lpgs in pcfs fabricated by an electric arc to temperature, strain, and external refractive index. *J. Lightwave Technol.*, 25(5):1306, 2007.

[117] `http://www.fuji-keizai.com`.

[118] Værdiansættelsesrapport - Handelsbanken.

[119] `http://www.thebiotechclub.org/industry/investment/biacore.php`.

Appendix A

Business plan

This is a tentative business plan made for a Venture Cup competition in Feb. 2006. It is not, and has not since then, been the author's intention to start a company for the reasons stated in Sec. 6.1. The reasons are technical in nature.

Executive summary

- **Type of business**
  Photoniq is a producer of high-end laboratory equipment for the biotechnology and pharmaceutical companies.

- **Company summary**
  Photoniq will produce state-of-the-art label-free biosensors which uses technology that originates in the optical communication technology. The product consists of a bioanalyzer and a biochip for analysis of biomolecule interactions.
  The performance of the biosensor exceeds any currently available product on the market. The biosensor is very suitable for mass production and the production costs are far lower than, not only any product currently on the market, but also to any product that may be conceived within decades. The production cost of a bioanalyzer is around 5.000 Euro and the production cost of a biochip is around 1 Euro.

- **Added values**
  The possibilities offered by this new product may increase the cost-effectiveness of the research & development (R&D)

of the pharmaceutical and biotechnological companies due to reduced investments in laboratory equipment and more advanced biomolecular analyses.

- **The market**
  The total biochip market size in 2004 was about 2.0 billion Euro and is projected to grow to about 5.1 billion Euro in 2009 [117]. The target market segments of drug discovery, life sciences and food analysis are estimated to 100m Euro [118].
  The market is currently dominated by a single competitor, which has an estimated market share of 85-90% [118]. Photoniq may challenge this monopoly.

- **Business system**
  Market entry is planned to be medio 2007 and is world-wide.

- **IPR**
  Intellectual property rights are a fundamental condition for a successful start-up of the company.

A.1   Business idea

In the last decade major pharmaceutical and biotechnology companies have seen their R&D costs explode as their actual productivity has declined. The companies are seeking to increase the cost-effectiveness of their laboratories through new and improved techniques and equipment. Biochip products are making their way into the business as a substitute for older, less cost-efficient systems.

In the high-end market the researchers use high-technology equipment to obtain valuable information about protein functionality and disease mechanisms. Today several products offer analysis of biomolecule interactions by attaching a label to one of the biomolecule reagents. This label slightly modifies the chemical properties of the reagent and the technique is less attractive to the researcher than label-free analysis. Products that allow the analysis of biomolecule interactions label-free, non-invasively and real-time are generally referred to as label-free biosensors.

Label-free biosensors are available today on-the-shelf with a technology known as surface plasmon resonance (SPR). SPR prod-

ucts have been commercially available on the market for 15 years and is today an integral part in high-end pharma/biotech R&D. The SPR market is dominated by a single corporation. Its systems are reliable, but are generally too expensive to purchase and operate, and does not have sufficient accuracy for many problems of interest for the researches [12].

Recently, there has been growing interest in developing cost-effective substitute or complementary products to SPR. Although several new technologies have been proposed in the scientific communities, no technology has yet prevailed, and it is still too early to point out a potential winner.

What's new in Photoniq's products?

- Revolutionary generation skipping label-free biosensor.
- Offer new possibilities with label-free biosensors.
- Low cost of production.
- Highly scalable production.

Photoniq plans to produce an analysis station, referred to as the bioanalyzer, and a disposable single-use biochip. The biochip holds a miniaturized laboratory with a state-of-the-art optical fibre sensor element. The reagents are injected into the biochip, which is then inserted in the bioanalyzer. The bioanalyzer is connected to a standard personal computer that records the data of the analysis. The biochip is discarded after use to avoid cross contamination of subsequent analyses.

The fibre sensor element is based on next generation optical fibres, the so-called PCFs, produced by a Danish spin-off company, Crystal-Fibre [52]. The optical fibres may be produced by kilometres, and only about 20 mm of fibre is needed for a single sensor, making the technology very scalable in production. The fibre sensor has the additional advantages of small sample volume, reducing costs by reducing the amount of costly biomolecules consumed in the analysis. Furthermore, the optical detection system in the bioanalyzer is relatively cheap.

The proposed technology is fifty times more accurate than SPR, opening up for analysis of interactions of biomolecules previously

beyond the accuracy of label-free biosensors. The technology is not only more accurate, but also vastly cheaper in production, thus the proposed system skips a generation of technology, being both cheaper and better than current technologies.

> "I would like to have this product right away - I have a thousand applications for it!"
> Research Associate Professor Martin Dufva, project leader in Micro Array Technology, Department of Micro- and Nanotechnology. Technical University of Denmark.

State of technology

The proof-of-principle of the technology has been obtained in autumn 2005. The technology know-how of Photoniq will be essential when constructing a successful commercial biosensor.

At the moment patenting the biochip is in process at the Technical University of Denmark. Some development work has yet to be done before a functioning prototype can be presented. Such work is already initiated.

A.2   Marketing

Photoniq's market is characterized as business-to-business (BTB) and the costumer segment targeted is the laboratories in pharmaceutical and biotech companies. This segment is more attractive than the business-to-consumer market in for example point-of-care testing (POCT) applications. The high accuracy and ease of use is ideal for research and will give the companies great value. In contrast, the system offered by Photoniq is relatively complicated compared with the often brutally simple POCT in use today. Furthermore, POCT systems such as recently introduced by the Danish company Chempaq have yet to prove their sales. In any instances, the POCT market has proven to be much harder to enter and expand much slower than the explosive growth anticipated in the late '90's.

Market size and current competitors

The total biochip market size in 2004 was about 2.0 billion Euro and is projected to grow to about 5.1 billion Euro in 2009 [117]. Though this market covers many different areas, the SPR technology is primarily used in the drug discovery, life sciences and food analysis segments. The size of these three segments is estimated to 100m Euro

"Our success is based on the ability of our SPR biosensor technology to provide high-quality, real-time data of biomolecular interactions"

- Ulf Jönsson, former CEO of Biacore, market leader.

At the present, the field of labelfree biosensors is dominated by a few, large players:

1. Biacore AB - Several SPR systems available.
2. Applied Biosystems - A single system SPR available.
3. Thermo Electron - A single system SPR available
4. Evotec - Ion-beam technology

All current corporations except Evotec use the same technology, namely the SPR technique. Biacore, a Swedish company which entered the market in 1990, is the current market leader dominating with a monopoly like status. Biacore's exact market share is unknown, but based on the number of academic reviews and publications using Biacore products their market share can be estimated to 85-90 % . Biacore's success is build on being the first on the market to provide label-free biosensor and now holds a large patent portfolio.

The other competitors are large biotech instrument producing companies with a wide array of other products, but are minor players on the SPR system market. Applied Biosystems introduced their own SPR analyzer in September 2003 with some success. Thermo Electron introduced their system in July 2005 and has yet to prove their sales on the market. Evotec is the only real competitor to Biacore, but is not considered as a real threat to Biacore's dominating position on the market. Under the current circumstances Biacore has advantages in performance, technology and market share. Each competitor's technologies have

different qualities, but none provide the same sensitivity, repro-
ducibility, and simultaneous set of interaction data as Biacore.

Furthermore, Biacore has the advantage of already being estab-
lished on the market. This means that the customers are used
to them as collaborator. Biacore are strong in customer relation
management. As a Biacore customer, you can expect being able
to benefit by the large network in science areas with relevance to
your own research. Customers are provided with knowledge and
information on the product specifications and applications. In
other words, you become a member of the Biacore family. This
high grade of customer loyalty can be seen as an entry barrier
for market enterers such as Photoniq. Photoniq must overcome
this barrier by reaching relevant people such as scientists and
other key decision makers. This will be further elaborated in the
market approach paragraph.

Customer behavior

The consumer behavior and decision making in the BTB-market
is generally characterized by being focused on the relation be-
tween price and quality, service, information, consultancy and
reliability. Purchasing expensive research equipment is a strate-
gic decision, and the customers expect to benefit from the equip-
ment over a longer period of time. As a consequence these deci-
sions are often taken at highest levels in the customer companies.
Additionally, the decision process is often in several phases and
usually includes a number of decision makers.

In most large companies the scientists' authority is limited and
purchase decisions have to be approved at a higher level. Most
scientists are able to purchase science equipment without ap-
proval to a price within 20.000 Euro. The product of Photoniq
can be produced with substantially lower production costs than
the current competitors' products. Photoniq will be able to sell
their product at lower prices than our competitors and thereby
sell directly to the end user.

Market entry barriers

When entering the market Photoniq must take the following entry barriers into account:

Current competitors

As earlier mentioned, Biacore has build up solid customer relations. This is a potential entry barrier for Photoniq. When communicating with potential customers it is essential that Photoniq is able to demonstrate the advantages of the product compared to what is presently available on the market.

Costs of technology transition

The relatively high costs in connection with changing technology must be financially justified before a transition to new technology will be considered. Companies already having acquired SPR systems will be reluctant to spend large investments in new equipment while sustaining the loss of selling relative new, and well functioning SPR systems. Again it is essential to inform potential customers of the advantages of the Photoniq products compared to their current systems. Photoniq must communicate its advantages of being cheaper than the competitors and at the same time having a superior product.

Certificates and approvals

In some of the relevant industries in the market specific approvals and certificates are required in order to be able to use the system of Photoniq in scientific research. Photoniq is aware of the importance of fulfilling the specific requirements for the necessary certifications and approvals at an early stage of the company develop.

Need for capital

A considerable amount of capital is needed in order to be able to enter the market and compete equally with the financially strong

competitors. There are high costs associated with developing the production facilities for the biochip and bioanalyzer.

Market approach - Communication and product

In science new products, however promising, are seldom accepted overnight. Laboratories are generally conservative in regards to purchasing equipment. Poorly performing or error prone equipment may be fatal to a laboratory or a research project. Furthermore laboratory equipment may pose heavy financial investments in both acquirement and training of personnel. As mentioned, our strategy will be seeking to influence the leading scientists. High profile scientific publications with leading researchers will clearly show the superior performance of the Photoniq systems. The new opportunities that the systems offer the customers, will give them a new edge over their competitors. The scientific publications should appear some time in advance of market entry to gain general acceptance; but not too soon for Photoniq's competitors to copy the technology. Laboratory managers depend on the board of directors for funding new equipment. The advantages of the system should be so obvious that an investment application from the laboratory managers should be difficult to refuse for the board of directors.

Photoniq's system should in any case be easy to operate for the laboratory technicians. This will be done by having the user functions similar to the equipment in use today, and in part by being automated.

Market approach - Price strategy

Competitors to Photoniq may emerge in time with new technology. Although different label-free biosensors have been demonstrated, none are commercially available to the market. There are several reasons for this, for example difficulty of use, difficulty of manufacture, unreliability, being ill suited for mass production or requiring extensive investments in high-tech production facilities.

The market for our product was 100m Euro in 2004. The increasing demand for pharmaceutical products along with the increas-

ing health care cost will press costs on pharmaceutical products. Since R&D constitutes the far largest part of the companies' expenses, a way of making it more cost-effective must be carried out. A successful market introduction and consolidation will see the complete substitution of current technologies in the long run.

The retail price of a Biacore instrument starts at 135.000 Euro and the biochips range from 75-300 Euro. The production cost of Photoniq's bioanalyzer is expected to be around 5.000 Euro and a single biochip will be around 1 Euro. This means that we will be able to set the price lower than Photoniq's competitors and still gain a considerable variable profit.

To avoid the aggressive reactions from the competitors to a market entry, the equipment should be marketed as complementing rather than replacing the competitor's equipment. In time, when Photoniq's system is established on the market, the strategy will change and the system will be sold as replacement equipment.

Market approach - Distribution

When entering the market Photoniq will distribute its products from a base in Denmark and later expand with sales divisions placed close to the customers on the international markets. The distribution should be done in collaboration with a larger company that already has an international sales force.

A.3 Business system and organization

Start-up team

The business idea is being developed by a team of one student from the Technical University of Denmark and two students from Copenhagen Business School (CBS) of Denmark.

The students are the following:

- Lars Rindorf (LHR) - founder, chief scientist, intellectual property rights - M.Sc. in applied physics from the Technical University of Denmark in 2003 - Currently studying

for the Ph.D. degree on the subject of fiber optic biosensors (biophotonics) at the Department for Communication, Optics and Materials, COM, at the Technical University of Denmark.

- Teis Vester (TV) - co-founder, business developer - Bachelor student in the third year at Copenhagen Business School. - Part time working in the accounting trade

- Benjamin Eriksson (BE) - co-founder, business developer - Bachelor student in the third year at Copenhagen Business School. - Part time working in the logistics trade

Required competencies within the company

The biotechnological sector contain a lot of technical specific knowledge and the sector also demands great knowledge in the research areas. This will be one of the greatest obstacles in the start of Photoniq and therefore we have decided to split the required competencies in two; the technical area and the non-technical area.

In the technical area following competencies will be required in the company

- Fiber optics. Theory and experiments.
- Plastic injection moulding
- Production processes
- Electronics
- Biochemistry

In the non-technical area following competencies are required:

- Intellectual property rights (IPR).
- Finance.
- Logistics
- Law.
- Management.
- Experienced CEO

In the Technical area the fiber optics are covered within LHR experience and knowledge, while the other parts will be outsourced (see Schedule). Still, the whole area will be supervised by LHR.

In the non-technical area the property rights, finance, logistics, and management are covered by the three founders while the experienced CEO must be found within the biotechnological sector and law must be added from an attorney.

Business development

The study phase

The Study phase started in the middle of 2004, with the Ph.D project of LHR at the Technical University of Denmark. The studies led to the discovery of a promising technology and in the middle of 2005 the proof-of-principle was obtained.

The prototype phase

This is the current phase of the company. During the phase a functioning bioanalyzer and biochip will be developed.

The developing phase

In the developing phase the prototype should be used to prepare the final production line. The specifications of the electronics in the bioanalyzer will be written and the development will be done with an external contractor. The same approach will be done with the machine for the injection moulding of the biochips. The marketing phase is being prepared.

The market entry phase

Marketing activities will be further speed up. In this phase the production line will be fully operational, and Photoniq will introduce its products on a full scale. The introduction will be initiated at the key markets (US, Japan, and Europe) and representative offices will be opened in these markets. The phase will

start in the middle 2007 and last until the middle 2008. Thus
the phase duration is a year, which will give Photoniq the time
to capture markets shares and build a customer network.

The consolidating/expansion phase

Photoniq will at this point be able to expand to other market
and continuously capture markets shares. The products will be
in greater demand and protected by the patents which were ob-
tained throughout the preceding phases. The other important
subject of this phase will be the consolidation of the current
market share. This will be done by customer relation and man-
agement.

A.3.1   IPR strategies

Current market players concentrated considerable effort in IPR.
Biacore AB has been dominating the market due to its favorable
patent portfolio of 24 patents [119]. Photoniq must also pro-
tect its market position by patenting or face competition from
companies copying the technology.

The patenting should be aimed at three areas: I. Functional
patenting of Biochip II. Production patenting of the Biochip and
Bioanalyzer III. Patenting of the biochemistry in optical fibers

Although the principle of fiber optic sensor itself can not be
patented, practical use of the invention is impossible unless a
feasible incorporation can be carried out. This may be divided
into two sub areas: optical readout and incorporation of the
sensor element in a microfluidic system (a biochip).

There are no Biochips with integrated optical fibers commercially
available to the market today. A patent protecting an efficient
integration of the optical fiber in the Biochip will thus give Pho-
toniq a favorable position over would-be copying competitors.

The most effective patent, however, might be on the biomolecular
functionalization of the fiber optic sensor. 'Functionalization' is
the technique in which a surface is prepared with biomolecules
in order to carry out an experiment. Such patents are common
within SPR.

Patenting expenses

Obtaining a patent is expensive. After the original patent is obtained, patents must be translated and applied for in the countries of the interesting markets. A patent cost about 10,000 Euro to obtain in each country, followed by the same amount over a fifteen year period. However, in markets where there are only a few dominating international producers, the patenting may be limited to the large key markets, where the residual market is too small to sustain a high-tech company with large development costs. The IPR strategy of Photoniq may fit such a strategy well. Key countries for Photoniq will be large European nations in the EU, the United States, Japan and the emerging markets in China and India.

Appendix B

Sellmeier expressions

B.1   Silica glass (SiO$_2$)

The refractive index of pure silica glass can be calculated with the Sellmeier expression

$$
n_{\mathrm{SiO_2}}(\lambda) = \sqrt{1 + B_1 \frac{\lambda^2}{\lambda^2 - \lambda_1^2} + B_2 \frac{\lambda^2}{\lambda^2 - \lambda_2^2} + B_3 \frac{\lambda^2}{\lambda^2 - \lambda_3^2}}, \quad \text{(B.1)}
$$

using the constants
$B_1 = 0.696\ 532\ 5$, $\lambda_1 = 4.36\ 830\ 9 \times 10^{-2}$ μm,
$B_2 = 0.408\ 309\ 9$, $\lambda_2 = 0.139\ 499\ 9$ μm,
$B_3 = 0.896\ 876\ 6$, $\lambda_3 = 9.79\ 339\ 9$ μm.

B.2   Water (H$_2$O)

Nomenclature

The data comes from Ref. [95]
n refractive index with respect to vacuum
T absolute temperature
λ wavelength of light
ρ mass density
Reference Constants: temperature $\mathrm{T}^* = 273.15$ K, density $\rho^* = 1000$ kg$\times$m^{-3}, wavelength $\lambda^* = 0.589$ μm
Dimensionless variables: temperature, $\bar{T} = T/\mathrm{T}^*$, density $\bar{\rho} = \rho/\rho^*$,

$a_0 = 0.244\ 257\ 733$	$a_4 = 1.589\ 205\ 70 \times 10^{-3}$
$a_1 = 9.746\ 344\ 76 \times 10^{-3}$	$a_5 = 2.459\ 342\ 59 \times 10^{-3}$
$a_2 = -3.732\ 349\ 96 \times 10^{-3}$	$a_6 = 0.900\ 704\ 920$
$a_3 = 2.686\ 784\ 72 \times 10^{-4}$	$a_7 = -1.666\ 262\ 19 \times 10^{-2}$
$\lambda_{\text{UV}} = 0.229\ 202\ 0\ \mu\text{m}$	$\lambda_{\text{IR}} = 5.432\ 937\ \mu\text{m}$

wavelength $\lambda = \lambda/\lambda^*$.

The refractive index is represented by the following equation

$$\frac{n^2-1}{n^2+2}\frac{1}{\bar{\rho}} = a_0 + a_1\bar{\rho} + a_1\bar{T} + a_2\bar{\lambda}^2\bar{T} + a_4/\bar{\lambda}^4 + \frac{a_5}{\bar{\lambda}^2 - \bar{\lambda}_{\text{UV}}^2} + \frac{a_6}{\bar{\lambda}^2 - \bar{\lambda}_{\text{IR}}^2} + a_7\bar{\rho}^2$$
$$(\text{B.2})$$

The coefficients a_0 - a_7, and the constants λ_{UV}, λ_{IR} are given in the table.